2024

Turbulent Shockwave/Boundary-Layer Interactions Generated by Sharp Swept Fins

Dustin Levi Otten

Recommended Citation

Otten, Dustin Levi, "Turbulent Shockwave/Boundary-Layer Interactions Generated by Sharp Swept Fins" (2024). *Mechanical and Aerospace Engineering Dissertations*. 407.
https://mavmatrix.uta.edu/mechaerospace_dissertations/407

TURBULENT SHOCKWAVE/BOUNDARY-LAYER INTERACTIONS GENERATED BY SHARP SWEPT FINS

by

DUSTIN LEVI OTTEN

Presented to the Faculty of the Graduate School of
The University of Texas at Arlington in Partial Fulfillment
of the Requirements
for the Degree of

DOCTOR OF PHILOSOPHY

THE UNIVERSITY OF TEXAS AT ARLINGTON
December 2023

To my wife Nicci who had the hardest job of all...

ACKNOWLEDGEMENTS

I would like to thank my adviser Dr. Frank Lu for all of the patience, encouragement, and motivation. He was especially understanding of the school/work/family tight-rope act I had to perform during the six years of Ph.D. work. I could not have completed this with any other adviser. I wish to thank my academic advisors, Dr. Habib Ahmari, Dr. Luca Maddalena, Dr. Brian Dennis, and Dr. Liwei Zhang for their interest in my research and for taking time to serve in my dissertation committee.

I also thank Lockheed Martin for financial support for my doctoral studies. Several people at LMMFC were instrumental in my success. I would like to give specific thanks to Tim Assel, Mark Bergee, Chase Caruth, Jeff Metzgar, and Michael McWithey with Lockheed Martin for their support and encouragement.

Finally, thanks be to God for helping me through the Ph.D. I would like to thank my parents (David and Danele), mother-in-law (Nancy), siblings, aunts, uncles, and grandparents for their support and encouragement. I am also extremely grateful to my wife for her sacrifice, encouragement, and patience throughout my PhD studies. I love you Nicci! My children have been especially patient throughout this process, and we all look forward to its conclusion!

October 24, 2023

ABSTRACT

TURBULENT SHOCKWAVE/BOUNDARY-LAYER INTERACTIONS GENERATED BY SHARP SWEPT FINS

DUSTIN LEVI OTTEN, Ph.D.

The University of Texas at Arlington, 2023

Supervising Professor: Frank K. Lu

The shock/turbulent boundary layer interaction (STBLI) generated by a sharp fin with a 60 deg leading edge sweep mounted above a flat plate at Mach 2.5 was studied numerically. Incipient separation due to this highly swept fin was determined by varying the fin angle to the incoming freestream. The effect of a small fin/plate gap on STBLI incipient separation was established. Sweeping the fin increases the deflection required for incipient separation as the sweep reduces the interaction strength. A gap causes flow leakage under the fin, further reducing the interaction strength on the windward side. The incipient angle of attack is increased when the gap is large enough. In this study, all gaps investigated, produced incipient separation. For the leeward side of the fin, a vortex at the fin leading edge was generated due to the pressure difference across the fin leeward and windward sides. In the cases with gaps, an additional vortex is generated at the fin leading edge and a vortex at the plate surface is also produced. It was found that the effect of the gap is to change the location and shape of these additional vortices. The fin angle to the incoming freestream was varied for three different gap heights to determine the effect of gap height on fin normal force, root bending moment, and hinge moment. The influence of the fin/plate gap on fin loads was established. The effect of increasing the fin/plate gap is to decrease fin effectiveness. Additionally the effect of gap height on the STBLI upstream influence line, primary separation, and attachment angles was compared to empirical relations. For the gaps investigated, no change in the inviscid shock angle was observed and so no significant changes in the upstream influence line, primary separation, or attachment angles were observed. As for the leeside of the fin similarities between it and the leeside of a delta wing were investigated. Numerical results agree qualitatively with those obtained from delta wing experiments. In contrast to full delta wing results, mounting the fin to the plate noticeably altered the lambda shock shape, but the vortex core location was relatively unchanged. These differences were seen in both numerical and experimental results for a fin on a plate. The same sharp fin was deflected 12 deg and mounted above a body of revolution at Mach 2.5. The results were compared to the same fin mounted above a flat plate, and showed similar lines of upstream influence, primary separation, and inviscid shock angles. However, the body of revolution caused these lines to curve rather than maintain a constant slope in the farfield region. This is at odds with the quasiconical flow observed by the fin on the flat plate, but is consistent with results from other studies. The peak and plateau normalized surface pressures within the separation region were observed to be less on the surface of the cylinder compared to the surface on the flat plate. These features can be attributed to the transverse curvature of the body of revolution.

TABLE OF CONTENTS

Appendix

LIST OF ILLUSTRATIONS

LIST OF TABLES

Table Page

NOMENCLATURE

b	span
$CD_{k\omega}$	κ–ω cross diffusion
CFD	computational fluid dynamics
CFL	Courant–Friedrich–Lewis (CFL) condition
C_A	axial force coefficient
C_f	skin friction coefficient
C_{HM}	hinge moment coefficient
C_N	normal force coefficient
C_p	pressure coefficient
C_{RBM}	root bending moment coefficient
c	chord
c_p	specific heat at constant pressure
c_v	specific heat at constant volume
d	diameter, distance to nearest wall
E	total energy
$\mathbf{F}$	Navier–Stokes inviscid flux vector
F	κ–ω blending function
FDM	finite difference method
FIT	free interaction theory
FVM	finite volume method
f	$g/(g+b)$, gap factor
$\mathbf{G}$	Navier–Stokes viscous flux vector

g	gap height
H	total enthalpy
HM	hinge moment
h	height
k	turbulence kinetic energy
k	thermal conductivity
k_0	thermal conductivity at reference temperature
LE	leading edge
l	length
M	Mach number
M_n	$M_\infty \sin\beta_0$, Mach number normal to inviscid shock trace on the flat plate
MRC	moment reference center
NF	normal force
P	pressure
P_k	turbulence production
P_{plat}	plateau pressure
Pr	Prandtl number
$\mathbf{Q}$	Navier–Stokes dependent variable vector
q	velocity component perpendicular to separation line, heat transfer/flux
R	(re)attachment point
RANS	Reynolds averaged Navier–Stokes
RBM	root bending moment
Re	Reynolds number
Re_θ	Reynolds number based on momentum thickness
R_c	radius of vortex core

Re_u	unit Reynolds number
r	radius
r	recovery factor
S	separation point
S_{ij}	mean strain
SBLI	shock wave/boundary layer interaction
SST	shear stress transport
STBLI	shock wave/turbulent boundary layer interaction
S_μ	Sutherland's viscosity constant
S_k	Sutherland's thermal conductivity constant
T	temperature
T_0	reference temperature
TKE	turbulent kinetic energy
TVD	total variation diminishing
t	time
U	velocity
(u, v, w)	velocity in Cartesian coordinate system
u^+	velocity in wall coordinates
UIL	upstream influence line
VCO	virtual conical origin
w	width
(x, y, z)	Cartesian coordinate system
x_f	x-location of fin leading-edge
y^+	yu_τ/ν wall coordinates
α	angle made between fin surface and the incoming freestream flow, angle-of-attack

α_N	angle of attack relative to fin/wing leading edge
β	angle between surface-flow features with incoming freestream flow
β_0	inviscid shock angle at the flat plate
β_U	upstream influence angle
β_S	separation angle
δ_{ij}	delta function
$\Delta\beta_0$	$(\beta_0 - \mu_\infty)$, reduced shock angle
$\Delta\beta_U$	$(\beta_U - \mu_\infty)$, reduced upstream influence angle
Δy_1	distance to first centroid away from wall
δ	boundary layer thickness, fin deflection angle
ϵ	rate of change of turbulence kinetic energy
Γ	circulation
γ	c_p/c_v, ratio of specific heats
η_k	Kolmogorov length scale
θ	wedge angle
θ_s	shock angle
$\theta_{1/2}$	fin leading-edge half angle
κ	von Kármán constant
Λ	leading-edge sweep angle
μ	dynamic viscosity
μ_∞	$\sin^{-1}(1/M_\infty)$, Mach angle of incoming freestream
μ_0	viscosity at reference temperature
μ_t	turbulent viscosity
ν	μ/ρ, kinematic viscosity
ν_t	eddy viscosity

ξ	p_2/p_1, pressure ratio across the inviscid shock trace on the flat surface
Π	wake parameter
ρ	density
τ	shear stress, strain
τ_t	turbulence timescale
Φ	dilation
$\bar{\chi}$	viscous interaction similarity parameter
Ω	angular velocity
ω	turbulent specific dissipation rate
ω_x	streamwise vorticity

Subscripts

BL	boundary layer
e	boundary layer edge
i	incipient
n	normal to the inviscid shock trace on the interaction surface
p	plateau
$plat$	plateau
s	shock
w	wall
∞	incoming freestream conditions

CHAPTER 1

INTRODUCTION

1.1 Shock Wave/Boundary Layer Interaction (SBLI)

Shock wave/turbulent boundary layer interactions (STBLI) are an unavoidable phenomenon in high-speed flows. High-speed missiles and aircraft encounter STBLI at many locations on the vehicle airframe. Examples where STBLI occur on a flight vehicle are shown in Fig. 1.1. Any junction between the body and control surfaces, wings, engine intakes, or other protuberances introduce SBLIs which are likely turbulent and must be analyzed for detrimental impacts. These detrimental impacts include a loss of aerodynamic performance, enhanced localized heating and unsteadiness, all of which are greatly exacerbated when the boundary layer separates [1].

Building block geometries are used for fundamental STBLI studies. As shown in Fig. 1.2, the six different fundamental geometries which produce swept shock waves are: a) sharp unswept fins; b) sharp swept fins; c) semicones; d) swept compression ramps; e) blunt fins; and f) double sharp fins. Each of these fundamental geometries isolate primary geometric drivers behind the observed STBLI on the flight vehicle. Taking a swept or unswept fin as an example, it can either represent a control surface, engine inlet, or other protuberance as shown in Fig. 1.1. Such building blocks capture the features of SBLI without complications of actual flight configurations and are essential for fundamental studies.

For missile stability and control, the junction between a fin control surface and an axisymmetric body is of particular interest. Interactions in this region can cause high surface heating rates and impact the effectiveness of the control surface. Missiles

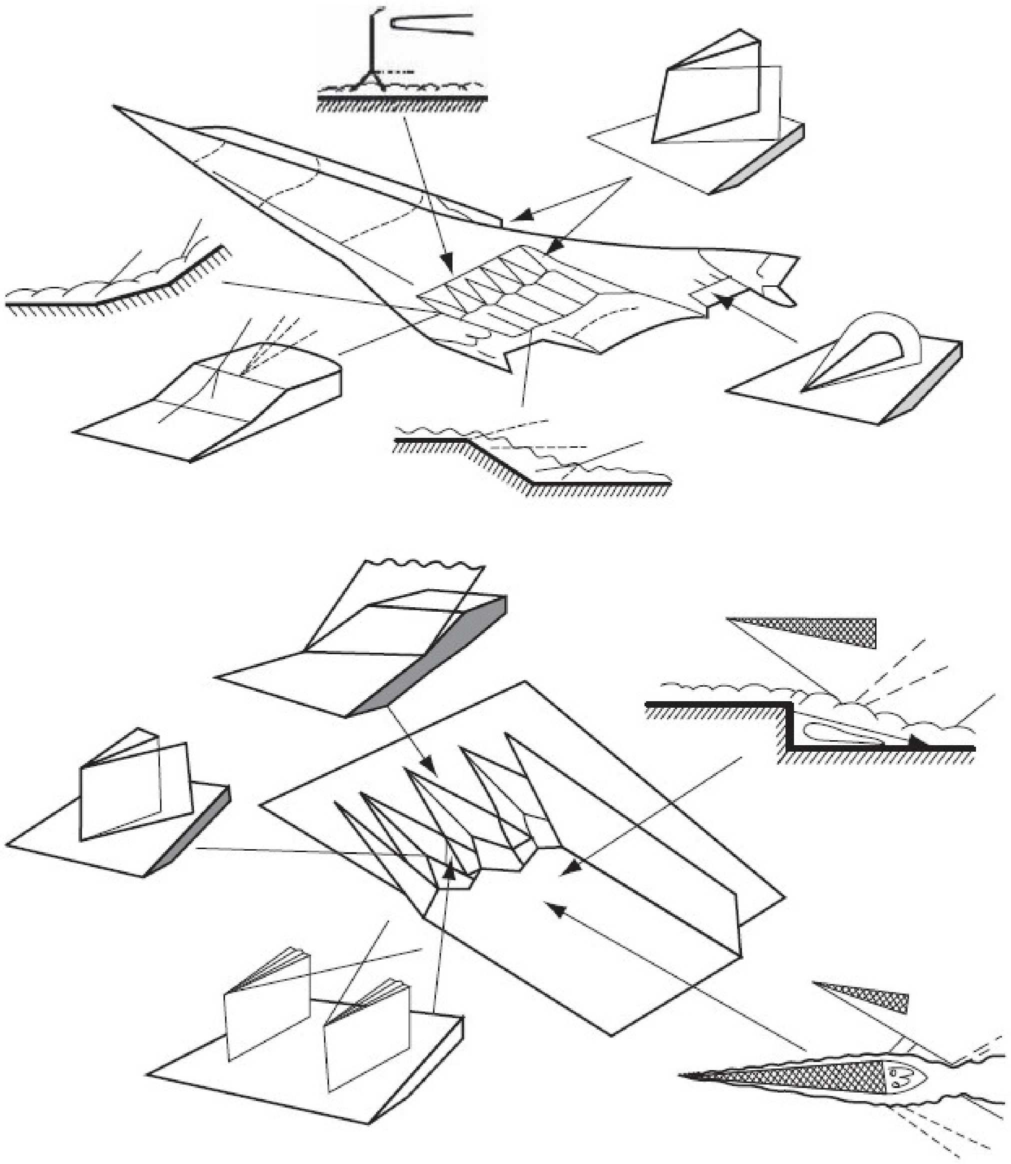

Figure 1.1: Examples of STBLI on an high-speed vehicle airframe [2]

are generally cylindrical but, in practice, flat plate results for SBLI and boundary layers are applied, and assumed to be adequate for engineering applications. There are occasions where a cylindrical surface is implemented to further investigate the phenomenon. Thus, by comparing SBLI results from flat plate studies to results obtained with a fin on a cylindrical body these assumptions can be tested.

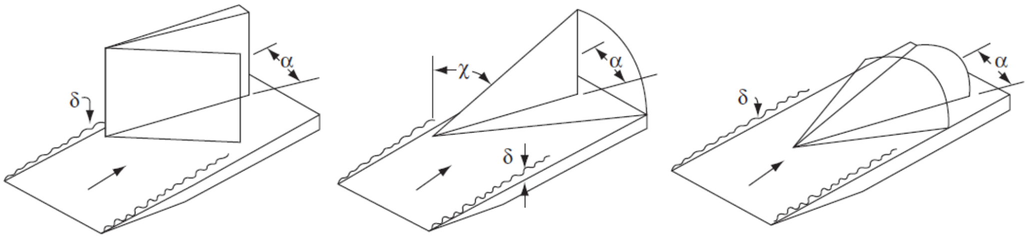

a. Sharp unswept fin (SUF) b. Sharp swept fin (SSF) c. Semicone (SC)

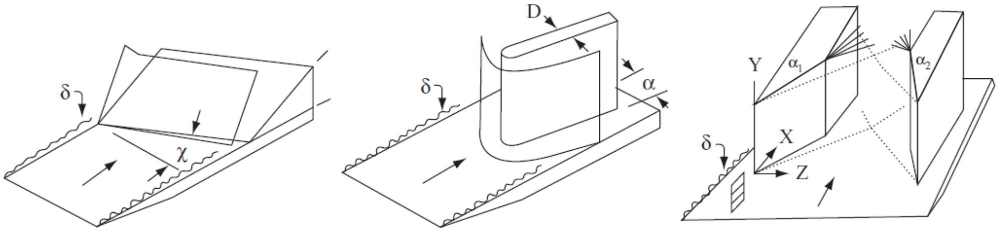

d. Swept compression ramp (SCR) e. Blunt fin (BF) f. Double Sharp fin (DSF)

Figure 1.2: SBLI fundamental geometry - swept shock wave generators [3]

1.2 Boundary Layer Separation

When an adverse pressure gradient of sufficient strength exists within a wall bounded flow, separation of the boundary layer occurs. The adverse pressure gradient is often generated due to geometric changes influencing the flow. In subsonic flows, convex curvature on an airfoil at angle of attack results in an adverse pressure gradient causing separation [4], as seen in Fig. 1.3.

In supersonic and hypersonic flows, concave geometry changes can lead to the formation of shock waves. When a shock wave impinges a boundary layer, complex viscous-inviscid interactions occur which can result in a self-induced adverse pressure gradient so great that the flow separates. The term “incipient separation” is used to describe the boundary layer on the verge of separation.

A hallmark of two-dimensional separation is a closed recirculation bubble which is demarcated by separation and reattachment points. The separation point is defined

Figure 1.3: Flow separation over an airfoil at high angle of attack [5]

as the point where the skin friction is zero or where the change in streamwise velocity in a direction normal to the wall is zero $(\partial u/\partial y)_w = 0$.

An illustrative example of two-dimensional ramp-induced separation is shown in Fig. 1.4. The incoming flow is from left to right, and a boundary layer has formed on the flat plate with a thickness of δ. The ramp at an angle α induces an inviscid, attached shock wave at the corner but, due to the boundary layer, it does not extend down to the plate surface. A pressure rise occurs within the boundary layer resulting in an adverse pressure gradient causing the flow to separate upstream of the corner. Separation causes a dividing streamline to lift off and reattach on the ramp at the aft end of the recirculation bubble. The resulting dividing streamline distorts the inviscid flow field causing two shock waves to form, one near the separation point and one near the reattachment point. The two shock waves interact and merge away from the plate, resulting in the familiar lambda foot.

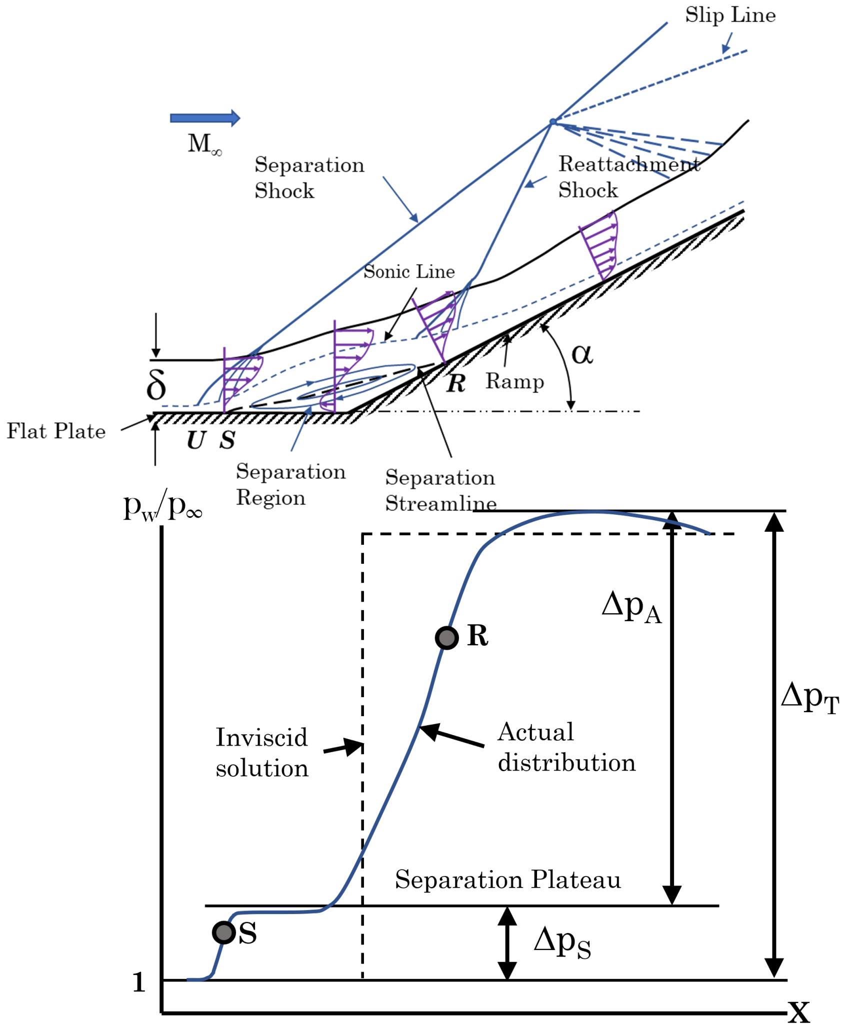

Figure 1.4: Ramp generated shock/boundary layer interaction. Bottom image: normalized surface pressure distribution for ramp generated two-dimensional separation. Modified from [6]

The streamwise normalized wall pressure is informative in studying two-dimensional separation. A schematic of a normalized pressure plot is given in the lower image of Fig. 1.4. Flow is from left to right and shows that the normalized pressure increases as the inviscid shock is encountered. In the absence of viscous effects, the pressure rise would follow the inviscid step function with the pressure instantaneously increasing through the shock. However, due to viscous effects the pressure rise due to the shock wave propagates upstream through the subsonic part of the boundary layer. The point at which the pressure rise first occurs is termed the upstream influence point or interaction origin. The distance between the inviscid solution and the upstream influence point is the upstream influence length, and is a function of Mach, ramp angle, and wall temperature.

A rapid increase in wall pressure is observed between the upstream influence point and flow separation point S. Due to slower moving air within the separation bubble, the pressure on the wall flattens resulting in a pressure plateau before increasing through the reattachment point R. The pressure then reaches a maximum after the reattachment point and remains constant at or near the inviscid solution.

Experimental results for ramp induced SBLI are shown in Fig. 1.5 at Mach 8 [7]. The sequence of images shows increasing ramp angle from top to bottom starting at 27 deg and ending at 36 deg. No separation is observed for ramp angles of 27 and 30 deg, but incipient separation is observed at 33 deg. Significant separation occurs at 36 deg.

Up until this point, we have considered two-dimensional flows. We now turn our attention to three-dimensional flows. Separation in three-dimensions is more complicated than in two. For instance, only in two-dimensional steady flow does separation occur at points of zero skin friction [8]. For typical cases of interest such as those shown in Fig. 1.2, an axial adverse pressure gradient is coupled with a favorable transverse pressure gradient. Thus, the flow, while being slowed axially, can be driven in the transverse direction. The degree that the flow is accelerated in the transverse direction is a balance between the adverse axial and favorable transverse pressure gradients. Therefore, either a closed or an open separation can occur in three-dimensional SBLIs, depending on the sweep. Schematics of these separation flowfields are illustrated in Fig. 1.6 with the left image showing closed separation and

(a) WEDGE ANGLE = 27°

(b) WEDGE ANGLE = 30°

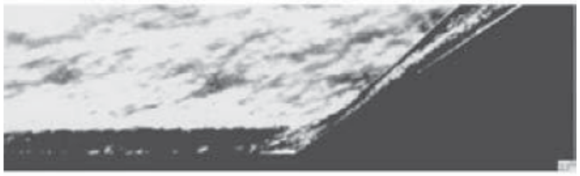

(c) WEDGE ANGLE = 33°

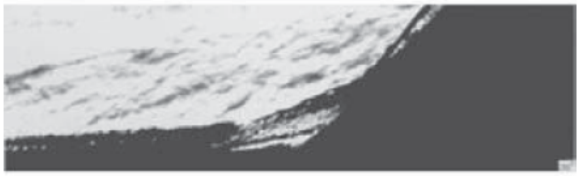

(d) WEDGE ANGLE = 36°

Figure 1.5: Comparison of flow separation due to 2D ramp generated STBLI at Mach 8. No separation at $\alpha = 27$ and 30 deg. Incipient separation at $\alpha = 33$ deg. Pronounced separation at $\alpha = 36$ deg. [7]

the right open separation. For closed separation, streamlines rotate about a common focus F. The bubble is enclosed by the dashed dividing streamline with clearly defined separation and attachment points, S and A respectively. For three-dimensional flow, separation is not just comprised of a streamline, but of a surface and is no longer required to reattach or proceed in the same streamwise direction. The surface can turn in a tangential direction resulting in boundary layer crossflow. Additionally, the recirculation is no longer comprised of closed streamlines, but of stream surfaces which spiral around and are drawn into focus F. The stream surfaces then escape the separation bubble transversely resulting in boundary layer crossflow [6, 9, 10]. In this way, flow separation forms a vortex and, if strong enough, induces further vortices near the surface.

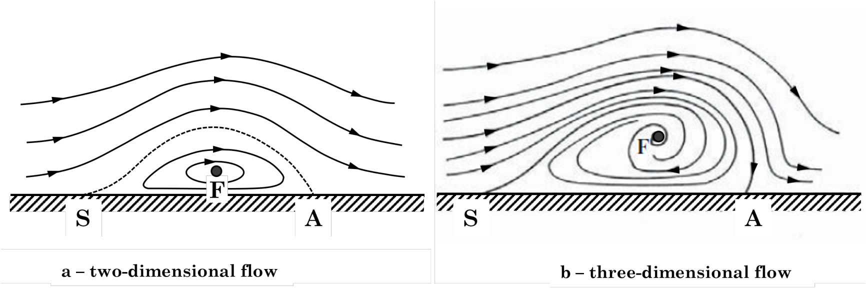

a – two-dimensional flow

b – three-dimensional flow

Figure 1.6: Comparison of open and closed separation. Separation location (S), attachment location (A), focus (F). Modified from [6]

Due to this turning of the flow, the 2D definition of separation fails and it becomes challenging to determine the location of separation and attachment. Rather than use $(\partial u/\partial y)_w = 0$ to mathematically determine the separation location, $(\partial q/\partial y)_w = 0$ is used, where q is the velocity component perpendicular to the separation line [9]. However, this mathematical definition of separation is physically ambiguous. Instead, limiting streamlines can be used to determine separation locations. A limiting streamline is separate from an inviscid streamline, in that a limiting streamline on the surface follows the same direction as a skin friction line, and is a projection of the boundary layer streamlines down to the surface [11, 12]. Maskell [13] proposed that separation occurs when limiting streamlines converge. This results in a separation surface which is initially tangent to the solid body, but then lifts off [9]. Similar to Maskell, Lighthill [14] and Legendre [15] used surface skin friction lines to determine separation locations. Skin friction lines have been shown to coincide with limiting streamlines on a surface [6], and can thus be used to determine separation locations.

Skin friction lines are tangent to the local skin friction vector [6]. The method utilized by Legendre is called critical point theory, since the behavior of skin friction lines near a critical point (that is a point with zero skin friction) is analyzed. Where skin friction lines converge separation is observed, and where they diverge attachment occurs [16].

1.2.1 Swept Fin Shock Wave/Turbulent Boundary Layer Interaction

A sharp swept fin is the geometry under consideration in the present research. A schematic of the geometry is given in Fig. 1.7 and shows the fin mounted on a flat plate. The fin is at an angle α to the flow with a leading edge sweep Λ.

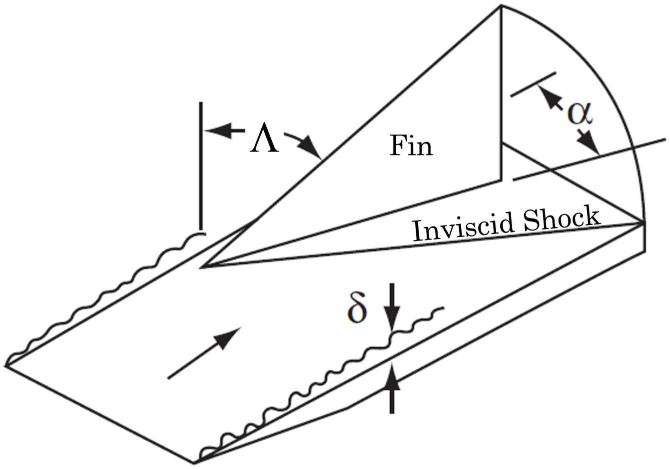

Figure 1.7: Sharp swept fin on a flat plate. From [3]

Similar to the two-dimensional ramp discussed in the previous section, small fin deflections will not cause the flow to separate. At a certain deflection angle, the pressure rise due to the shock will be great enough to cause flow separation. Fin generated SBLI separation leads to key structures not present in two-dimensional separation; however, there are common features. Both two- and three-dimensional separation display upstream influence, but in the case of the swept fin it is defined by a swept line instead of a point. This is seen in Fig. 1.8. In addition, the separation and attachment points are now separation and attachment lines. The upstream influence, separation, and attachment lines all converge at a virtual conical origin (VCO) not at the fin leading edge [17, 18]. A few of these structures are shown in Fig. 1.8. The angled blue line indicates the upstream influence line (UIL), which is present in separated and unseparated flows, and which is where the incoming flow starts encountering the interaction. For separated flows, the UIL is further upstream from the inviscid shock trace on the flat plate compared to unseparated flows. The primary separation line indicated in red occurs downstream of the UIL and is generally straight except for curvature near the fin leading edge. The inviscid shock trace is the shock line if the flow were inviscid, and is between the primary shock and the fin surface. All of these lines come together at a virtual conical origin indicative of quasiconical flow. Demonstrated by Lu, fin-generated interactions possess quasiconical symmetry [17, 18, 19] resulting in relatively constant flow properties along radial lines ahead of the inviscid shock trace which originate at a virtual conical origin [20, 21, 22].

The wall pressure due to swept fin induced flow separation follows a similar trend as that of two-dimensional closed separation. Normalized pressure plots for fins with different leading edge sweep angles at Mach 3 and a 20 degree deflection are shown in Fig. 1.9. Flow is from right to left in a plane normal to the fin surface. Rather than plot versus a distance from the fin, the pressure is plotted against an angle relative to the fin using the VCO as the point of rotation.

Moving from right to left in Figure 1.9, we have the initial pressure rise associated with the upstream influence location. The pressure continues to rise through the separation point, reaching a plateau pressure within the separation area. Following

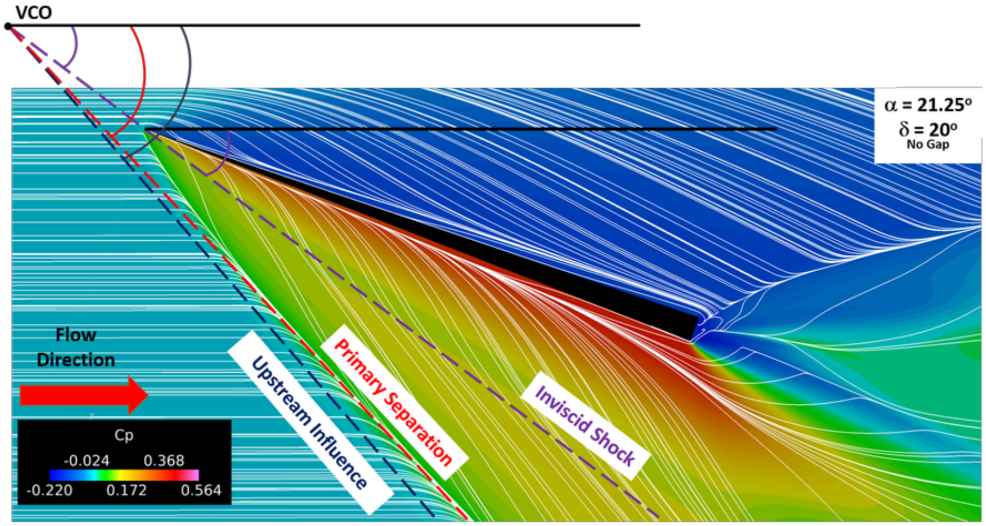

Figure 1.8: Illustration of virtual conical origin showing upstream influence (blue), primary separation (red), and inviscid shock trace (purple). Mach 2.5, $\delta = 20\,\mathrm{deg}$, $\Lambda = 60\,\mathrm{deg}$. Plate colored by C_p.

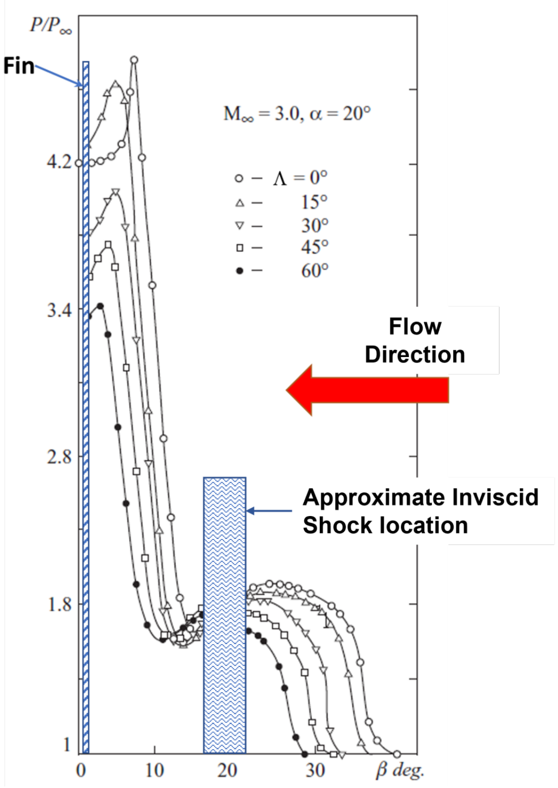

Figure 1.9: Pressure ratio vs fin leading edge sweep angle. From Zheltovodov [3].

the plateau pressure, a local minimum occurs due to strong vortical flow associated with open separation. The pressure rises until it reaches a maximum at the attachment location. A decrease in pressure due to the inviscid boundary conditions follows the attachment location until the fin surface is reached.

1.2.2 Inviscid Shock Angle

Unlike two-dimensional flows or flow over three-dimensional unswept fins, the shock angle of a swept fin cannot be determined using simple oblique shock relations for a wedge. The sweep of the fin results in a shock which more closely follows conical shock theory. This feature was observed by Richards [23] in his work on supersonic delta wings. Using experimental results for a swept delta wing, he compared the resulting shock angle to wedge, cone, tangent wedge, and thin shock-layer theory. Figure 1.10 plots the shock angle versus incident angle for the tested theories and for the delta wing at Mach 2.5. Note that the shock angle (θ_s in Fig. 1.10) is measured from the windward fin surface and the flow incidence (α in Fig. 1.10) is measured from the flat leeward surface.

A schematic of the labeled delta wing is given in Fig. 1.11. Results plotted in Fig. 1.10 are for a wedge angle of $\theta = 7.5\,\mathrm{deg}$, and the delta wing leading-edge sweep $\Lambda = 70\,\mathrm{deg}$. Note: Richards uses the notation μ to denote wedge angle.

Due to the inability to use theory to compute the inviscid shock angle, it was determined using CFD with an inviscid solver. The inviscid shock line could be determined by measuring surface streaklines and pressure contours. Since Richards measured α from the flat leeward surface and $\theta_{1/2}$ is nonzero, the flow deflection α is the sum of the fin deflection δ and $\theta_{1/2}$. The inviscid solution at $\delta = 12\,\mathrm{deg}$ ($\alpha = 13.25\,\mathrm{deg}$) is shown in Fig. 1.12, with the flow direction indicated by the red arrow. The surface is colored by c_p, and Euler-based limiting streamlines are added.

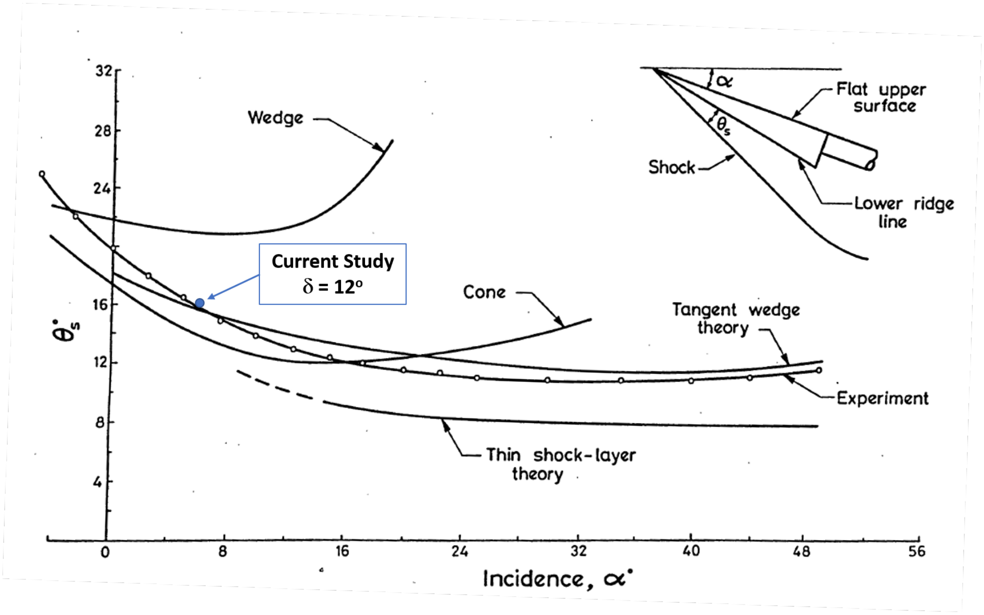

Figure 1.10: Shock angle versus incident angle for a delta wing with a leading-edge sweep Λ=70 deg at $M_\infty = 2.5$. From Richards [23]. Point is swept fin result, $\delta = 12\,\text{deg}$, $\Lambda = 60\,\text{deg}$.

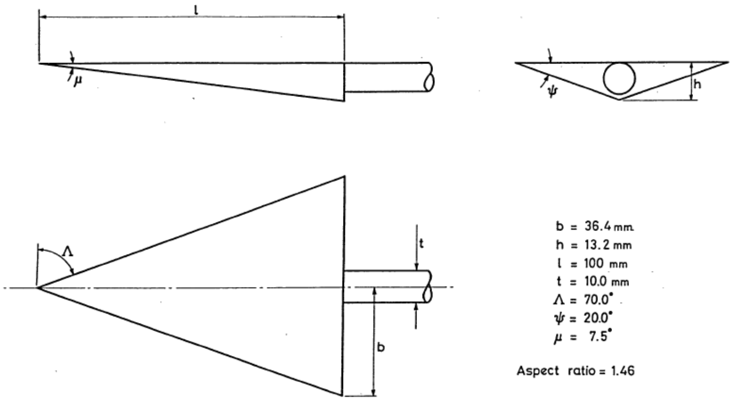

Figure 1.11: Schematic of delta wing geometry studied by Richards [23]. Note: Richards uses the notation μ to denote wedge angle.

The inviscid shock wave trace on the flat plate due to the fin deflection is readily apparent when observing the streamlines and surface c_p. The black dashed line in Fig. 1.12 indicates the location of the inviscid shock wave. The blue long-dashed line indicates the location a shock wave computed used conical shock methods would lie, and the red dashed line is the oblique shock solution. The swept fin shock is between the two theories, which is as predicted by Richards [23], as shown in Fig. 1.10. The angles in Fig. 1.12 are relative to the fin surface, not freestream or fin centerline. The inviscid shock angles from Fig. 1.12 are plotted on Fig. 1.10, and closely follow results obtained by Richards.

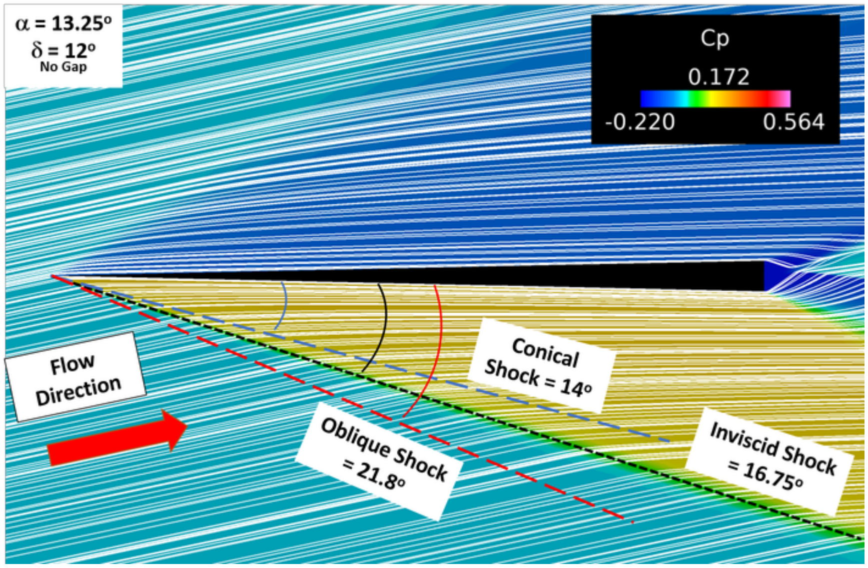

Figure 1.12: Pressure coefficient contour and limiting streamlines from an Euler solution, $M = 2.5$, $\delta = 12\,\text{deg}$, $\Lambda = 60\,\text{deg}$

1.3 Flow on Leeward Side of Fin

The flow field on the leeward side of a delta wing has been thoroughly investigated [23, 24, 25, 26, 27, 28, 29, 30, 31, 32, 33]. However, the flow field on the leeward side of a fin undergoing STBLI is relatively unexplored. One of the few studies connecting the two areas was performed by Seshardi and Narayan [27] who noted the similarity between quasiconical flow generated due to swept shock SBLI and the flow on the leeside of a delta wing.

Generally, interest in fin-generated SBLI has been on the windward side. While there have been studies of delta wing/body junction flows such as [34], most studies tend to study the wing in isolation. A comprehensive treatment of both sides of the fin has rarely been performed. Recent studies by Otten and Lu [22, 35, 36] presented preliminary results combining the two areas of study. Further, for flight vehicles which use deflecting fins as control surfaces, there is a desire to understand the flow field on both sides of the fin.

1.3.1 Vortex Dynamics

In Chapter 4, the leeward side will be discussed in more detail. It is beneficial to briefly discuss vortices prior to reading those sections. The reader is reminded of the Helmholtz vorticity theorems [8, 37, 38]:

1. The integrated vorticity flux over a cross surface of a vorticity tube or the circulation of the tube is constant, independent of the shape and location of the cross surface or its boundary over which the integrals are estimated [38]
2. If and only if the flow is circulation-preserving, a material vorticity tube will move with the fluid [38]
3. Vorticity tubes are time-invariant [38]

Theorem One leads to the fact that vorticity tubes cannot terminate in a fluid: they must either terminate at a fluid-fluid interface or form a closed path. Also vorticity tubes cannot terminate on a non-rotating solid boundary where the no-slip condition holds. Vorticity lines, however, may terminate this way. The third theorem means that a fluid element without vorticity will remain without vorticity. Due to viscosity, boundary layers contain vorticity. When a boundary layer separates, the viscosity is transported to the free shear layer [37] and a vortex can form. This is the mechanism by which vortices form on the leeside of the fin, and will be discussed in more detail in Chapter 4.

CHAPTER 2

LITERATURE REVIEW

A significant amount of SBLI research on two- and three-dimensional geometries has been performed for 80 years. Research has focused on simple geometries where the interaction develops on planar, two- and three-dimensional geometries [19, 39, 40, 41, 42, 43, 44, 45, 46, 47]. Impinging shocks, compression ramps, and sharp fins on flat plates comprise a significant portion of the studied configurations. Examples of these were presented as Fig. 1.2 in Chapter 1.

2.1 Quasiconical Studies

It was found that fin-generated interactions possess quasiconical symmetry [17, 18, 19, 48]. In quasiconical symmetry, flow properties ahead of the inviscid shock trace are relatively constant along radial lines which originate at a virtual conical origin. The radial lines are curved in the inception region near the fin apex, but straight further from the apex [49, 50].

2.2 Three-Dimensional Studies

More complex experiments utilizing missile geometries by Neumann and Hayes [51], Kussoy and Horstman [52], and more recently by Fano et al. [53, 54] and Pickles et al. [55, 56, 57] have been carried out to study three-dimensional SBLI on nonplanar surfaces. Kussoy and Horstman investigated three-dimensional flow over a missile with either a flare or a sharp fin [52] to determine both heating and pressure effects. Pickles et al. found that unlike planar interactions, the surface limiting streamlines on a cylindrical body exhibit an inward tilt towards the fin root with smaller overall compression across the SBTLI [57]. Micro vortex generators were demonstrated to be effective in reducing the separation vortex size, or even eliminate it [58, 59].

Practical missile configurations contain a gap between the body and the fin. The effect of gap on control or fin effectiveness has been investigated by many authors [53, 60, 61, 62, 63, 64, 65, 66, 67, 68, 69]. Limited studies have been performed to determine the gap effect on SBLI in both planar or axisymmetric geometries, with studies to determine the effect of gap on heating seeing some attention. Neumann and Hayes [51], Fano et al. [53], and Zhang et al. [63] focused on the heating caused by the STBLI when the boundary layer enters the gap and interacts with the shock from the fin leading edge and fin support [51, 53]. The location of highest heating was found to be directly ahead of the fin support [51, 53], and there is a proportional relationship between increasing gap height and increasing heating [63].

Geometries where a gap exists between the missile body and the fin were studied by Dahlke and Pettis [61] to determine the effect of a gap on fin performance. They found that the gap reduces the normal force produced by the fin. Comparisons between a fin on a flat plate to a fin on a missile body at several angles of attack and deflection angles were performed by Allen [60]. He found that the effect of the body on the fin loads was to produce a small positive increment in normal force and bending moment, without impacting hinge moment [60]. Additionally, Allen varied the gap between the fin and the flat plate between 0.01–0.05 in which are less than the height of the undisturbed boundary layer. These gaps did not have an appreciable effect on the fin loads when the gap was changed [60]. Otten and Lu [22] numerically investigated incipient STBLI generated by a sharp swept fin mounted above a flat plate both with and without gaps. The increasing gap was found to reduce the interaction strength due to flow leakage under the fin without changing the inviscid shock angle. No significant changes in the upstream influence line, primary separation, or attachment angles were observed either. In a follow-on study by Otten and Lu [70], the effect of gap height on fin normal force, root bending moment, and hinge moment was studied. They found that increasing the fin/plate gap is to decrease fin effectiveness.

2.3 Incipient Separation

A commonly used empirical relation to determine the flow incidence angle required for incipient separation due to SBLI of an unswept fin is the Korkegi criterion [71, 72]

$$M_\infty \alpha_i = 0.3 \tag{2.1}$$

(with the angle α in radians). The Korkegi criterion has demonstrated its applicability for unswept fins. However since it does not take into account Reynolds number or shape factor dependencies, the criterion should be viewed as a guideline rather than a rule [3]. Lu observed separation at shock strengths less than that predicted by Korkegi [19]. Lu and Settles recommended that Korkegi's criterion be re-interpreted to mean that significant separation occurs above α_i instead of separation to start at that flow deflection angle [73]. Two-dimensional free interaction theory (FIT) using the Mach number normal to the inviscid shock rather than the freestream Mach number can also be used to determine incipient separation [3]. FIT indicates that the incipient Mach number normal to the inviscid shock trace on the surface is

$$M_{ni} = 1.24 - 1.26 \tag{2.2}$$

and the corresponding pressure rise

$$\xi_i \equiv \left(\frac{p_2}{p_1}\right)_i = 1.62 - 1.69 \tag{2.3}$$

over a range of $Re_\theta = 1.4\text{–}2.3 \times 10^4$. This is depicted graphically in Fig. 2.1, where M_i and ξ_i indicate the Mach number and pressure ratio respectively for incipient separation. Using the approximate ξ_i values in Eq. 2.3 and the FIT equation from [2], the normal Mach number required for incipient M_{ni} can be determined from

$$\frac{p_{plat}}{p_\infty} = kM_{ni}^2 \left(M_{ni}^2 - 1\right)^{-1/4} c_f^{1/2} + 1, \tag{2.4}$$

where p_{plat} is the plateau pressure, c_f is the skin friction coefficient upstream of the fin, and k is an experimentally established constant. From Zheltovodov [3, 74] k in Eq. 2.4 ranges from 5.94 to 7.4 and varies inversely with the Reynolds number.

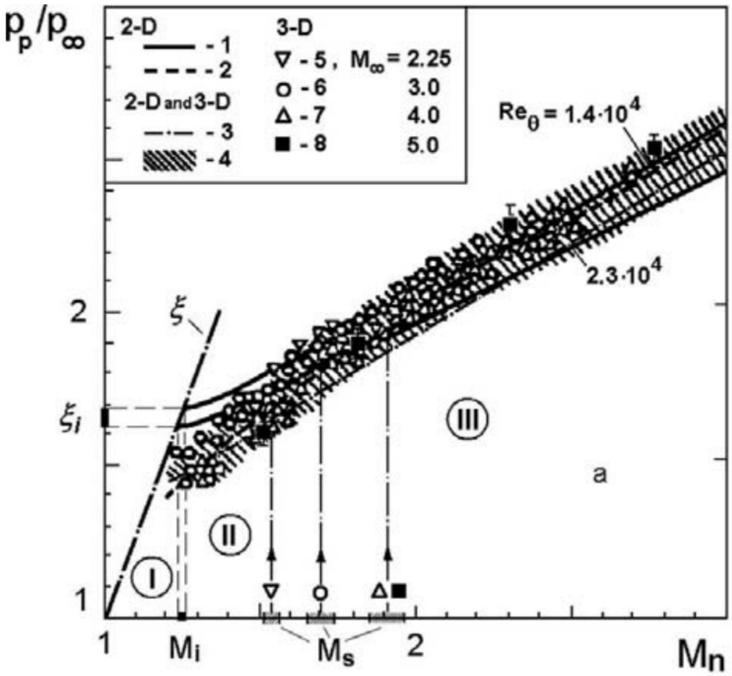

Figure 2.1: Plateau pressure versus Mach number normal to inviscid shock. From [3]

One of the ways to determine separation location and other flow features in shock/boundary layer interaction is through surface-flow visualization techniques. Limiting streamlines and surface streaklines are commonly encountered in CFD. The current study makes use of surface streaklines, as computed in FieldView, and will be discussed further in Chapter 3. Typically, converging surface streaklines indicate locations of flow separation, and diverging streamlines flow attachment [12, 14, 75]. Based on the lines of separation and attachment, Zheltovodov [3] identified six different flow regimes, as shown in Fig. 2.2. No separation occurs in Regime I, with the line separating Regimes I and II determined by the Korkegi criterion. Starting in Regime III, secondary separation lines appear withing the SBLI interaction region. In Regime V the secondary separation line was observed to disappear, reappearing in Regime VI along with a secondary attachment line.

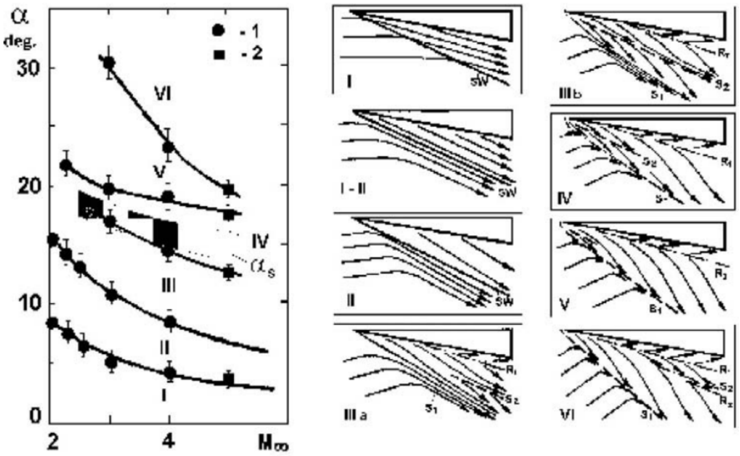

Figure 2.2: SBLI Regimes of Zheltovodov [3]. No SBLI occurs in Regime I. The border between Regimes I and II indicate incipient separation. Regimes III to VI display multiple separation (e.g., S_1 and S_2) and/or attachment (e.g., R_1 and R_2) lines.

2.3.1 Swept Fin Shock/Turbulent Boundary Layer Interaction

While fins with leading-edge sweep are preferred in high-speed missile applications, few studies have been carried out on STBLI generated by a fin with leading-edge sweep. The few studies showed that the flow-field structure and interaction regimes are qualitatively similar for both swept and unswept fins [3, 18], as shown in Fig. 2.3. For an increase in leading-edge sweep angle, while holding fin angle and freestream Mach number constant, a weakening of the shock wave occurs. This decreases (1) the extent of the interaction, whether separated or not, in angular terms, (2) the surface pressure levels at the maximum peak attachment line close to the fin and (3) the plateau pressure level for separated interactions. The smaller angular extent of the separated interaction means that the attachment location is squeezed closer to the fin junction. Previous work by Zheltovodov et al. [76] found that for a swept fin, the critical Mach number $M_n = M_i$, and the critical shock-wave strength $\xi = \xi_i$ corresponding to Stanbrook's interaction regime were largely independent of sweep angle at moderate supersonic Mach numbers.

An example of fin induced shock-wave/turbulent boundary layer interactions with lines of separation and attachment emanating from a virtual conical origin VCO away from the fin is shown in Fig. 2.5 and by a schematic in 2.4. The upstream location where the incoming flow starts to interact with the shock is known as the upstream influence line (UIL). In Fig. 2.4 the UIL is indicated by the straight black dashed line. With the farfield possessing conical symmetry, the UIL would then appear to emanate from a VCO, while the actual upstream influence curves toward the fin tip. Directly downstream of the UIL is the primary separation line which also shows conical farfield behavior and nonconical nearfield behavior. Within the separation region is the inviscid shock trace which is the shock wave line if the flow were inviscid. The inviscid shock takes on a conical shape for a swept fin, as shown in Fig. 2.5. The inviscid shock trace with the farfield UIL and separation line come together at the VCO. When a shock is sufficiently strong, a secondary separation zone appears [3, 77].

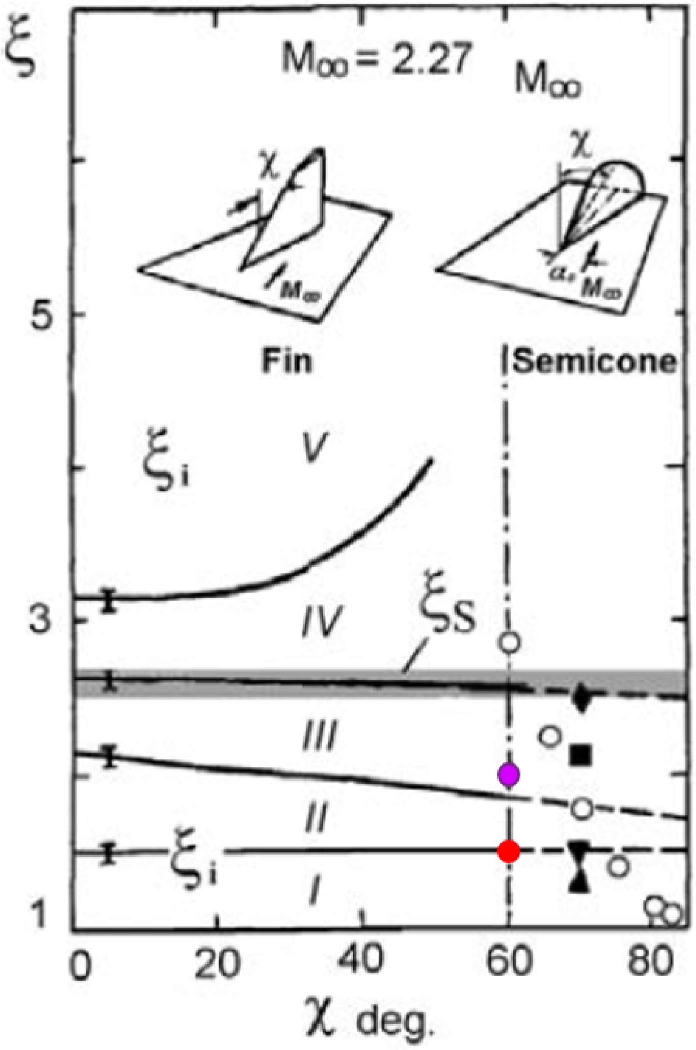

Figure 2.3: SBLI Regimes of Zheltovodov [3] for Sharp Swept Fins and Semicone at Mach 2.27: open symbols - symmetric flow over semi-cone (α_0=0), closed symbols - asymmetric flow ($\alpha_0 > 0$)

The upstream influence line can be easily determined by plotting the wall pressure normalized by the freestream pressure versus β. The UIL is found by locating the angle at which the normalized wall pressure increases from unity. Figure 2.6 plots the normalized wall pressure for a fin deflection of 20 deg. Flow is from right to left, starting just outside the UIL and ending at the fin surface. For δ = 20 deg the UIL

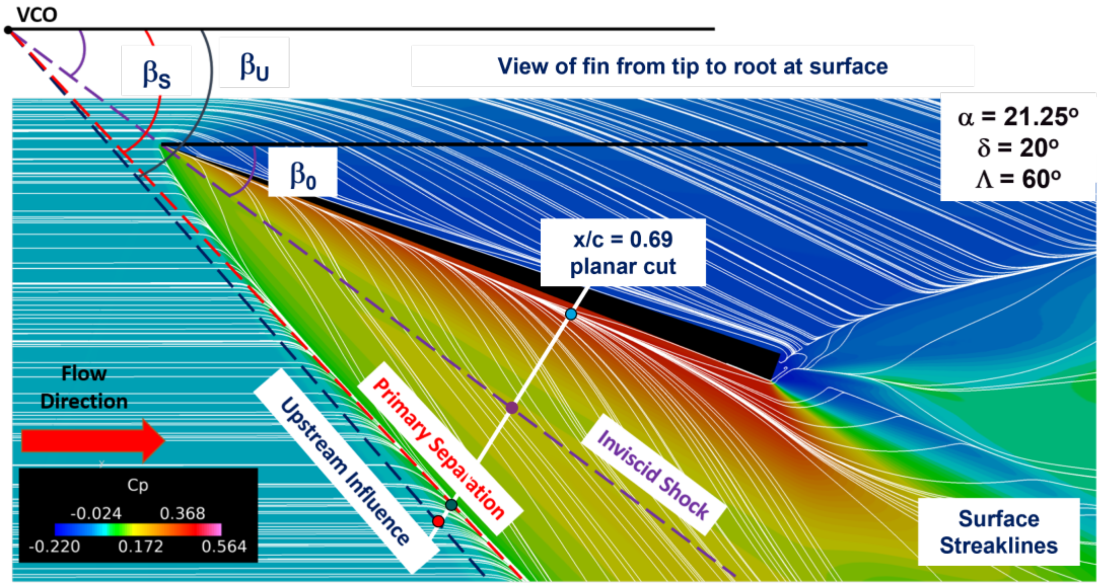

Figure 2.4: Illustration of virtual conical origin showing upstream influence (blue), primary separation (red), and inviscid shock trace (purple). Mach 2.5, $\delta = 20\,$deg, $\Lambda = 60\,$deg. Plate colored by c_p.

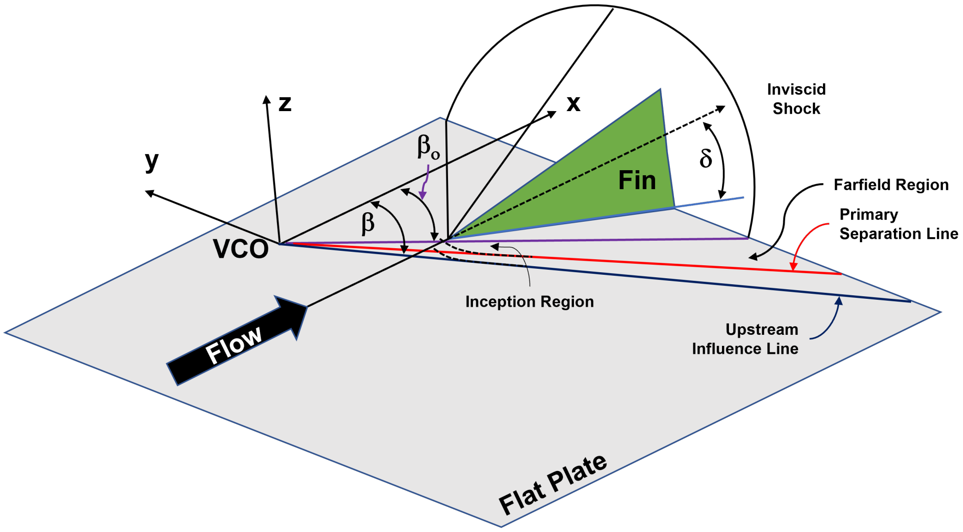

Figure 2.5: Schematic of Swept Fin on Flat Plate

occurs around $\beta - \alpha = 28$ deg, the separation is at $\beta - \alpha = 25$ deg, and the inviscid shock is at $\beta - \alpha = 17$ deg. In Fig. 2.6, the location of the UIL is marked by a circle and denoted by UI. The location of the separation line is labeled 'S', inviscid shock location is 'I', and the attachment point is labeled 'A'.

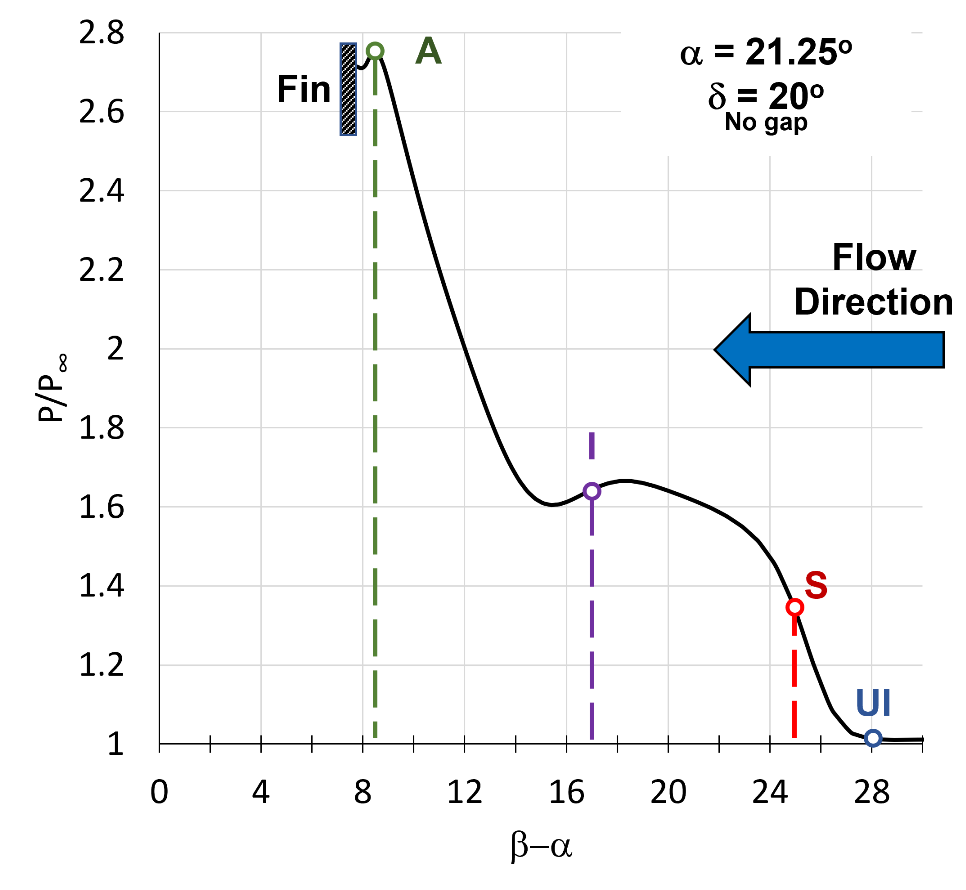

Figure 2.6: Normalized surface pressure with points for attachment (green, A), inviscid shock (purple, I), separation (red, S), and upstream influence (blue, UI). Mach 2.5, $\delta = 20$, no gap.

2.3.2 Computational Advancements

The complex viscous–inviscid interaction between a shock and a turbulent boundary layer poses a challenge for computational fluid dynamics. A combination of advanced numerical methods, powerful computational hardware and better understanding of the flow physics has led to improved numerical modeling over the past two decades [45, 46, 78, 79, 80, 81, 82, 83, 84, 85]. As recent as 2010, at an SBLI workshop during the 48th AIAA Aerospace Sciences Meeting, it was determined that CFD consistently failed to agree with experiment [78, 86]. Specifically, DeBonis et al. [86] conducted a thorough examination of CFD methods for the solution of impinging shock SBLI. In their study, they compared six different RANS turbulence closure models to hybrid LES/RANS and LES methods. They found in general RANS and LES methods have the same level of error. Depending on the LES method, it could have more error or less error than RANS when predicting streamwise and transverse velocity. The only area LES consistently outperformed RANS was in predicting normal stress. The authors concluded that since RANS is more mature than LES, there is more room for improvement for LES and thus with further development could in the future consistently outperform RANS. More recently, dramatic advancements have resulted in improved agreement between experiment and computation, allowing for detailed computational study of the flow field within the interaction region [53, 63, 87, 88, 89, 90, 91, 92].

Several computational studies have been performed to evaluate the accuracy of RANS methods with different turbulence models applied to shock-wave/turbulent boundary layer interaction [3, 79, 93, 94, 95, 96]. In general, for weak to moderate interactions ($\alpha < 20$ deg), the surface pressure, heat transfer, and primary separation location are accurately captured with RANS computational methods [79]. However, as steady RANS cannot capture the high level of unsteadiness seen in shock systems undergoing strong interactions, secondary separation is rarely observed [3], and surface pressures, heat transfer, and primary separation location are not accurately computed [79]. Additionally, solve-to-the-wall results are more accurate than wall-function results [3].

Further studies by Gaitonde [96] found that RANS methods are able to accurately model the mean 3-D flowfield. Flow away from walls can be considered inviscid, and independent of eddy viscosity. Once flow separates, it becomes practically inviscid rotational and thus also independent of eddy viscosity when away from the wall. The vorticity distribution in flow downstream of separation primarily depends on the its distribution in the incoming boundary layer [96]. Since RANS methods are designed to, and have been shown to, accurately capture the vorticity within a boundary layer, RANS methods can accurately reproduce the overall mean flow. RANS has even demonstrated its ability to accurately model surface oil flow and pressure [96].

From the findings of DeBonis [86] and Gaitonde [96] and the computational cost and complexity associated with LES methods, this research utilized RANS based CFD instead of LES.

2.4 Motivation and Scope of the Present Study

While many studies, such as those listed previously, have been carried out on sharp unswept fins, expanding the understanding of STBLI to swept fins is of great interest. In practice, high-speed vehicles, such as missiles and aircraft, use swept fins. Therefore, the present study is conducted to further the understanding of swept STBLI induced by a sharp swept fin. In an effort towards greater practicality, the presence of a gap between the fin and surface is introduced with the resulting STBLI characterized. This includes how the gap and sweep affect incipient separation. Due to the weakening of the shock from the swept fin, it is hypothesized that the sweep will necessitate a higher deflection angle before incipient separation is seen. The gap will cause a pressure relief within the separation region, further weakening the interaction. If the pressure relief is significant, this could require a higher angle before incipient separation is observed. When the fin is placed on a body of revolution it is expected that the body will provide some relief in the SBLI region, but that the SBLI structure will be similar to the flat plate case.

This study's objectives are as follows:

- validate the RANS turbulence closure model and numerical solver against experimental and theoretical results
- study STBLI and underlying physics associated with a swept fin-induced shock wave/turbulent boundary layer interaction on a flat plate by numerical simulations
- study STBLI and underlying physics associated with a swept fin-induced shock wave/turbulent boundary layer interaction when a gap is introduced between a fin and flat plate by numerical simulations
- study STBLI and the underlying physics associated with a swept fin-induced shock wave/turbulent boundary layer interaction on a body of revolution by numerical simulations

In accomplishing the above, additional areas of study presented themselves. These were:

- qualitative comparison between the leeside of a fin and delta wing
- RANS to DES CFD comparison for moderate interactions

Both the primary and secondary research objectives will be discussed in detail in Chapter 4

CHAPTER 3

NUMERICAL SCHEME

Previously, engineers only had experiments and theory to analyze their designs. The advent of computation fluid dynamics (CFD) added a third arrow to the engineers quiver of tools. A significant advantage of CFD is its ability to provide unprecedented flowfield detail which allows for in-depth analysis of fluid mechanics and processes. This is augmented by providing previously unobtainable flow visualization. With the plethora of information available from CFD, one must be discerning with the data or risk becoming overwhelmed. Over the years, advances in CFD have enabled engineers to analyze the aerodynamic characteristics of more and more complex vehicles as well as study the underlying flow physics. CFD involves pre-processing, solving, and post-processing. During pre-processing, the geometry is defined and/or refined, a mesh or grid is generated, and the necessary physics models are determined. A numerical scheme for solving partial differential equations is then utilized, followed by analyzing the results during post-processing.

This chapter discusses the first two components of CFD: pre-processing and the numerical method for acquiring the solution. The governing equations are presented in Sec. 3.1 including the turbulence closure model in Sec. 3.1.1. During this study structured meshes were generated using Pointwise 18.4R4, a solution was obtained using the commercial software ICFD++ v19 by Metacomp, and results were post-processed using FieldView, MATLAB, and Python. CFD++ is discussed in Sec. 3.2. The geometry used in this study is presented in Sec. 3.3.1 and numerical results of the flow over the flat plate are given in Sec. 3.3. The chapter closes with grid convergence results in Sec. 3.4.

3.1 Governing Equations

CFD++ solves the three-dimensional Navier–Stokes equations as outlined by Palaniswamy, et al. [97], which for a single species without a source term is

$$\frac{\partial \boldsymbol{Q}}{\partial t} + \frac{\partial}{\partial x}\left(\boldsymbol{F}_1 + \boldsymbol{G}_1\right) + \frac{\partial}{\partial y}\left(\boldsymbol{F}_2 + \boldsymbol{G}_2\right) + \frac{\partial}{\partial z}\left(\boldsymbol{F}_3 + \boldsymbol{G}_3\right) = 0 \tag{3.1}$$

where $\boldsymbol{Q}$ is the dependent variable vector; the inviscid flux vectors are $\boldsymbol{F}_1$, $\boldsymbol{F}_2$ and $\boldsymbol{F}_3$, and $\boldsymbol{G}_1$, $\boldsymbol{G}_2$, and $\boldsymbol{G}_3$ are viscous flux vectors. The dependent variable vector and inviscid fluxes are given as

$$\boldsymbol{Q} = \begin{bmatrix} E \\ \rho \\ \rho u \\ \rho v \\ \rho w \end{bmatrix} \qquad \boldsymbol{F}_1 = \begin{bmatrix} (E+p)\,u \\ \rho u \\ \rho u^2 + p \\ \rho v u \\ \rho w u \end{bmatrix} \quad \boldsymbol{F}_2 = \begin{bmatrix} (E+p)\,v \\ \rho v \\ \rho u v \\ \rho v^2 + p \\ \rho w v \end{bmatrix} \quad \boldsymbol{F}_3 = \begin{bmatrix} (E+p)\,w \\ \rho w \\ \rho u w \\ \rho v w \\ \rho w^2 + p \end{bmatrix}$$

where E is the total energy, ρ is density, p is pressure, and u, v, and w are the velocity components in the x, y, and z directions respectively [98]. The viscous flux vectors are

$$\boldsymbol{G}_1 = \begin{bmatrix} q_x - u\tau_{xx} - v\tau_{xy} - w\tau_{xz} \\ 0 \\ -\tau_{xx} \\ -\tau_{xy} \\ -\tau_{xz} \end{bmatrix} \quad \boldsymbol{G}_2 = \begin{bmatrix} q_y - u\tau_{yx} - v\tau_{yy} - w\tau_{yz} \\ 0 \\ -\tau_{yx} \\ -\tau_{yy} \\ -\tau_{yz} \end{bmatrix}$$

$$\boldsymbol{G}_3 = \begin{bmatrix} q_z - u\tau_{zx} - v\tau_{zy} - w\tau_{zz} \\ 0 \\ -\tau_{zx} \\ -\tau_{zy} \\ -\tau_{zz} \end{bmatrix}$$

with the stresses given as

$$\tau_{xx} = 2\mu\frac{\partial u}{\partial x} - \frac{2}{3}\mu\Phi \tag{3.2}$$

$$\tau_{yy} = 2\mu\frac{\partial v}{\partial y} - \frac{2}{3}\mu\Phi \tag{3.3}$$

$$\tau_{zz} = 2\mu\frac{\partial w}{\partial z} - \frac{2}{3}\mu\Phi \tag{3.4}$$

$$\tau_{xy} = \tau_{yx} = \mu\left(\frac{\partial u}{\partial y} + \frac{\partial v}{\partial x}\right) \tag{3.5}$$

$$\tau_{xz} = \tau_{zx} = \mu\left(\frac{\partial u}{\partial z} + \frac{\partial w}{\partial x}\right) \tag{3.6}$$

$$\tau_{yz} = \tau_{zy} = \mu\left(\frac{\partial w}{\partial y} + \frac{\partial v}{\partial z}\right) \tag{3.7}$$

where μ is the laminar viscosity and Φ the dilation

$$\Phi = \left(\frac{\partial u}{\partial x} + \frac{\partial v}{\partial y} + \frac{\partial w}{\partial z}\right). \tag{3.8}$$

The last unknown variable in the viscous flux vector is the heat transfer q. It is determined following Fourier's law

$$q_x = -k\frac{\partial T}{\partial x} \tag{3.9}$$

$$q_y = -k\frac{\partial T}{\partial y} \tag{3.10}$$

$$q_z = -k\frac{\partial T}{\partial z}. \tag{3.11}$$

In CFD++, the energy equation is written as total energy

$$E = \rho H - p \tag{3.12}$$

where H is the total enthalpy. Due to the complexity of the energy equation, the author leaves it as an exercise to the reader to see the excellent discussion of provided by Tannehill et al. [99].

To close the solution of the Navier–Stokes equation, for a perfect gas, CFD++ uses the equation of state

$$p = \rho R T \tag{3.13}$$

or

$$E = \frac{p}{\gamma - 1} + \frac{1}{2}\rho\left(u^2 + v^2 + w^2\right) \tag{3.14}$$

where $\gamma = C_p/C_v = 1.4$ and $R = C_p - C_v = 287$ J/(kg.K). As the gas is assumed to be thermally perfect, the ratio of specific heats is constant. Sutherland's law is used to compute both the viscosity and thermal conductivity as

$$\frac{\mu}{\mu_0} = \left(\frac{T}{T_{0\mu}}\right)^{1.5} \frac{T_{0\mu} + S_\mu}{T + S_\mu} \tag{3.15}$$

$$\frac{k}{k_0} = \left(\frac{T}{T_{0k}}\right)^{1.5} \frac{T_{0k} + S_k}{T + S_k} \tag{3.16}$$

where $T_{0\mu} = T_{0k} = 273.15$ K are reference temperatures, $\mu_0 = 1.715 \times 10^{-5}$ kg/(m.s) and $k_0 = 0.0241$W/(m.K) are the coefficients of viscosity and thermal conductivity respectively at the reference temperature, and $S_\mu = 110.4$K and $S_k = 194$K are the Sutherland constants [100].

3.1.1 Turbulence Model

In turbulent flows, the timescale for eddies vary with

$$\tau_t\left(l\right) = \left(l^2/\epsilon\right)^{1/3} \tag{3.17}$$

where l is the eddy size and ϵ is the rate of change of turbulence kinetic energy [101]. The eddy size can range from meters down to the Kolmogorov length scale η_k, where

$$\eta_k = \left(\nu/\epsilon\right)^{1/4}, \tag{3.18}$$

and roughly varies with

$$\eta_k/l \approx Re^{-3/4} \tag{3.19}$$

[101]. From Eq. 3.19 the Kolmogorov length scale can be between the order of millimeters to micrometers. If the range of length scales is micrometers to meters, then time scales span from nanoseconds to milliseconds. Due to these large ranges of time and length scales present, the numerical solution of the full Navier–Stokes equations where turbulence is directly solved is intractable for simple geometries and becomes impossible when modeling complex geometries. Additionally, in order to resolve the Kolmogorov length scale requires the computational cells to be on the order of η_k. Coupled with the requirement to limit the time step to approximately $\eta_k/20$ [101], can result in multi-year simulations for simple geometries. To simplify the problem, turbulence can be represented in the Navier–Stokes equations as the sum of the mean (time-averaged or time-varying) and fluctuating portions of turbulence [102]. The new expression is then itself time-averaged. This results in a statistically steady solution with a steady mean flow and the only source of unsteadiness being turbulence [98]. In addition, the Reynolds equations are used to solve for the mean velocity. This requires the knowing the Reynolds stresses, which are obtained used a turbulent-viscosity or turbulence closure model.

Several closure models have been developed over the years, such as algebraic (e.g. Cebeci-Smith and Patankar-Spalding) and transport-equation (e.g. Spalart-Allmaras, κ–ϵ, κ–ω, and SST) turbulence models. For this study the steady RANS Menter SST κ–ω turbulence closure model was employed. Menter developed the shear stress transport SST model by careful combination of the κ–ω and k–ϵ turbulence models allowing each to contribute their individual strengths [102, 103]. The SST model utilizes κ–ω in the boundary layer's inner region, and κ–ϵ in the free-stream and free shear regions of the flow. By using κ–ϵ in the free-stream, SST does not display the same sensitivity to the free-stream as κ–ω. As κ–ω does not involve damping functions and uses simple Dirichlet boundary conditions, it exhibits excellent numerical stability. For these reasons, and its demonstrated accuracy in predicting mean flow profiles, κ–ω was chosen by Menter [103] to model the boundary layer inner region.

Prior to combining the two models, Menter had to first cast them into similar forms. To achieve this, the κ–ϵ equations were transformed into the κ–ω form. It was also required to introduce additional cross-diffusion to the ω term within the κ–ω model. A blending function was utilized to blend the two models in the wake region of the boundary layer. Since eddy viscosity models were known to underestimate the transport of turbulent shear stress (affecting adverse pressure gradient flows), Menter also modified the definition eddy viscosity [102]. This modification improved predictions for flows with adverse pressure gradients over the Wilcox κ–ω turbulence model [103]. As this modified definition was only required in the boundary layer, Menter employed a second blending function to use the original formulation of eddy viscosity in free shear or free-stream flows, limiting the modified eddy viscosity definition to wall bounded flows [103].

From the Metacomp CFD++ users manual [98], the implementation of the SST turbulence closure model in CFD++ is as follows. First, Reynolds stresses are defined as

$$\rho\overline{u_i u_j} = \frac{2}{3}\delta_{ij}\rho k - \mu_t S_{ij} \tag{3.20}$$

where S_{ij} is the mean strain

$$S_{ij} = \left(\frac{\partial U_i}{\partial x_j} + \frac{\partial U_j}{\partial x_i} - \frac{2}{3}\frac{\partial U_k}{\partial x_k}\delta_{ij}\right). \tag{3.21}$$

A constant is added to the eddy-viscosity term and is given by

$$\nu_t = \frac{a_1 k}{\max\left(a_1\omega, SF_2\right)} \tag{3.22}$$

where $a_1 = 0.31$ and F_2 is the second blending function

$$F_2 = \tanh\left\{\left[\max\left(\frac{2\sqrt{k}}{\beta^*\omega d}, \frac{500\nu}{d^2\omega}\right)\right]^2\right\} \tag{3.23}$$

with d the distance to the nearest wall and $\nu = \mu/\rho$. This leads to turbulence generation or production

$$\begin{aligned} P_k =& \rho\overline{u_i u_j}\frac{\partial U_i}{\partial x_j} && (3.24)\\ =& \left[\mu_t\left(\frac{\partial U_i}{\partial x_j} + \frac{\partial U_j}{\partial x_i} - \frac{2}{3}\frac{\partial U_k}{\partial x_k}\delta_{ij}\right) - \frac{2}{3}\rho k\delta_{ij}\right]\frac{\partial U_i}{\partial x_j}. && (3.25)\end{aligned}$$

In the SST model, turbulence production is limited in the turbulence kinetic energy transport equation to

$$\tilde{P}_k = \min\left(P_k, 10\beta^*\rho k\omega\right). \tag{3.26}$$

The turbulence kinetic energy transport equation is given as

$$\frac{\partial\rho k}{\partial t} + \frac{\partial}{\partial x_j}\left(u_j\rho k\right) = \tilde{P}_k - \beta^*\rho k\omega + \nabla \bullet \left[\left(\mu + \sigma_k\mu_t\right)\nabla k\right] \tag{3.27}$$

and the turbulence inverse time-scale transport is given as

$$\frac{\partial\rho\omega}{\partial t} + \frac{\partial}{\partial x_j}\left(u_j\rho\omega\right) = \frac{\gamma}{\hat{\nu}_t}P_k - \beta\rho\omega^2 + \nabla\bullet[(\mu + \sigma_\omega\mu_t)] + 2\left(1 - F_1\right)\rho\sigma_{\omega 2}\frac{1}{\omega}\nabla k\bullet\nabla\omega. \tag{3.28}$$

where eddy viscosity is limited to $\hat{\nu}_t = \max(\nu_t, 10^{-8})$ and F_1 is the first blending function which controls if κ–ϵ or κ–ω is used. The first blending function is given by

$$F_1 = \tanh\left\{\left\{\min\left[\max\left(\frac{\sqrt{k}}{\beta^*\omega d}, \frac{500\nu}{d^2\omega}\right), \frac{4\rho\sigma_{\omega 2}k}{CD_{k\omega}d^2}\right]\right\}^4\right\} \tag{3.29}$$

where the positive portion of the cross diffusion term is

$$CD_{k\omega} = \max\left(2\rho\sigma_{\omega_2}\frac{1}{\omega}\nabla k \bullet \nabla\omega, 10^{-10}\right). \tag{3.30}$$

Next, the constants in the equation need to be blended depending on the model. This is achieved through

$$\phi = \phi_1 F_1 + \phi_2 \left(1 - F_1\right) \tag{3.31}$$

where ϕ_1 denotes a constant of the κ–ω model and ϕ_2 the κ–ϵ model. These constants for the inner model are

$$\sigma_{k1} = 0.85 \left(0.5 \text{for baseline}\right), \qquad \sigma_{\omega 1} = 0.5, \tag{3.32}$$

$$\beta_1 = 0.075, \qquad \gamma_1 = \frac{\beta_1}{\beta^*} - \sigma_{\omega 1} \frac{\kappa^2}{\sqrt{\beta^*}} = 0.553 \tag{3.33}$$

and for the outer model are

$$\sigma_{k2} = 1.0, \qquad \sigma_{\omega 2} = 0.856, \tag{3.34}$$

$$\beta_2 = 0.0828, \qquad \gamma_2 = \frac{\beta_2}{\beta^*} - \sigma_{\omega 2} \frac{\kappa^2}{\sqrt{\beta^*}} = 0.440 \tag{3.35}$$

In both cases $\beta^* = 0.09$ and $\kappa = 0.41$. Lastly, in the case of a smooth wall with $y^+ < 3$

$$k = 0 \tag{3.36}$$

$$\omega = 800 \frac{\nu}{\left(\Delta y_1\right)^2} \tag{3.37}$$

where Δy_1 is the distance to the first centroid away from the wall [98].

3.2 Metacomp CFD++ Solver

General numerical methods iterate a system of equations in which continuous mathematical operators are replaced with discrete numerical equivalents. This process known as discretization results in a system of coupled algebraic equations in which dependent variables exist only at discrete points. Within computational fluid dynamics, the Navier–Stokes equations are commonly discretized using either finite difference (FDM), or finite volume methods (FVM). The finite difference method discretizes the differential form of the Navier–Stokes equations and replaces partial derivatives with algebraic differences based on a Taylor series expansion. While finite difference is relatively straightforward, it suffers from an inability to accurately handle problems where discontinuities exist (e.g., shocks). To resolve the issue with discontinuities, the integral form of the Navier–Stokes equations are discretized using the finite volume method. In this form, integrals are replaced with algebraic differences.

Discretizing the integral form of the Navier–Stokes equations allows FVM to handle discontinuities in the solution. In theory, using FVM mass, momentum, and energy are fully conserved. Compared to finite differencing, finite volume easily handles unstructured meshes. The finite volume method is therefore the preferred method for CFD, and widely used in both commercial and research CFD codes.

This section will discuss basics of the finite volume method and present its implementation within CFD++. For a more in-depth discussion on the finite volume method the reader is referred to any of the excellent CFD books published such as [99, 104, 105, 106]. A complete discussion of CFD++ can be found in its users manual [98].

3.2.1 Spatial Discretization

An example of a hexahedral finite volume mesh is shown in Fig. 3.1. Cell centers are shown by red dots, a selection of nodes around the central cell are illustrated with green dots, and shared faces are hatched. Each cell can be considered a control volume and is connected to other cells via shared faces. Unlike the finite difference method which stores dependent variables and flow properties at nodes on a grid, finite volume stores this information at the cell centers. Conservation is enforced within each control volume or cell by computing the fluxes through a cell face via surface

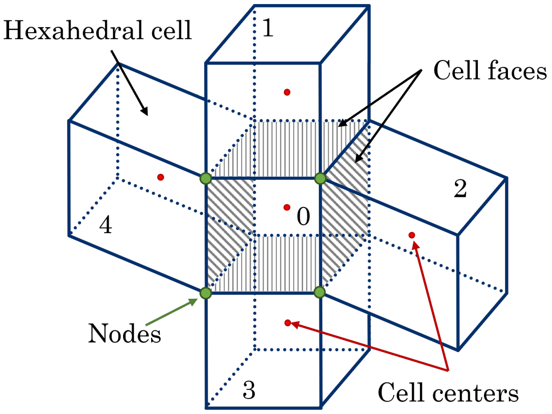

Figure 3.1: Example finite volume mesh

integration with information at the face interpolated from the cell center to that face. This means discretization occurs at both cell centers and cell faces.

Within CFD++, the governing Navier–Stokes equations are solved using FVM. As the Navier–Stokes equations include partial derivatives with respect to space and time, both temporal and spatial discretization is carried out. During spatial discretization, a piecewise multidimensional linear polynomial function is generated at each cell face which is a reconstruction of a scalar function within each cell. Since neighboring cells share a face, two values exist at each face: a polynomial to the left of the cell face, and a polynomial from the right of the face. In the example mesh of Fig. 3.1, if cell 0 is the active cell, and the fluxes on the right face is to be determined, there would be a polynomial from cell 0, and a polynomial from cell 2. The flux originating from the upwind direction is then used to determine the final face flux. If cell 0 is determined to be the upwind direction, its polynomial would be used to determine the final flux between cells 0 and 2. The upwind direction is required so that the solution is physically correct and the solution corresponding to the wave direction of travel at the cell face is chosen.

Each generated piecewise polynomial is used to determine cell gradients and in computing fluxes for the inviscid terms. CFD++ offers both a cell-centroidal and nodal-based polynomial. In this study, the nodal-based method was utilized as it ensures second order accuracy. The nodal-based method uses a least-squares average of the polynomials computed at cell nodes and a linear fit of cell-centered data from either face- or node-neighbors of the cell. The face-neighbor method was utilized in the current study to perform the linear fit of the cell-centered data.

The downside to piecewise polynomials is that they can yield a solution at a cell face which exceeds the solution at a cell center. To overcome this, Metacomp utilizes a multi-dimensional total variation diminishing (TVD) method. TVD prohibits the polynomial evaluated at a cell face from exceeding the neighboring cell center value, effectively limiting the slope of the polynomial. For compressible flows, the TVD method can result in erroneous solutions due to overly restricting the slope. To account for this, a compressibility correction is applied which allows for steeper slopes.

It is possible to discretize the viscous terms by using the non-limited cell polynomials from the inviscid discretization, but inaccuracies in the solution can occur. To get around this, the viscous terms are discretized with an out-of-face fit which removes the in-face contribution of the non-limited inviscid polynomials and combining it with an in-face fit. The out-of-face terms contain contributions from viscous flux derivatives from not only immediate face neighbors. This requires information from cells beyond the immediately neighboring ones. For example, in Fig. 3.1 if cell 3 was the active cell, then it could use information from all the cells pictured.

In cases where the upwind direction cannot be determined or multiple waves are propagating with different velocities, the final flux on the face is computed from a solution of the Reimann problem. To break the waves down into individual waves at each cell face, the solution to an assumed wave-interaction initial value problem is used. The resulting solution of the Reimann problem provides the net upwind flux for the transport equations. CFD++ utilizes a linearized approximate Riemann solver which obtains an exact solution to an approximate problem, specifically an averaged-state HLL-type (Harten, Lax, van Leer) Reimann solver as described in [107, 108, 109]. Some advantages of an HLL-type Riemann solver are that it preserves positivity, satisfies isentropy across expansion fans, and provides exact resolution of mesh-aligned shock waves. This means that all important properties of the exact solution are preserved in a non-iterative, closed-form flux solution which can be used with implicit numerical methods.

For each solution in this study, the compressible density-based solver of CFD++ was utilized. The Reimann solver in this scheme is able to detect the presence of strong shocks and expansions, but adds a small amount of dissipation for numerical stabilization. The scheme only applies this extra numerical dissipation in cells where strong pressure gradients are found. Areas of pressure gradients are determined by analyzing a cell and all cells sharing a face with that cell (face-neighboring) and then computing the pressure gradient across the collection of cells.

3.2.2 Temporal Discretization

As the Navier–Stokes equations have time dependencies, temporal discretization is required. Even with a steady-state CFD simulation, the converged solution can be thought of as a time-averaged solution. As the solution evolves through time, the time step used is a matter of importance. A large time step allows for the solution to quickly converge, but too large of a step will cause instabilities in the solution. This is especially true for explicit schemes where numerical stability is not assured. Implicit methods, like the ones used in CFD++, are theoretically stable for all time steps but non-linearities during the solution practically limit the time step. This is especially true at the start of a CFD simulation. After several time steps have been completed with the lower time step, it becomes possible to increase the value of the time step. For this reason the time step can be ramped within CFD++, and most CFD codes. This is accomplished by starting with a Courant (or CFL) number of one, and gradually increasing the CFL over a fixed number of iterations. Increasing CFL from 1–10 over 100–500 iterations is not uncommon for high speed flows.

Practically speaking, if the CFL number is too large, the error in the solution increases over time, and divergence will occur. CFD++ has an automatic Courant number adjustment, which detects if the time step for the iteration is too large. If the CFL number is determined to be too large, it will be reduced by half and the iteration retried. This decreases the likelihood that an instability will grow and affect the solution. Another method CFD++ makes use of to avoid instabilities is temporal smoothing. During temporal smoothing, CFD++ will use a part of the old solution (usually 25%) with the new solution to update the new solution. In order to avoid instabilities at the beginning of a simulation, CFD++ waits to introduce Reynolds stresses until the eleventh iteration and, additionally, the turbulence equations will be solved in their non-conservative form for the first 20 iterations.

3.2.3 Multigrid

Finite volume methods, while accurate, can take a long time to reach convergence. This is partially due to the extraordinary number of equations which are being solved. For the simple mesh of Fig. 3.1, there will exist a spatially discretized equation at each cell center, and one for each cell face. For the sake of simplicity, ignore the faces not shared by two or more cells and assume only one equation is to be solved instead of a set of coupled equations at each point. With these simplifications, there would still be five equations (one for each cell center), plus eight cell face equations (one for each direction possible at the four faces). So for a single cell, thirteen spatial equations will exist. Now if a grid of one million cells were to be generated the solver would have to solve 13 million equations.

Given the enormous number of equations to be solved, methods have been developed to reduce the number of equations and therefore decrease the computational time. One of the most popular methods is multigrid acceleration. Multigrid essentially assumes that a large number of unknowns will similarly affect multiple cells. So the correction to the solution during the iterative process will be similar for a group of neighboring cells. The solution in one cell is most likely going to be similar to the solution of a neighboring cell. So given the same initial conditions, a group a cells can use the same correction.

In CFD++, an algebraic multigrid is used to perform additive correction. This process is explained in detail by Guerrero [110]. As the solution evolves, the group of cells that could benefit from the same correction changes. New groups need to be formed throughout the solution. Also, within a mesh, there can be multiple levels of cell groupings from very coarse with a quarter of the total cells, down to groupings of only a few hundred thousand depending on the unknown. The multigrid cycle is the method used to obtain a correction. During a cycle, corrections are propagated between multigrid levels until all levels have been corrected. CFD++ utilizes a form of the full multigrid cycle, which traverses the levels from coarsest to medium, back to coarsest level, then to finest level and then returning to the coarsest, as illustrated in Fig. 3.2.

There are two cases where multigrid may be unable to group cells together. The first is in the instance where the algorithm determines there are no cells which fit the criteria to be grouped together, and the second is when cells should be grouped together but are being solved on different CPUs in a parallel job. In the latter case,

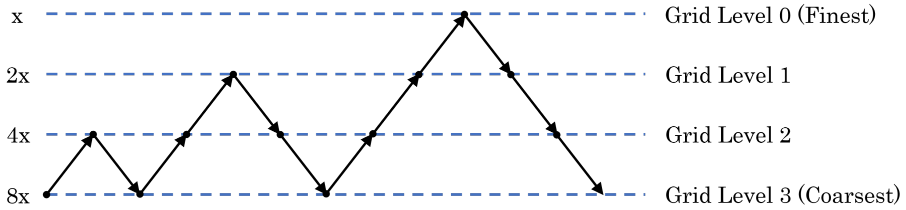

Figure 3.2: Full multigrid cycle level traverse

because cells exist on different CPUs, the algorithm is unaware of the connection between the cells since the process uses a sequential Gauss-Seidel relaxation.

3.2.4 CFD++ Implementation

The simulations were all performed using ICFD++ v19 by Metacomp. For all the runs (except inviscid runs), a steady RANS Menter SST κ–ω turbulence closure model was employed using a compressible density-based solver. Values of k and ω were set based on guidance from Georgiadis et al. [111] resulting in $k = 50.225$ m^2/s^2 and $\omega = 3.622 \times 10^5$ Hz. Making use of the CFD ramping capability, the CFL number was ramped from 1 to 500 over 300 iterations. This aggressive CFL, allowed for the residuals to drop by four orders of magnitude after only 400 iterations. Residuals were tracked and if they had remained flat for 1000 iterations, no further iterations were performed. A maximum of 5000 iterations was allowed, but never needed. The Reimann solver detected pressure gradients based on face neighbors, and TVD limiting also carried out based on face neighbors. Multigrid with a full multigrid cycle was employed over 4 cycles and a maximum allowable 20 multigrid levels. Cells were ordered by starting at the boundaries, followed by their immediate neighbors, and so on.

3.2.5 Hybrid RANS/LES Method

Large-Eddy simulation (LES) directly resolves large, energy containing eddies within an unsteady flow. Structures too small for LES to directly resolve in either space or time use a sub-grid scale model. While LES is great at solving unsteady flows, it becomes too expensive to use at large Reynolds numbers or flows with thin boundary layers. To reduce the cost of LES, CFD++ has several hybrid RANS/LES methods known as detached eddy simulation (DES) and limited numerical scales (LNS). These hybrid methods combine RANS and LES, using LES only in areas where it makes sense. Within smaller cells where turbulence scales can be directly resolved, LES is used. Within coarse cells and within attached turbulent boundary layers RANS is used. This combination relaxes mesh resolution and time step requirements.

Hybrid RANS/LES methods work well for highly separated flows. However, one weakness is that the traditional DES method uses mesh resolution to determine if RANS or LES is used. So if an attached boundary layer has any refinement, the method will switch to LES, when RANS is preferred. Later methods, such as LNS, DDES, and IDDES, were developed to overcome premature switching and use RANS rather than LES in areas where LES was not necessary. These methods use a filter width corresponding to some multiple of the maximum distance within a cell to determine if RANS or LES is used. Wavelengths larger than this filter are considered resolvable and LES is used. Smaller wavelengths are modeled using RANS (the cubic k-ϵ model in the case of LNS; the SA RANS model in the case of any of the DES-based models) [98].

The specific model used in this study is the Batten-Goldberg hybrid RANS/LES LNS model. In this model, transport equations are solved for the unresolved turbulence kinetic energy and its dissipation rate. Where the local mesh is too coarse for LES, LES is blended to a RANS-type model. The model also incorporates anisotropy and low Reynolds number damping effects in either LES or RANS modes [98]. In cells where RANS is used, the model reverts to a cubic κ–ϵ model. In regions of uniformly-refined mesh it blends automatically to an anisotropic form of the Smagorinsky model. The blending is performed in such a way that the effective shear-stress is continuous, given by the minimum of the two (RANS and LES) models [98]. The RANS/LES blending is achieved by damping the modeled stress tensor according to a given latency parameter.

3.3 Three-Dimensional Interactions

3.3.1 Geometry and Boundary Conditions

The shock generator in this study was a sharp fin with a leading-edge sweep of $\Lambda = 60\,\text{deg}$. The fin has a root chord of $c = 0.128$ m and span of $b = 0.0736$ m with a cross section of an isosceles triangle. The leading-edge half angle $\theta_{1/2} = 1.25\,\text{deg}$, and the trailing edge is blunt. Fin details are shown in Fig. 3.3. In the first study, the fin was placed above a flat plate within a rectangular computational domain along the centerline. The height of the computational domain is $h = 0.35$ m as seen in Fig. 3.4. The total plate width is $w = 0.75$ m and the plate length is $l = 0.658$ m which starts 0.22 m from the freestream inlet. Section 3.3.2 describes how the fin position was chosen.

Computational domain boundaries employed standard boundary conditions. An "Inflow/Outflow Characteristics Based" boundary condition was used for the inlet. This boundary condition prescribed the temperature and velocity at the inflow and pressure at the outflow. It required the user to specify static pressure, static temperature, and x, y, and z velocities. Both the plate and the fin boundaries were set as adiabatic viscous walls. As the wall y^+ was small enough, a solve-to-the-wall

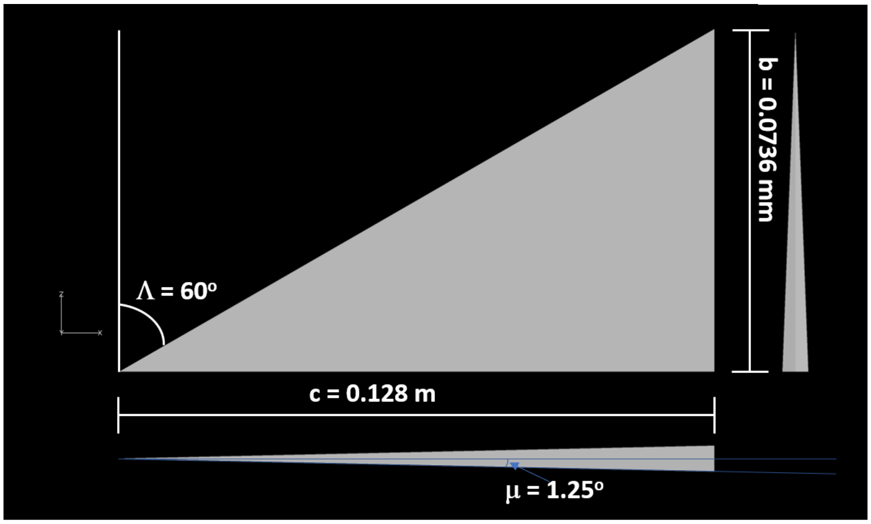

Figure 3.3: Schematic of swept fin

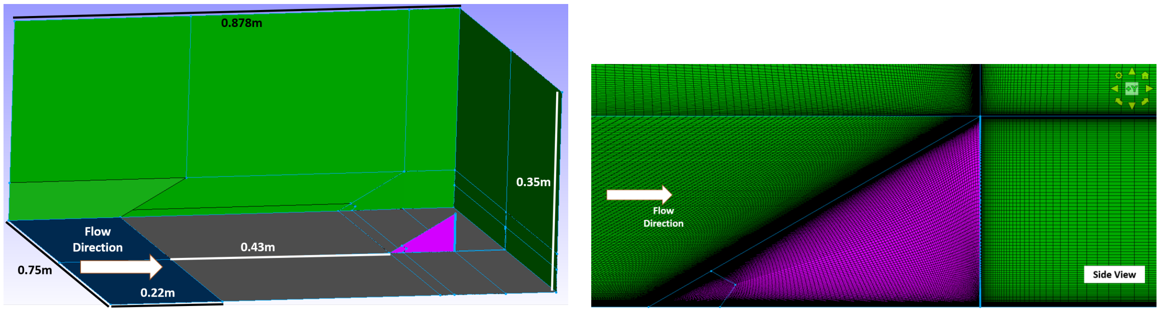

(a) Isometric view of fin mesh.

(b) Side view of fin mesh.

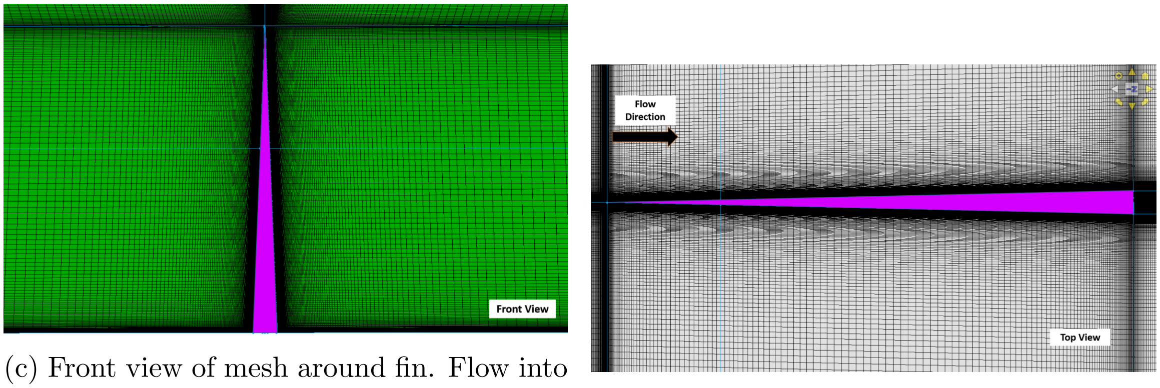

(c) Front view of mesh around fin. Flow into page.

(d) Top view of mesh around fin.

Figure 3.4: Meshing details.

scheme was used rather than wall functions. A wall boundary condition set turbulence related quantities equal to their wall-limiting values [98]. To mitigate reflected shocks

Table 3.1: Flat plate geometric properties

Domain	
Plate length l	0.658 m
Plate width w	0.75 m
Fin leading-edge location x_f	0.43 m (from plate LE), 0.65 m (from inlet face)
Computation domain height h	0.35 m
Mesh settings	
Wall y^+	< 1
Initial cell height	0.004 mm
Cells in boundary layer	60
Growth Rate	1.08
Cell Count	
No gap	$\approx$ 57 million
g/δ_{BL}=0.221	$\approx$ 82 million
g/δ_{BL}=0.443	$\approx$ 108 million
Cells in gap normal to plate	100
Fin	
Leading-edge sweep Λ	60 deg
Fin half angle $\theta_{1/2}$	1.25 deg
Span b	0.0736 m
Root chord c	0.128 m
Gap g	0.0, 1.27 and 2.66 mm
Gap g/δ_{BL}	0.0, 0.221 and 0.443

from the plate on the top computational boundary the top boundary condition was set to a “Supersonic Outflow” and Metacomp’s “Absorbing Layers” were enabled. A supersonic outflow extrapolated all quantities from the interior cells and prevented flow from returning to the computational domain. This boundary condition set flow velocities to zero if the flow attempts to reverse. No quantities were prescribed for the supersonic outflow boundary condition. Geometry and mesh setup details are given in Table 3.1.

In addition to placing the fin above the flat plate, it was also placed above a body of revolution. As with the previous setup, the inlets of the computation domain were set to an “Inflow/Outflow Characteristics Based” boundary condition. The fin and body of revolution were set to adiabatic viscous walls. With a maximum diameter of $d_{mesh} = 0.725$ m and length of $l_{mesh} = 1$ m, the computational domain itself is approximately half a cone as seen in Fig. 3.5. The body of revolution was cut in half to take advantage of symmetry, and a single fin was placed above the centerline and deflected 12 deg. As seen in Fig. 3.6 the diameter of the body of revolution is $d = 0.128$ m with the fin placed in the vicinity of the centerline of the computational domain at $x_f = 0.779$ m from the nose tip. A von Kármán ogive with a length to diameter ratio of 3:1 forms the nose of the BoR. The total length of the ogive-body of revolution combination is $l = 0.966$ m and starts 0.044 m from the freestream inlet. Mesh setup details are given in Table 3.2. The fin was placed with a gap between it and the cylinder of 1.31 mm at the fin point of rotation. The fin was deflected 12 deg about a point two-thirds downstream from the fin leading edge, leading to a gap between the fin leading edge tip and body of 3.64 mm.

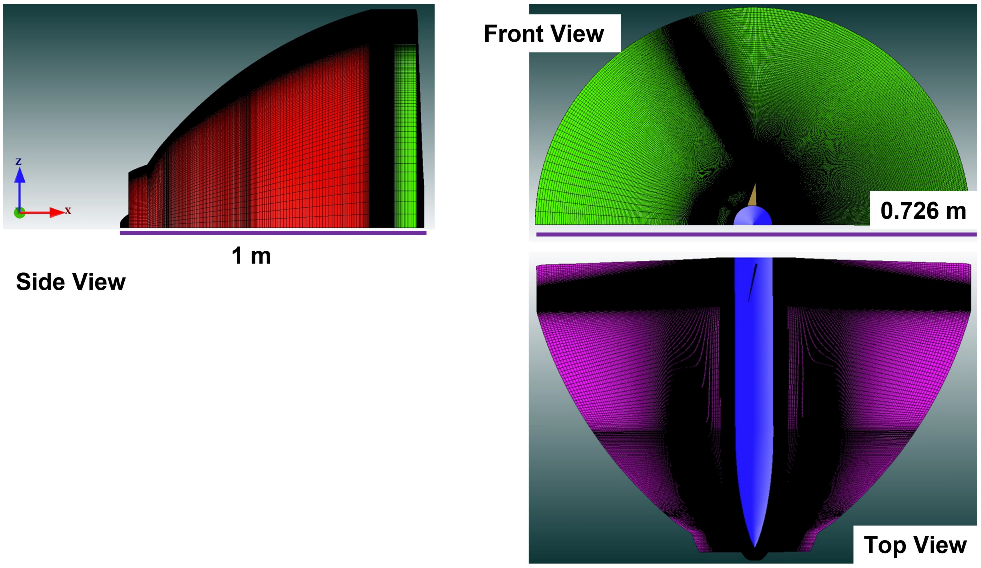

Figure 3.5: Three-view of fin on body of revolution mesh, $\delta = 12\,\text{deg}$

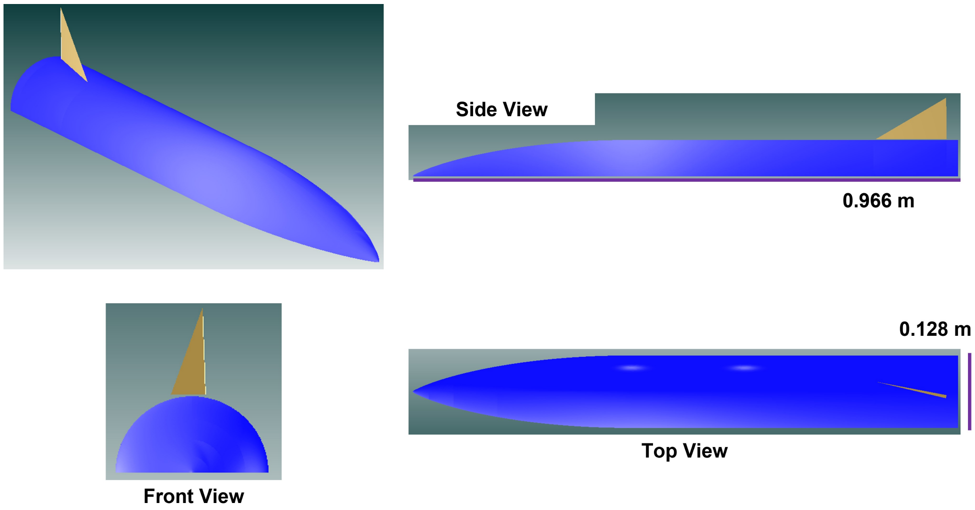

Figure 3.6: Three-view of fin on body of revolution, $\delta = 12\,\mathrm{deg}$

The mesh off the wall boundaries used a growth rate from the walls of 1.08 and the boundary layer contained at least 60 cells normal to the surface. Grid refinement was applied at the nose and fin leading-edges for shock wave resolution. Illustrative details of the mesh around the fin are given in Fig. 3.7.

For this study, Mach 2.5 and a unit Reynolds number of 55×10^6/m were utilized. Experimental data at this condition were available for a fin on a flat plate by Lu [17]. Freestream flow conditions are given in Table 3.3. For all geometries, the entire computational domain was initialized to free stream conditions.

3.3.2 Boundary Layer

Prior to meshing the fin on a flat plate, the size and length of the plate were determined by running CFD on a bare flat plate. The boundary layer profile was checked at several downstream locations along the plate to ensure a fully-developed turbulent boundary layer was formed. The profile was compared to the theoretical turbulent boundary layer by transforming the numerical results using the Van Driest

Table 3.2: Body of Revolution Geometric Properties

Domain	
Body of revolution length l	0.966 m
Nose length l_n	0.384 m
Cylinder diameter d	0.128 m
Nose fineness ratio l_n/d	3.0:1 tangent ogive
Fin leading-edge location x_f	0.779 m (from nose tip) 0.823 m (from inlet face)
Computation domain diameter d_{mesh}	0.726 m
Mesh settings	
Wall y^+	< 1
Initial cell height	0.004 mm
Cells in boundary layer	60
Growth Rate	1.08
Cell Count	$\approx$ 156 million
Fin on Body of Revolution	
Gap g at rotation point	1.31 mm
Gap g/δ_{BL}	0.131
Gap g at quarter chord	2.13 mm
Gap g/δ_{BL}	0.221
Gap g at fin tip	3.64 mm
Gap g/δ_{BL}	0.377

II transformation [112, 113]. The inner region of the transformed boundary layer profile was compared to Reichardt [114], and the wall wake compared to the wallwake law of Granville [102, 115, 116].

The Van Driest II [112] transformation is given by

$$U^+ = \frac{U_e}{U_\tau A_1} \sin^{-1}\left(\frac{2A_1^2\,(U/U_e) - B_1}{\sqrt{B_1^2 + 4A_1^2}}\right) \tag{3.38}$$

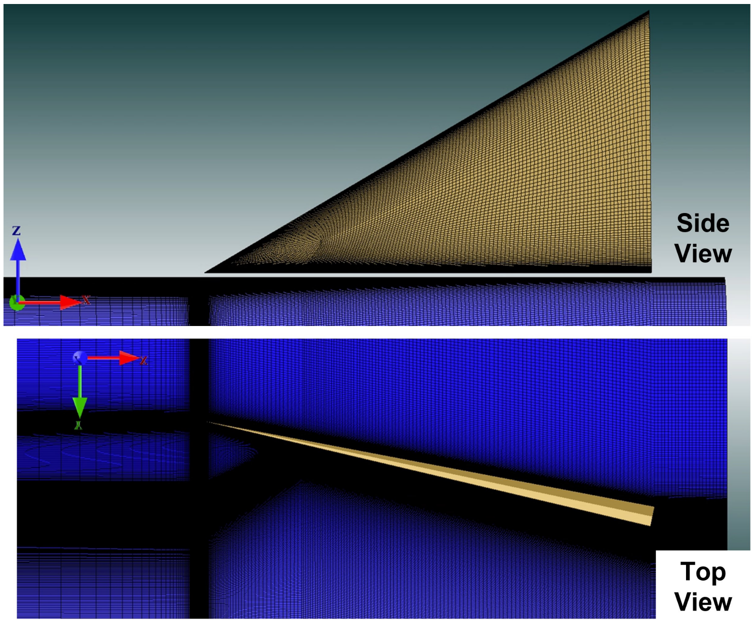

Figure 3.7: Three-view of fin on body of revolution fin mesh close-up, $\delta = 12\,\text{deg}$

Table 3.3: Incoming freestream flow conditions

Mach number M_∞	2.5
Freestream velocity U_∞	578.64 m/s
Static pressure P_∞	25413 Pa
Static temperature T_∞	133.33 K
Density ρ_∞	0.6637 kg/m^3
Unit Reynolds number Re_u	55×10^6/m

where

$$A_1 = \sqrt{\frac{(\gamma - 1)\, r M_e^2}{2} \frac{T_e}{T_w}} \tag{3.39a}$$

$$B_1 = \left[1 + \frac{(\gamma - 1)\, r M_e^2}{2}\right] \frac{T_e}{T_w} - 1 \tag{3.39b}$$

$$U_\tau = \sqrt{\frac{\tau_w}{\rho_w}} \tag{3.39c}$$

$$U^+ = \frac{U}{U_\tau} \tag{3.39d}$$

Starting with the region closest to the wall, the viscous sublayer is

$$u^+ = y^+. \tag{3.40}$$

The inner region $5 \leq y^+ \leq 30$ given by [114] is

$$u^+ = C_1 \left[1 - \exp\left(-\frac{y^+}{11} \right) - \frac{y^+}{11} \exp\left(-0.33 y^+ \right) \right] + \frac{1}{\kappa} \ln\left(1 + \kappa y^+ \right) \tag{3.41}$$

where the von Kármán constant $\kappa = 0.41$ and the constant

$$C_1 = C - \frac{\ln \kappa}{\kappa} \tag{3.42}$$

using a value of $C = 4.9$. Granville's law of the wake [115] is

$$u^+ = \frac{1}{\kappa} \ln y^+ + C + \frac{1}{\kappa} \left[\Pi \left(1 - \cos \pi\eta \right) + \left(\eta^2 + \eta^3 \right) \right] \tag{3.43}$$

where the von Kármán constant $\kappa = 0.41$, the law-of-the-wall constant $C = 4.9$, and the wake parameter $\Pi = 0.55$. The nondimensional boundary layer thickness

$$\eta = \frac{y}{\delta} \tag{3.44}$$

where the criterion for the boundary layer thickness was chosen to be $U/U_e = 0.995$.

Transformed results plotted in wall coordinates at a downstream location just upstream of the final fin location are shown in Fig. 3.8 as a solid blue line. The dashed purple line shows Granville's wallwake law, the circles are Reichardt's inner region, and the viscous sublayer is given by diamonds. The figure shows that the boundary layer is fully developed at the fin location with the expected wallwake characteristics.

Using the same method outlined above for the flat plate, boundary layer analysis was performed along the top centerline of the body of revolution. Due to the curvature of the body, the velocity is no longer all aligned in the x-axis. In place of U in

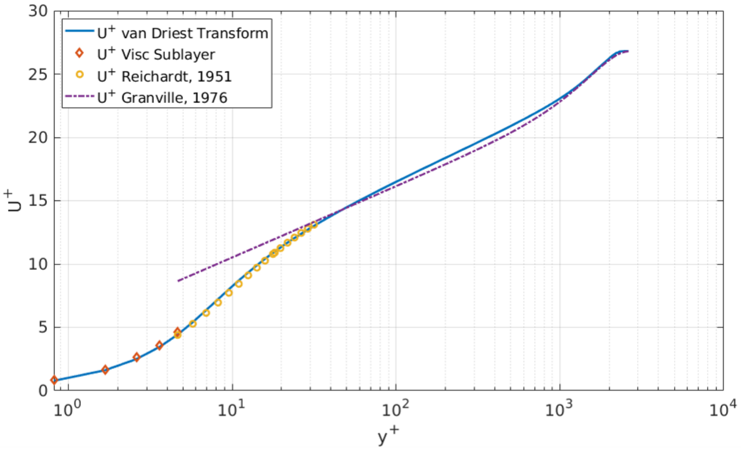

Figure 3.8: Undisturbed velocity profile in transformed wall coordinates. Solid line: Van Driest II transformation of present data; dashed line: wallwake law [115] ($\Pi = 0.55, C = 4.9, \kappa = 0.41$); circles: inner region [114] ; diamonds: viscous sublayer

Eqs. 3.38 and 3.39d, the velocity magnitude $\sqrt{U^2 + V^2 + W^2}$ is used. Similarly, the magnitude of the wall shear stress $\sqrt{\tau_x^2 + \tau_y^s + \tau_z^2}$ is used in place of τ_w. In this case, the constants, C, and κ were slightly adjusted to $C = 5$ and $\kappa = 0.392$. The resulting transformed boundary layer profile is plotted in Fig. 3.9, and shows good agreement with theoretical predictions.

3.3.3 Viscous Interaction

To further establish that the fin was placed far enough downstream so that the plate leading-edge shock interaction has no effect on the STBLI, the viscous interaction similarity parameter $\bar{\chi}$ was computed. For turbulent flows, $\bar{\chi}$ depends on whether the interaction is strong or weak. From Stollery and Bates [117] $\bar{\chi}$ for the strong and weak interactions are given respectively by

$$\bar{\chi} = \left(\frac{CM_\infty^9}{Re_x}\right)^{\frac{2}{7}} \tag{3.45}$$

$$= \left(\frac{CM_\infty^9}{Re_x}\right)^{\frac{1}{5}} \tag{3.46}$$

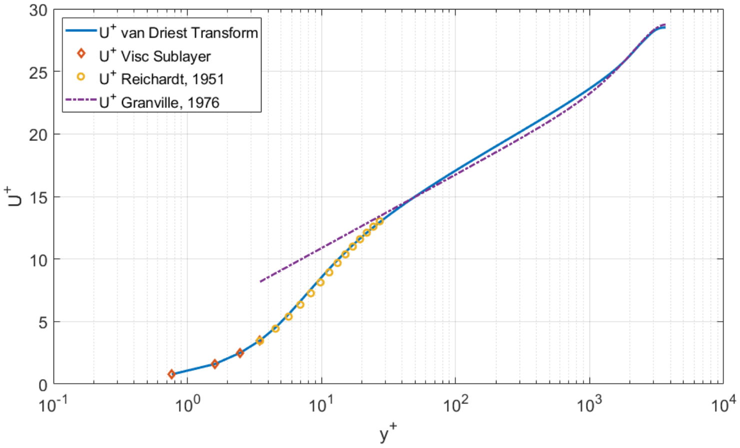

Figure 3.9: Undisturbed velocity profile on body of revolution centerline in transformed wall coordinates. Solid line: Van Driest II transformation of present data; dashed line: wallwake law [115] ($\Pi = 0.55, C = 5, \kappa = 0.392$); circles: inner region [114] ; diamonds: viscous sublayer

The pressure ratio p_w/p_∞ is used to determine if the interaction at a particular location is strong or weak [117]. If the ratio is close to unity and is approximately uniform, then the interaction is considered weak. However, if the pressure ratio is on the order of $\bar{\chi}$ then the interaction is strong. Pressure ratio and the $\bar{\chi}$ value at the fin leading-edge X_{L_f} for this case are plotted in Fig. 3.10. As can be seen, the pressure ratio is close to unity with $p_w/p_\infty \approx 1.01$ just before the fin leading-edge and is approximately uniform leading up to it. Therefore the viscous interaction just upstream of the fin is weak.

3.3.4 Flat Plate with a Fin: Zero Deflection

After characterization of the plate boundary layer, the swept fin was placed at a location ensuring it was in the fully-developed, turbulent boundary layer. This put the fin leading-edge at $x_f = 0.43$ m. Simulations of an undeflected fin ($\delta = 0\,\text{deg}$) without flow incidence were performed to check setup and initial conditions. As the

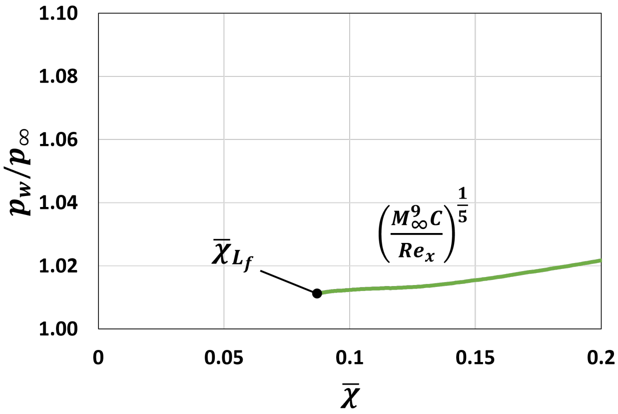

Figure 3.10: Pressure variation vs viscous interaction similarity parameter $\bar{\chi}$. Solid line: turbulent pressure ratio, weak interaction [117]; Point: viscous interaction parameter at fin leading-edge location.

fin half angle $\theta_{1/2} = 1.25\,\text{deg}$, when the fin is undeflected, the flow was still deflected by $\theta_{1/2}$ and therefore at $\delta = 0\,\text{deg}$, $\alpha = \theta_{1/2} = 1.25\,\text{deg}$. From Korkegi, separation occurs starting when $M_\infty \alpha = 0.3$ where α is in radians. At Mach 2.5, and a fin half angle of 1.25 deg, this product is 0.055, well below the Korkegi criterion. As expected, no separation is observed, as seen by the surface streakline patterns shown in Fig. 3.11. The streaklines in the figure are color coded by pressure coefficient C_p. The figure shows that the streaklines remained parallel to the fin surface, except at the blunt base. Surface streaklines (similar to limiting streamlines) are restricted to the plane of the boundary surface. They were computed by FieldView using shear velocity (velocity gradient at the surface) [118].

3.4 Grid Generation and Grid Independence Study

For more control over the cells in the boundary layer, grid density and cell-to-cell volume ratios, a fully structured mesh was generated for this study. A grid convergence study was performed to ensure proper resolution of the plate leading-edge shock, boundary layer, and fin shock. Three structured meshes for both the no

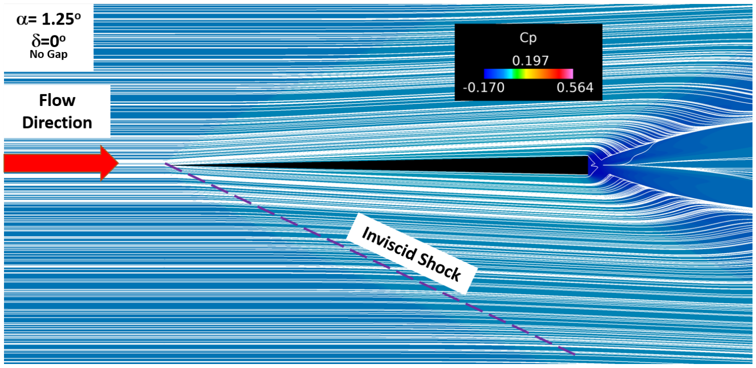

Figure 3.11: Surface streaklines on plate. Fin is aligned at zero incidence to the incoming flow, $\delta = 0\,\text{deg}$. leading-edge sweep $\Lambda = 60\,\text{deg}$. Plate colored by C_p, with maximum value dictated by maximum value for all cases studied.

gap case and for the gap of $g/\delta_{BL} = 0.443$ were generated using Pointwise 18.4R4. For the no gap case, the first mesh contained approximately 57 million cells. Each subsequent mesh increased the cell count, resulting in meshes of 98 and 183 million cells. To achieve $y^+ < 1$ at the wall, each mesh had an initial cell spacing of 0.004 mm off the plate and fin boundaries. The mesh within the boundary layer contained at least 60 cells normal to the surface for meshes one and two. In the case of mesh three, 120 cells normal to the surface was used. Grid resolution was applied at the plate leading edge and fin leading edge for shock wave resolution. As the fin was submerged in the viscous portion of the freestream additional refinement at the fin leading edge was also needed for proper setup of the STBLI. Growth rate and average cell size were varied between the meshes. The parameters of interest for the grid convergence study were the axial and normal forces generated by the fin. The fin forces for each mesh can be found in Table 3.4. Compared to mesh one, meshes two and three were within less than 1% in axial force and less than 0.2% in normal force. The normalized surface pressure on the plate, from the plate leading edge to just upstream of the fin was also captured for each mesh, and is presented in Fig. 3.12. It shows almost identical values for meshes one and three and slightly different values for mesh two at

Table 3.4: Grid Convergence Study Results

Mesh	Cell Count (million)	Fin Axial Force (N)	Fin Normal Force (N)
1	57	8.013	249.77
2	98	7.962	250.13
3	183	8.059	251.32

the plate leading edge up to about a third of the plate length. After X/L=0.4 surface pressures for each mesh are nearly identical. Since all the meshes showed excellent agreement, mesh 1 was chosen as it had the fewest cells (resulting in less run time).

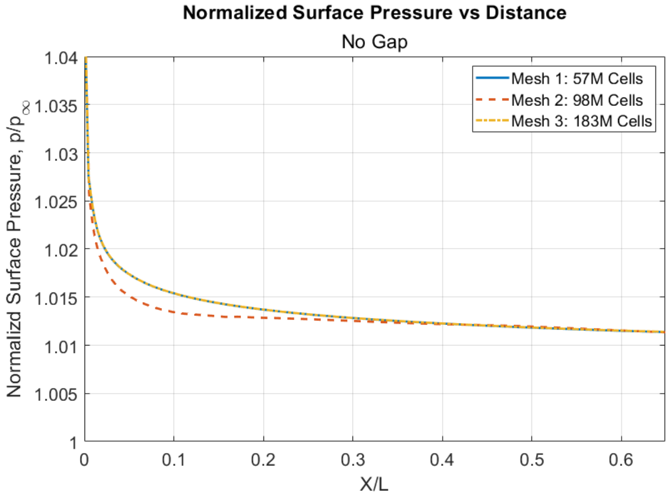

Figure 3.12: Normalized surface pressure for coarse, medium, and fine mesh versus distance along plate.

A grid convergence study was also performed for the geometry with the largest gap, g/δ_{BL}=0.443. The resulting meshes in this study had 108, 247, and 341 million cells. As before, fin forces were computed from each mesh compared. The resulting forces are shown in Table 3.5. Compared to the coarsest mesh, meshes two and three fin axial force was within less than 1% and fin normal force was within less than 0.1%. Additionally, for the case with the gap, surface flow on the plate was used to evaluate

Table 3.5: Grid Convergence Study Results: g/δ_{BL}=0.443

Mesh	Cell Count (million)	Fin Axial Force (N)	Fin Normal Force (N)
1	108	8.12	244.45
2	247	8.17	244.61
3	341	8.20	244.47

the accuracy of each mesh. A top down view of the plate colored by normalized surface pressure and surface streaklines added for each mesh is shown in Fig. 3.13. Lines of inviscid shock, primary separation, and upstream influence have been added. For each mesh resolution, the angles of inviscid shock, primary separation, and upstream influence were identical. Together with the fin force results and topological features, mesh one can be considered accurate and was chosen for this research.

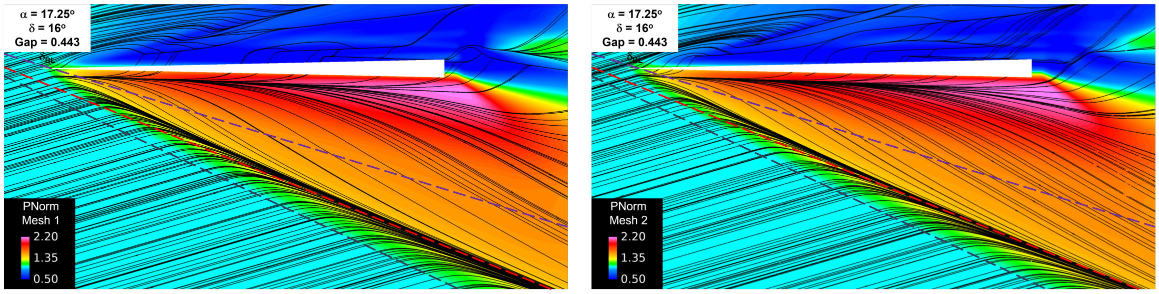

(a) Mesh 1

(b) Mesh 2

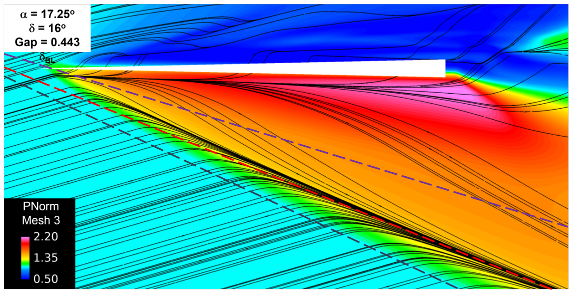

(c) Mesh 3

Figure 3.13: Streaklines on plate showing moderate interaction. Plate colored by normalized surface pressure. Gap $= 0.443\delta_{BL}$; $\delta = 16\,\text{deg}$

CHAPTER 4

RESULTS

With the numerical method established and computational domain presented, we come now to the results of the current study. We start in Sec. 4.1 which compares the separation region for the swept fin at several deflection angles to results by Lu [19] for an unswept fin. The determination of incipient separation angle is presented in Sec. 4.2. Then Sec. 4.3 compares the surface pressure results to those from theory. Flow features unique to the leeside of the fin are discussed in Sec. 4.4. Section 4.5 presents comparisons of fin effectiveness from this study with wind tunnel results. Following this, in Sec. 4.6, results from a hybrid RANS/LES simulation are compared to the RANS results for a fin deflected 16 deg. The chapter closes with Sec. 4.7, where the results for a fin on a body of revolution are presented.

4.1 Upstream Influence

Upstream influence is a striking feature of shock/boundary layer interaction. Contrary to purely inviscid flows, the free-stream or upstream flow "feels" the shock and is influenced by it prior to encountering the shock wave. This is seen in the turning of the streaklines prior to reaching the separation line in Fig. 4.1.

Dimensional analysis and hypersonic similarity were utilized by Lu et al. [19] in developing semi-empirical expressions relating (i) the upstream influence angle β_u (ii) the inviscid shock angle β_0 and (iii) the difference between these angles and the free-stream Mach angle μ_∞. Additionally, semi-empirical relationships were devel-

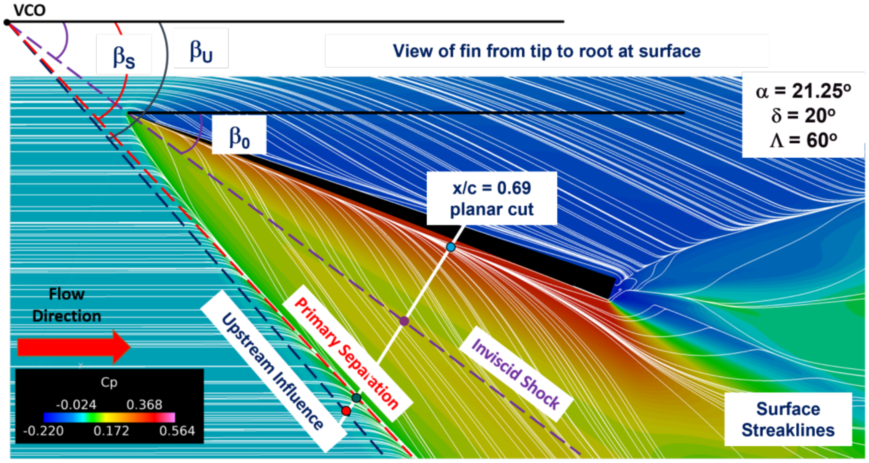

Figure 4.1: Illustration of virtual conical origin showing upstream influence (blue), primary separation (red), and inviscid shock trace (purple). Mach 2.5, $\delta = 20\,\text{deg}$, $\Lambda = 60\,\text{deg}$. Plate colored by C_p.

oped between the various β angles and α. This section compares the results for the upstream influence angle of this study to those obtained by Lu.

4.1.1 Effect of Deflection on Separation

The first semi-empirical relationship uses the reduced inviscid shock angle $\Delta\beta_0$ to determine the reduced upstream influence angle $\Delta\beta_U$. As shown in Fig. 4.2 Lu et al. compared the resulting $\Delta\beta$ angles for fins at three different Mach numbers. At $M_\infty = 2.95$, two different leading edge sweep angles (20 and 40 deg) were also compared to the no sweep case. Added to the plot are results from the current study for the no gap case (circles), gap of $0.221\delta_{BL}$ (squares), and gap of $0.443\delta_{BL}$ (diamonds). All configurations for the current study were at $M_\infty = 2.5$ with $\Lambda = 60\,\text{deg}$. The semi-empirical equation derived is

$$\Delta\beta_U = 2.2\Delta\beta_0 - 0.027\Delta\beta_0^2 \tag{4.1}$$

where the reduced upstream influence angle is $\Delta\beta_U = \beta_U - \mu_\infty$ and the reduced inviscid shock angle is $\Delta\beta_0 = \beta_0 - \mu_\infty$. It is observed in Fig. 4.2 that the gap height had no affect on the inviscid shock angle no matter the deflection angle. Also seen is that the upstream influence line is only slightly influenced by the gap, as all gap heights closely follow the relationship and are almost identical at higher angles.

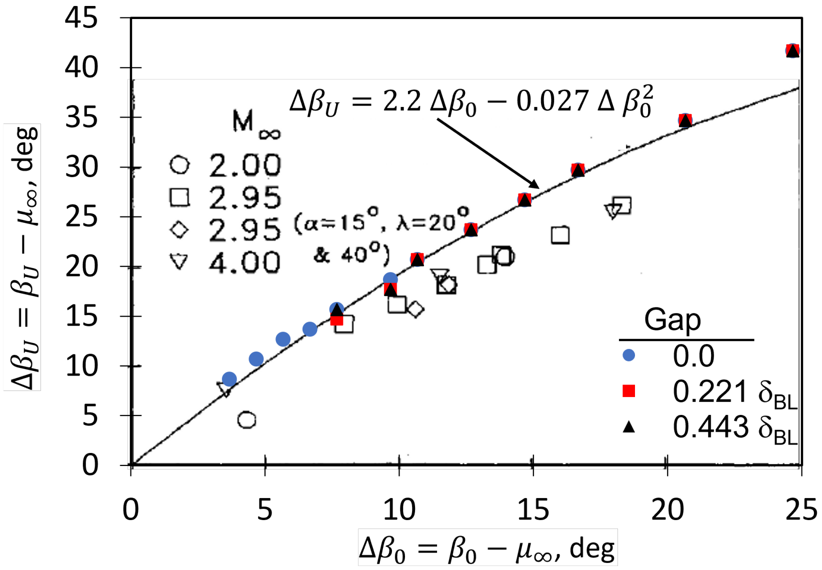

Figure 4.2: $\Delta\beta_U$ vs $\Delta\beta_0$ at different Mach and fin sweep angles. Original figure from Lu et al. [19]. Current results: $M_\infty = 2.5$, $\Lambda = 60$ deg, circle (no gap), square (gap $= 0.221\ \delta_{BL}$), and triangle (gap $= 0.443\ \delta_{BL}$).

We now turn our attention to how α impacts both the reduced upstream influence angle and the reduced inviscid shock angle. The dependence of $\Delta\beta_0$ on α is plotted in Fig. 4.3 and shows a decrease in $\Delta\beta_0$ for the swept fin compared to the unswept fin for a given α. This is because a swept fin reduces the strength of the inviscid shock consequently reducing the inviscid shock angle. The resulting relationship between $\Delta\beta_0$ and α for a swept fin is given by

$$\Delta\beta_0 = 0.4465\alpha + 0.0112\alpha^2 \tag{4.2}$$

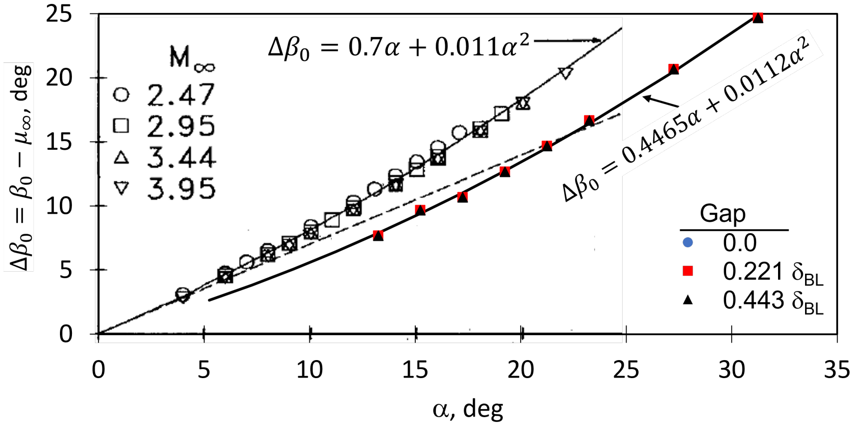

Figure 4.3: Reduced inviscid shock angle $\Delta\beta_0$ vs α. Original figure from Lu et al. [19]. Current results: $M_\infty = 2.5$, $\Lambda = 60$ deg, circle (no gap), square (gap = 0.221 δ_{BL}), and triangle (gap = 0.443 δ_{BL}).

The reduced upstream influence angle $\Delta\beta_U$ is plotted versus α with the current results added is shown in Fig. 4.4. This plot demonstrates that the resulting SBLI is weakened due to the weakening of the inviscid shock leading to a decrease in the upstream influence angle. While $\Delta\beta_U$ is linearly dependent on α for an unswept fin, the swept fin shows a quadratic dependence over the range of α studied. A simple curve fit was applied resulting in the empirical equation for a swept fin

$$\Delta\beta_U = 1.0547\alpha + 0.0088\alpha^2 \tag{4.3}$$

Both $\Delta\beta_0$ and $\Delta\beta_U$ have a weak dependence on the change in gap height, and so the same empirical relationships is valid for both with and without the gap geometries.

The upstream influence angle β_U vs the inviscid shock angle β_0 for several Mach numbers is plotted in Fig. 4.5. The results by Lu [19] are for unswept fins, and the current results are for a swept fin with three difference gap heights. It can be seen from these results that the sweep angle and gap height had almost no affect on the

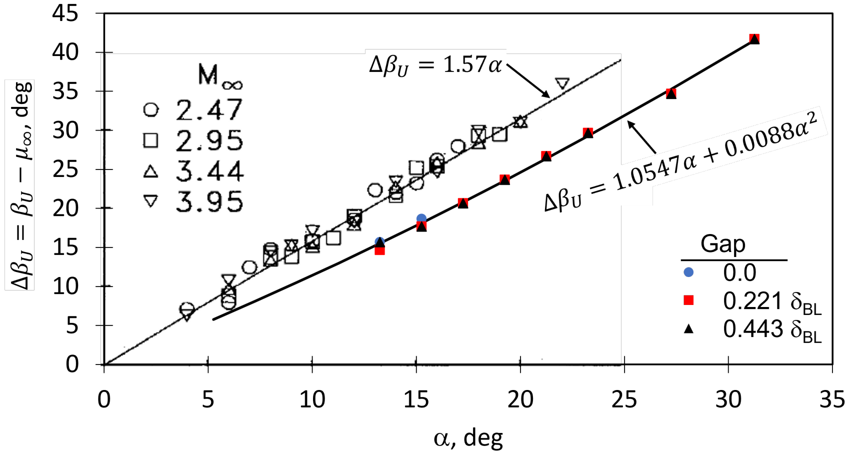

Figure 4.4: Reduced upstream influence angle $\Delta\beta_U$ vs α. Original figure from Lu et al. [19]. Current results: $M_\infty = 2.5$, $\Lambda = 60$ deg, circle (no gap), square (gap = 0.221 δ_{BL}), and triangle (gap = 0.443 δ_{BL}).

ratio between β_0 and β_U. Mach number is the principal driver to the ratio of the angles.

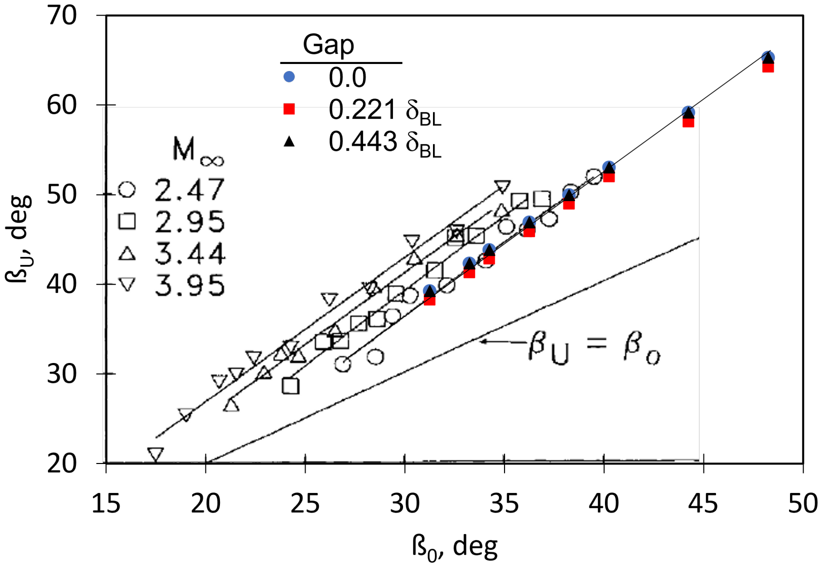

Figure 4.5: Upstream influence angle β_U vs inviscid shock angle β_0. Original figure from Lu et al. [19]. Current results: $M_\infty = 2.5$, $\Lambda = 60$ deg, circle (no gap), square (gap = 0.221 δ_{BL}), and triangle (gap = 0.443 δ_{BL}).

Settles and Kimmel [119] developed empirical relationships for quasiconical flow for a swept compression ramp shock generator and a swept fin. For the swept fin, the upstream influence angle is obtained if the inviscid shock angle was known using

$$\beta_U = 1.59\beta_0 - 10.0 \tag{4.4}$$

From inviscid shock angles computed in this study, the upstream influence angle is calculated with Eq. 4.4. A comparison of the computed β_U values (line), and measured values from CFD (points) versus normal Mach number is plotted in Fig. 4.6. For the range of α analyzed, the results between the empirical equation and the current CFD results agree with one another at lower normal Mach numbers, and slightly deviate at normal Mach numbers. The gap effects are most significant around the incipient separation location, and almost negligible at higher values of normal Mach number.

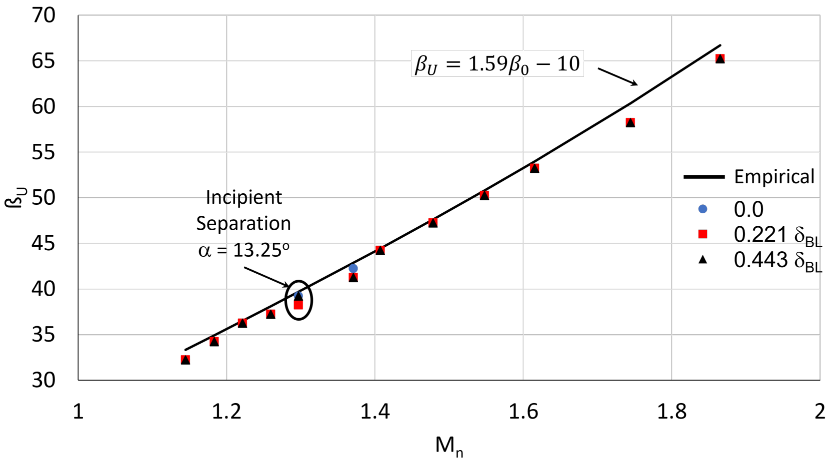

Figure 4.6: β_U vs M_n. Eq. 4.4 (line), Current study: circles (no gap), square (gap = 0.221 δ_{BL}), and triangle (gap = 0.443 δ_{BL}). $M_\infty = 2.5$, $\lambda = 60$ deg.

Empirical equations for the conical angles of upstream influence β_U, primary separation β_S, and primary attachment β_R, were developed by Zheltovodov for both unswept and swept fin interactions [3, 76]. They are given as

$$\begin{aligned} \beta_U - \beta_{Ui} &= 1.53\left(\beta_0 - \beta_{0i}\right) && (4.5) \\ \beta_S - \beta_{Si} &= 2.15\left(\beta_0 - \beta_{0i}\right) - 0.0144\left(\beta_0 - \beta_{0i}\right)^2 && (4.6) \\ \beta_R - \beta_{Ri} &= 1.41\left(\beta_0 - \beta_{0i}\right) - 0.0139\left(\beta_0 - \beta_{0i}\right)^2 && (4.7) \end{aligned}$$

Plots comparing the current results of conical angles to the empirical relations are given in Fig. 4.7 and Fig. 4.8. In both plots, the lines are the empirical results, and points are from the current study. In Fig. 4.7, the circles represent the no gap case, squares are for a gap of $0.221\delta_{BL}$, and triangles are for a gap of $0.443\delta_{BL}$. In Fig. 4.7a the primary separation line angle for a given deflection angle minus the primary separation line angle at incipient separation is plotted versus the inviscid shock angle at the same deflection angle minus the incipient inviscid shock angle. Results show that for each of the gap heights, the overall trend is followed. The results are in better agreement at lower angles, compared to higher angles. However, at higher angles the larger gap is closer to the empirical values. Figure 4.7b plots the upstream influence angle for a given deflection angle minus the incipient upstream influence angle versus the inviscid shock angle at the same deflection angle minus the incipient inviscid shock angle. For each of the gap heights, results between CFD and the empirical relation show good agreement. However, the gap height of $0.221\delta_{BL}$ consistently has a greater value of $\beta_U - \beta_{Ui}$ compared to the other gap heights.

Results for $\beta_U, \beta_S, \beta_R$ vs β_0 for each of the gap heights are plotted in Fig. 4.8 and compare numerical results obtained to empirical results. For each of the gap heights, the results are in good agreement with the empirical values over the range of inviscid shock angle ran in CFD. The results from CFD also confirm the conver-

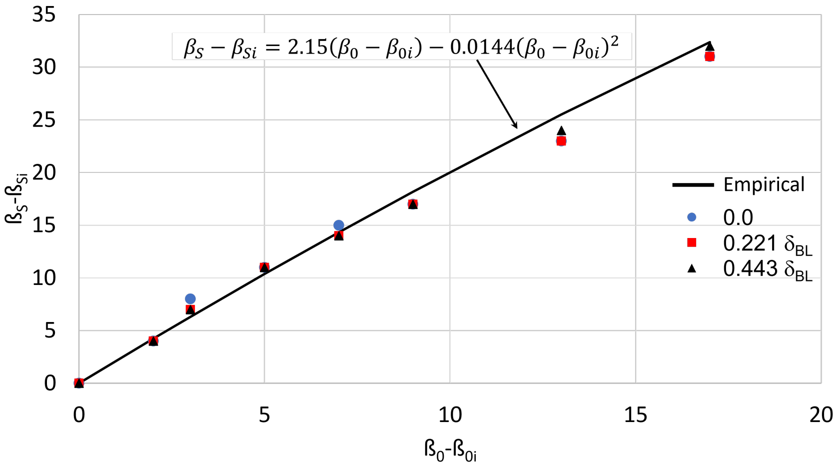

(a) $\beta_S - \beta_{Si}$ vs $\beta_0 - \beta_{0i}$.

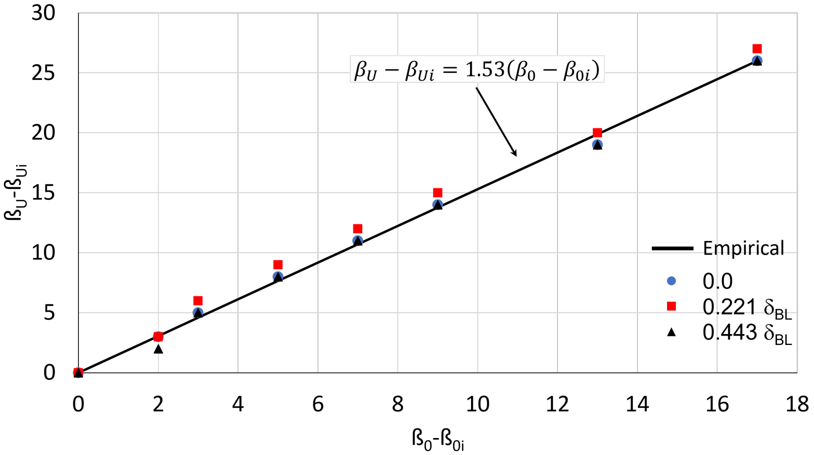

(b) $\beta_U - \beta_{Ui}$ vs $\beta_0 - \beta_{0i}$.

Figure 4.7: Comparisons to empirical relations from Zheltovodov [3, 76]. Line: empirical equations; Current study: circles (no gap), square (gap = 0.221 δ_{BL}), and triangle (gap = 0.443 δ_{BL}).

gence of the upstream influence angle with the primary separation line as predicted with the empirical relations. The gap angle, however, affects the location where the convergence of the two lines occurs. The gap height of $0.221\delta_{BL}$ shows convergence soonest, where the gap of $0.443\delta_{BL}$ is the most delayed.

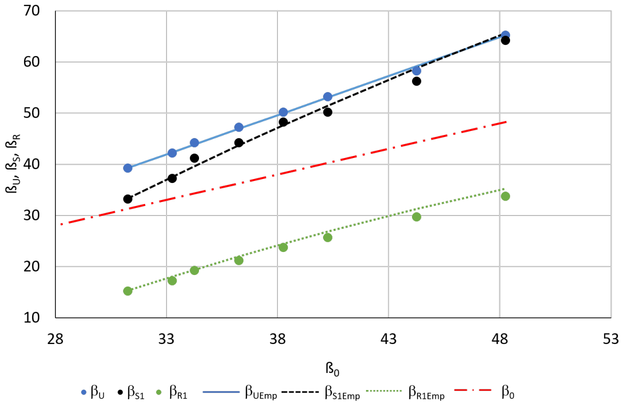

(a) No Gap.

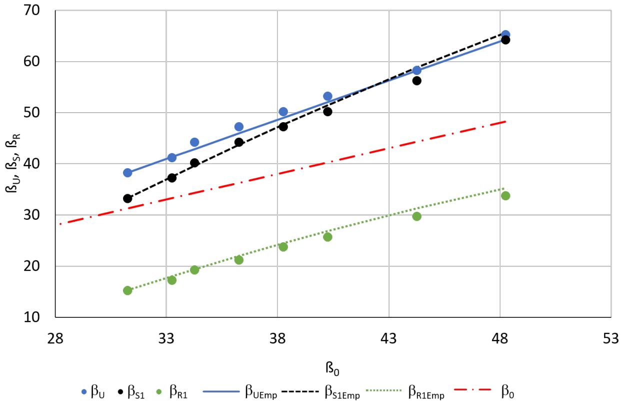

(b) Gap = $0.221\delta_{BL}$.

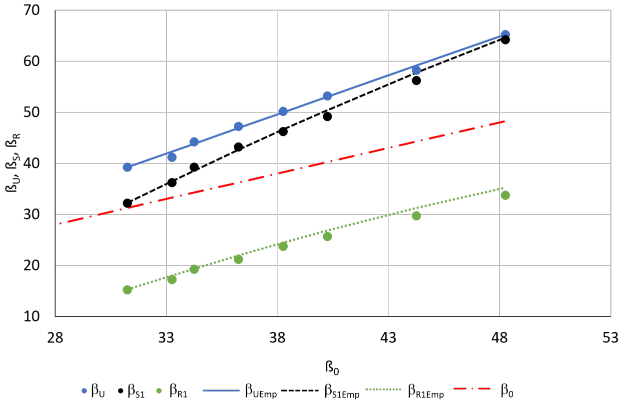

(c) Gap = $0.443\delta_{BL}$.

Figure 4.8: $\beta_U, \beta_S, \beta_R$ vs β_0 comparisons to empirical relations from Zheltovodov [3]. Current study (symbols), empirical equations (lines).

4.2 Incipient Separation

4.2.1 Effect of Leading-Edge Sweep on Incipient Separation

The vast majority of previous studies on incipient separation were performed with unswept rather than swept fins. In addition to decreasing the shock strength, the sweep angle changes the inviscid shock angle on the flat plate. This effect is apparent in Fig. 4.9 where the peak plateau pressure ratio is seen to decrease with an increase in sweep angle. The dashed black line shows the results from Eq. 2.4 with $k = 6.2$, the dot-dashed line is Eq. 2.4 with $k = 5.94$, the solid line is the current geometry at different α, and the symbols are from Zheltovodov and Knight [3] at different sweep angles. The values for the points from Zheltovodov and Knight in Fig. 4.9 are the peak plateau pressure ratio values take from Fig. 4.10. Plotted in Fig. 4.10 is the pressure ratio versus location moving along a line originating at the fin on the left and ending at the UIL on the right. Also of note in Fig. 4.10 is that as the sweep angle increases, the UIL moves closer to the fin surface reducing the size of the interaction region.

Generally in STBLI studies, the Korkegi criterion is evaluated to ensure separation or in providing the conditions required for incipient separation. Following this, the fin was rotated to a deflection angle of $\delta = 6\,\text{deg}$. For a Mach number of 2.5, and a total flow deflection angle of $\alpha = 7.25\,\text{deg}$ (deflection angle δ plus fin half angle of 1.25 deg), this case would show incipient separation for an unswept fin where $M_\infty \alpha = 2.5 \times 0.1265\text{ rad} = 0.316 > 0.3$. However, as observed in Fig. 4.11, no separation is seen upstream of the inviscid shock. This is because the leading-edge sweep weakens the shock and reduces the pressure such that the free-stream can overcome the pressure gradient. Taking the inviscid shock angle β_0 produced by the swept fin, and backing out a flow deflection angle α using wedge theory results in an effective

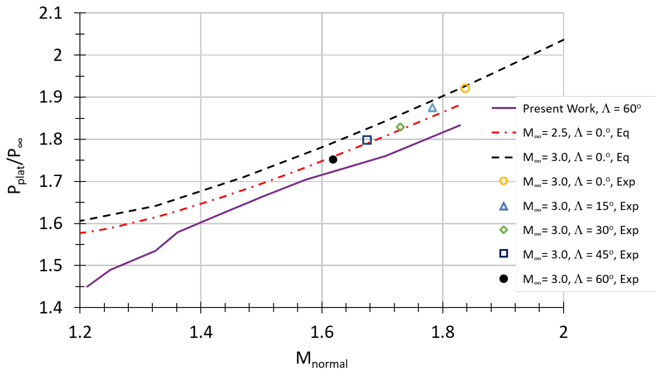

Figure 4.9: Peak plateau pressure vs normal Mach M_n. Solid line: current study, no gap; Dashed line: Eq. 2.4 $k = 6.2$; Dot-dash line: Eq. 2.4 $k = 5.94$; Symbols: experimental results from Zheltovodov[3] for various sweep angles, $M = 3.0$, $\delta = 20\,\text{deg}$.

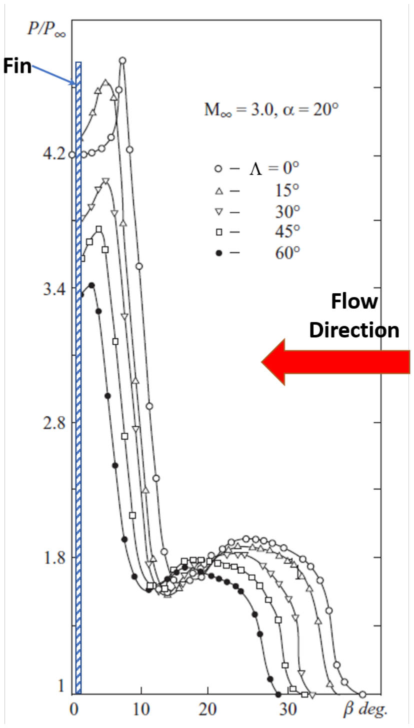

Figure 4.10: Pressure ratio vs incoming flow angle from Zheltovodov [3].

$\alpha = 4.5\,\text{deg}$, which is below the Korkegi criterion. Thus for a swept fin, the Korkegi criterion requires modification and should take into account the inviscid shock angle.

On a plane normal to the deflected fin, Fig. 4.12 shows the curved shock wave produced by the swept fin when it is deflected 6 deg, as computed by numerical Schlieren, for just the windward side of the fin. In order to better visualize the boundary layer, contours of turbulent kinetic energy are also shown. As the shock approaches the boundary layer, viscous effects cause it to dissipate, such that the shock does not extend completely to the plate surface. However, it does cause the boundary layer to slightly thicken as the flow moves from right to left, indicating slight separating between the shock and fin. As described previously, this separation

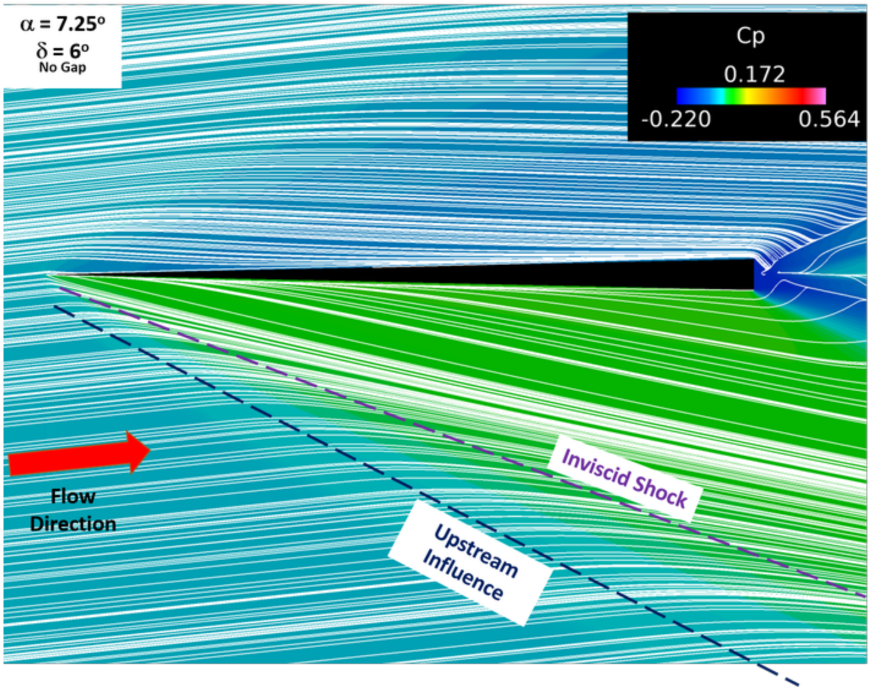

Figure 4.11: Streaklines on plate showing weakly unseparated interaction in Regime I. Plate is colored by pressure. $\delta = 6\,\text{deg}$, $\Lambda = 60\,\text{deg}$.

occurs downstream of the inviscid shock, and not upstream of it, which confirms no incipient separation yet.

Rather than relying solely on Korkegi, free interaction theory can be utilized to determine incipient separation if the Mach number normal to the inviscid shock (and therefor inviscid shock angle) is know. If after solving Eq. 2.3 the pressure ratio exceeds the incipient separation criterion of $\xi \geq 1.59$ separation can be expected. Additionally, the equation also reveals that for a pressure ratio between 1.59 - 1.69, a normal Mach number of 1.25 results in incipient separation. For the current results, the normal Mach number $M_n \ngtr 1.25$ until the incoming flow is deflected 12 deg (Fig. 4.14). Results of pressure ratio versus normal Mach over a range a Reynolds and Mach numbers were collected by Zheltovodov and Knight [3], and reproduced in Fig. 4.13, with the current results for $\delta = 12\,\text{deg}$ added (red dot), where δ is the angle

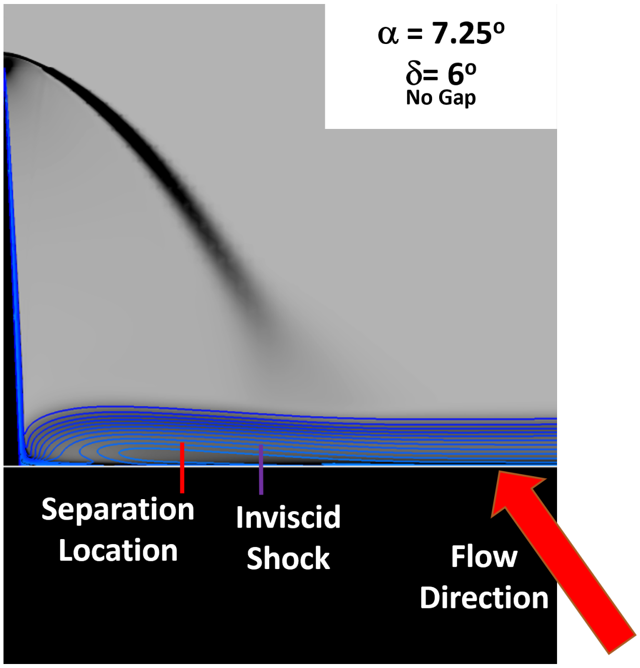

Figure 4.12: Numerical Schlieren showing shock wave due to swept fin. Windward side. Contours of turbulent kinetic energy added to highlight boundary layer. $\delta = 6\,\text{deg}$, $\Lambda = 60\,\text{deg}$.

between the free-stream and the fin centerline, not the fin surface. The $\delta = 12\,\text{deg}$ results plotted on Fig. 4.13 clearly fall in line with the range of data collected within the incipient separation area between the dotted lines separating regions I and II.

Indicated on Fig. 4.13 are three fundamental interaction regimes or domains. Interaction in region I occurs without boundary layer separation; incipient separation occurs on the boundary between regions I and II; boundary layer separation is present in region II; and region III displays secondary separation [77]. Secondary separation displays a second separation line within the interaction zone, which initially occurs downstream of the fin tip. As the incident angle or normal Mach number is increased, the secondary separation line extends towards the fin tip. The value of M_S (Mach when secondary separation first occurs) vary depending on the freestream Mach number, with larger M_∞ requiring larger M_n to produce secondary separation.

Zheltovodov proposed the criterion $M_\infty \alpha = 0.6$ for first occurrence of secondary separation [120].

Returning to the idea of an effective Mach number also points to $\delta = 12\,\mathrm{deg}$ as the incipient deflection angle. The inviscid shock angle for a flow deflection, $\alpha = 13.25\,\mathrm{deg}$ is $30\,\mathrm{deg}$ from the freestream flow. For a wedge to produce this shock angle would require a turning angle of only $8\,\mathrm{deg}$, resulting in $M_\infty \alpha = 0.35 > 0.3$, and incipient separation according to Korkegi. The present numerical results for $\delta = 12\,\mathrm{deg}$ confirm incipient separation theory using the normal Mach number, and effective α.

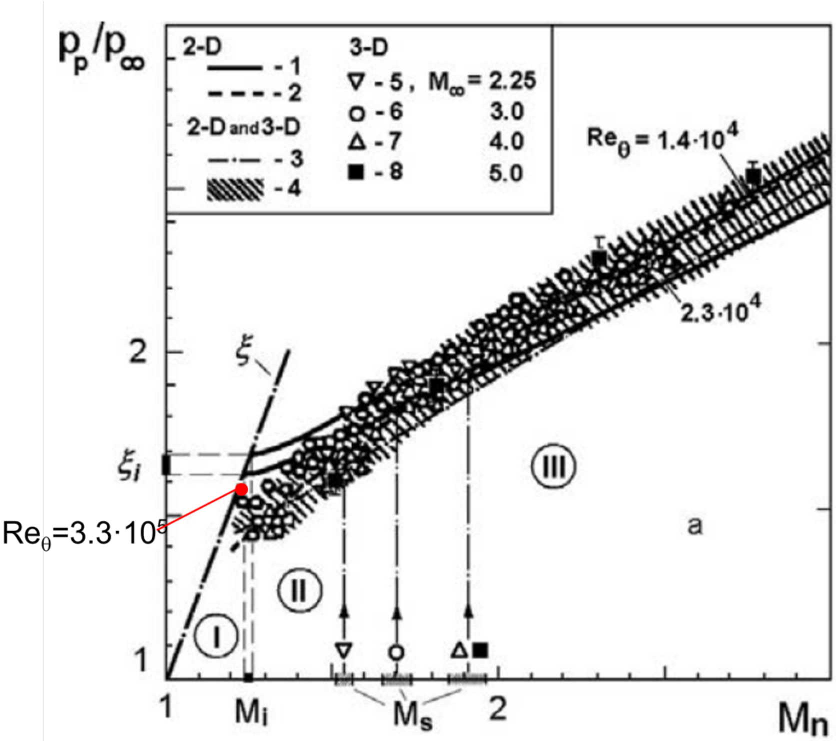

Figure 4.13: Plateau pressure comparison for 2D and 3D STBLI [3]. Current study: $\delta = 12\,\mathrm{deg}$ (red dot).

Streaklines on the plate around the fin are shown in Fig. 4.14. The purple line is the inviscid shock trace, the red line is the primary separation line, and the blue line indicates the upstream influence. Not shown is the virtual conical origin. Relative to the freestream, the inviscid shock angle for this case is 30 deg, and the primary separation line is 32 deg. The upstream influence angle is 38 deg, which agrees with experiments by Lu [19] as shown in Sec. 4.1. The skin friction coefficient increases significantly in the separation zone, unlike for 2D separation the friction is low due to slow flow in the separation bubble. Evidence that this case indicates incipient separation are the near-parallel inviscid shock angle and primary separation line [121]. This was observed by Zheltovodov and Knight as the flow angle was increased [3].

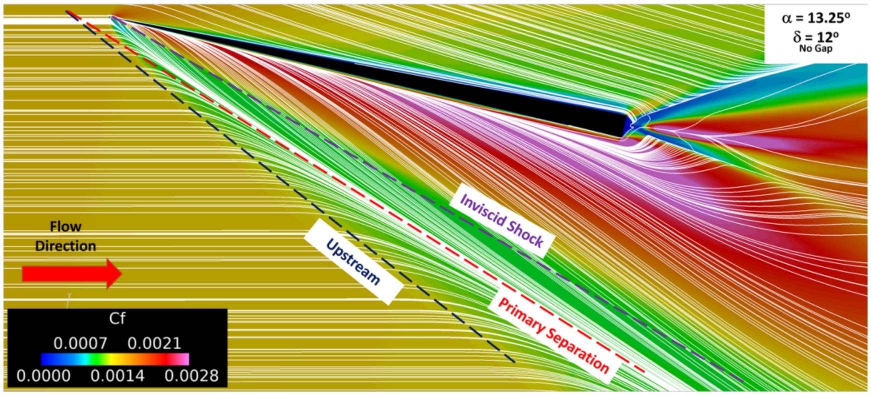

Figure 4.14: Streaklines on plate showing incipient separation. Plate is colored by skin friction coefficient c_f. Upstream influence (blue), primary separation (red), and inviscid shock trace (purple); $\delta = 12\,\text{deg}$, no gap.

Figure 4.15 shows the curved shock wave produced by the swept fin when it is deflected 12 deg, as computed by numerical Schlieren, for just the windward side of the fin. Contours of turbulent kinetic energy are also shown to visualize the boundary layer. Separation occurs upstream of the inviscid shock in this case, which causes the boundary layer to thicken. This thickening results in the familiar λ shock pattern seen with flow separation.

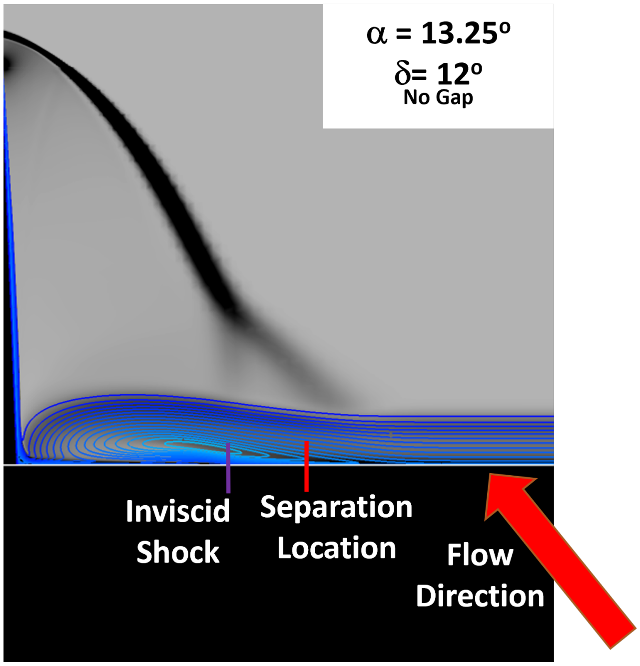

Figure 4.15: Numerical Schlieren showing shock wave due to swept fin. Windward side. Contours of turbulent kinetic energy added to highlight boundary layer. $\delta = 12\,\text{deg}$, $\Lambda = 60\,\text{deg}$.

A tight and distinct core within the interaction region is visualized by the velocity vectors on a plane normal to the fin located at $x/c = 0.6$ in Fig. 4.16, with the vectors colored by Mach number. The separation location S1 and attachment point R1 are notated in the figure. The evolution of the vortex core is seen in Fig. 4.16b where the cut plane is now located at $x/c = 0.9$. It is observed that not only does the vortex grow, but the core shifts away from the fin and moves vertically by a small amount. The same scale is used in both images of 4.16, and therefor the separation line is out of view in Fig. 4.16b. From the streamlines in Fig. 4.17 it is seen that streamlines near the fin and originating at a height above the plate of

$0.221\delta_{BL}$ roll into this vortex. Streamlines originating further from the fin are turned by the shock and eventually roll into the vortex as well.

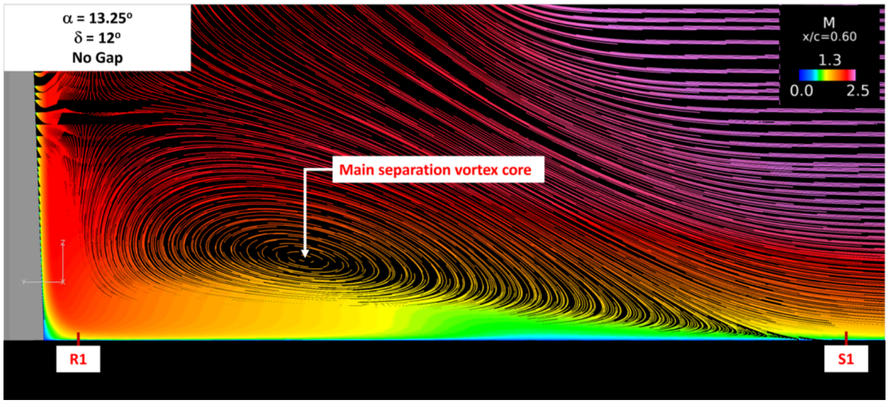

(a) $x/c = 0.60$. Vortex core located 14.34 mm outboard of and 3.968 mm above fin leading edge tip.

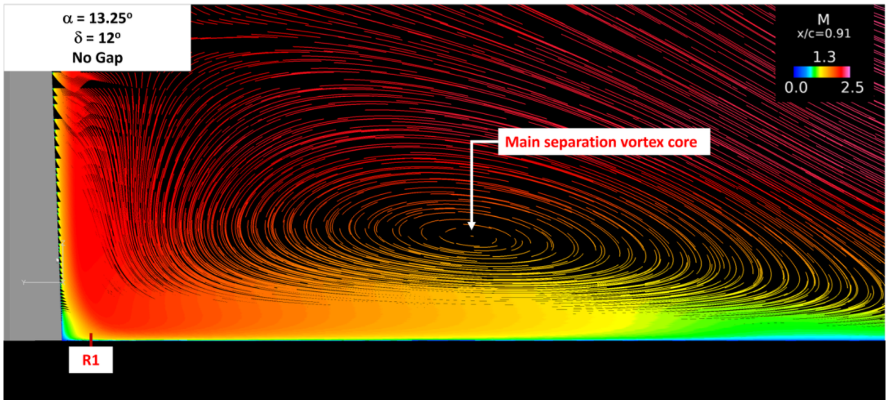

(b) $x/c = 0.90$. Vortex core located 22.68 mm outboard of and 5.165 mm above fin leading edge tip.

Figure 4.16: Fin $\delta = 12\,\text{deg}$, no gap. Velocity vectors normal to fin. Colored by Mach number.

4.2.2 Effect of Fin/Plate Gap on Incipient Separation

Following the case described above where no gap exists between the fin and the plate, the same flow conditions for incipient separation were ran for configurations with $0.221\delta_{BL}$ and $0.443\delta_{BL}$ gaps. While the introduction of the gap resulted in the

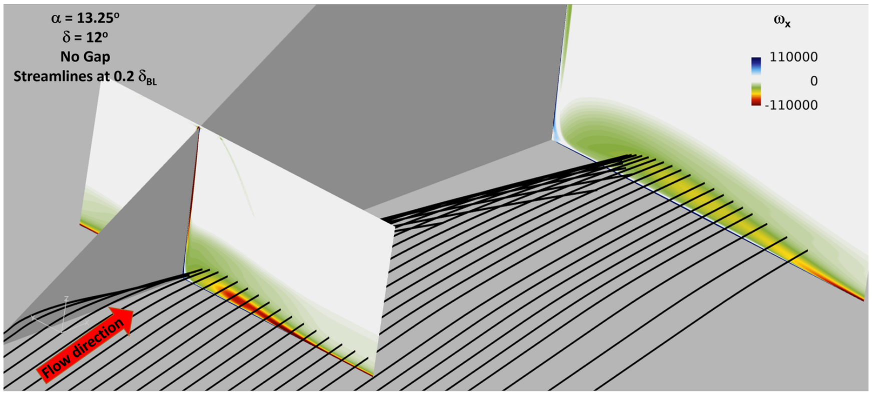

Figure 4.17: Contours of streamwise vorticity ω_x with streamlines. Streamlines originate at 0.2 δ_{BL}. Fin $\delta = 12\,\text{deg}$, no gap.

VCO shifting closer to the fin leading edge, the separation and upstream influence angles were unchanged. This is illustrated in Figs. 4.18a and 4.18b, where the streaklines on the plate are shown. From these figures, it appears that flow through the gap relieves some of the pressure due to the shock wave. This translates the primary separation line closer to the fin tip without changing the angle. This translation also brings the VCO closer to the fin tip. Other than causing the shift in the separation line on the windward side of the fin, this flow through the gap causes flow separation to occur on the leeward side of the fin. This separation feature can be seen at the top of Figs. 4.18a and 4.18b. The separation line on the leeward side appears to slightly shift as the gap height is increased. Additionally, the larger gap height causes the separation line to become more freestream flow aligned due to more crossflow through the gap.

Can be seen in Fig. 4.19 that as the gap increases the BL thickness decreases. Due to flow ”escaping” through gap. Relieving effect.

The effect of the gap on streamlines is shown in Fig. 4.20. The streamlines in Figs. 4.20a and 4.20b are in the same position relative to the root of the fin as in the no gap case shown in Fig. 4.17. Figure 4.20c however, places the streamlines at the

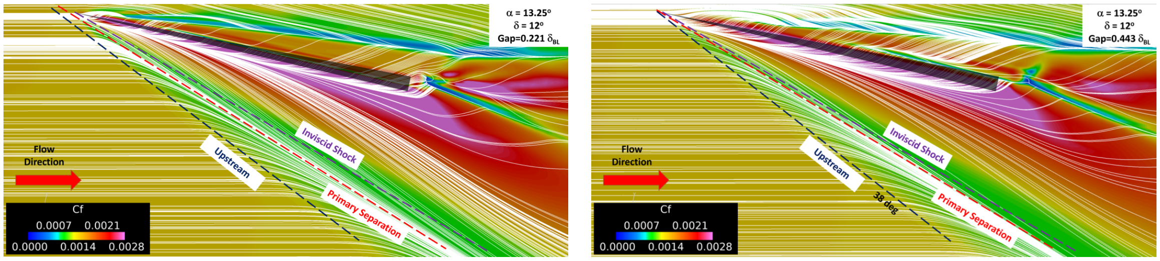

(a) Gap = $0.221\delta_{BL}$.

(b) Gap = $0.443\delta_{BL}$.

Figure 4.18: Surface streaklines on plate showing incipient separation for the cases with a gap, $\delta = 12\,\text{deg}$, color coded by skin friction coefficient; upstream influence (blue), primary separation (red), and inviscid shock trace (purple).

same position relative to the plate and boundary layer as Fig. 4.17. In comparing Figs. 4.20a and 4.20b to Fig. 4.17 it is observed that if streamlines originate at the same location relative to the fin root, the gap has little affect on their behavior. For both gap cases, the streamlines closest to the fin roll into the vortex. However, in the case of the larger gap, some streamlines are seen to pass through the gap instead of being completely captured by the vortex. Additionally, we compare Fig. 4.20c in which the streamlines originate at the same position relative to the fin as the no gap case in Fig. 4.17. In both cases the streamlines originate at a vertical position off the plate of 0.221 δ_{BL}. As observed in Fig. 4.20c the gap causes some streamlines to flow through the gap and other streamlines terminate on the plate surface, rather than roll into the vortex.

To further illustrate what is occurring in the flow, velocity vectors on a plane normal to the fin surface (YZ plane) are shown in Figures 4.21 and 4.22. Just as with the no gap case of Fig. 4.16, vectors are colored by Mach number. Depicted in Fig. 4.21 are vectors at a YZ plane located at 60% of the fin chord, with Fig. 4.21a showing a gap if $0.221\delta_{BL}$ and Fig. 4.21b for a gap of $0.443\delta_{BL}$. Figure 4.22 shows the same, but at a YZ plane located at 91% of the chord. Table 4.1 gives the coordinates for the vortex cores shown in the figures. The z location of the core is recorded

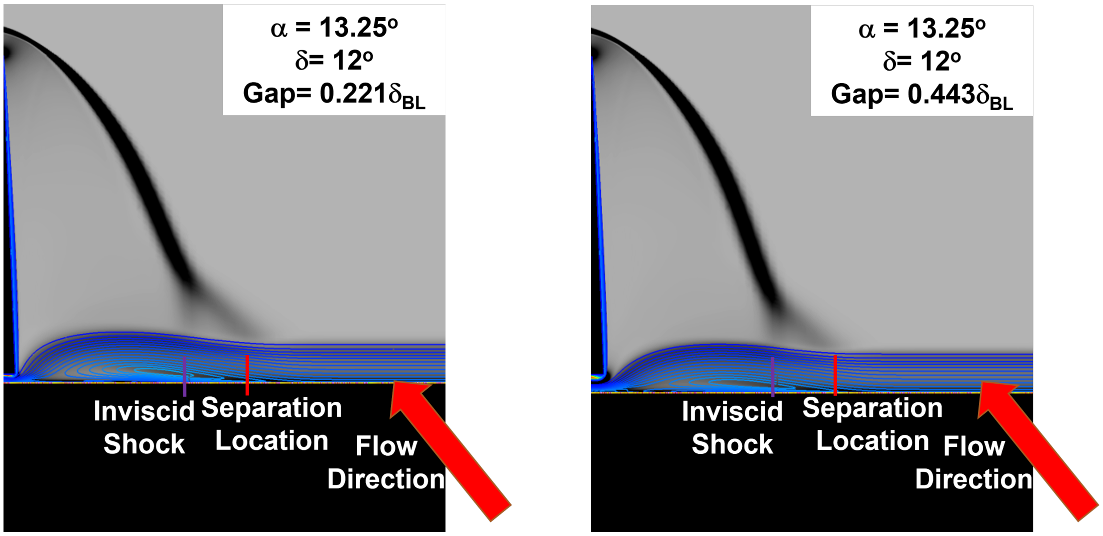

(a) Gap $= 0.221\delta_{BL}$ (b) Gap $= 0.443\delta_{BL}$.

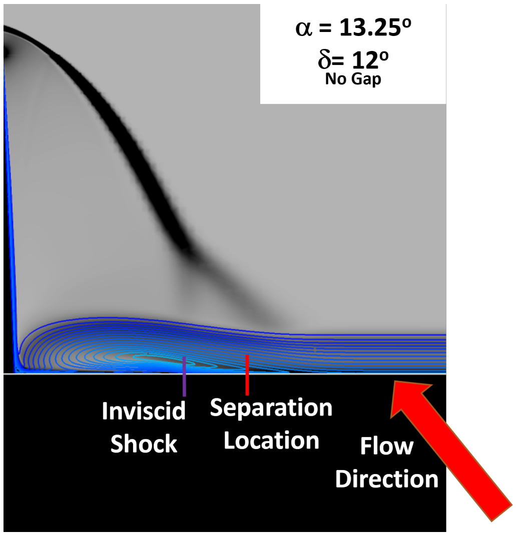

(c) No gap.

Figure 4.19: Numerical Schlieren showing shock wave due to swept fin. Windward side. Contours of turbulent kinetic energy added to highlight boundary layer. $\delta = 12\,\mathrm{deg}$, $\Lambda = 60\,\mathrm{deg}$.

referenced to both the fin root and the plate. From the figures and the table it is observed that the addition of the gap causes the vortex core to shift vertically, with it moving downwards towards the plate as the gap increases. The distance between the plate and the vortex core decreases as the gap height increases. Introducing the

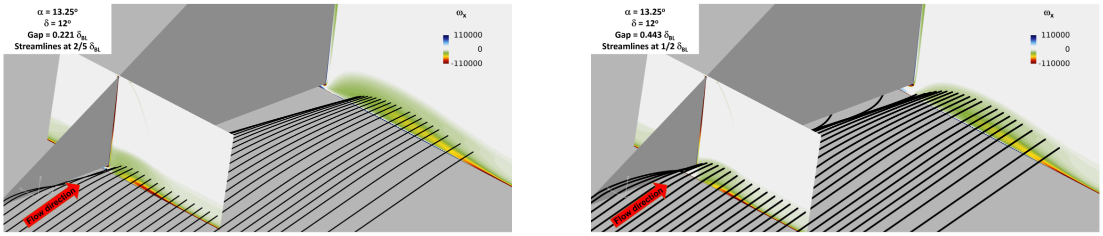

(a) Gap $= 0.221\delta_{BL}$. Streamlines originate at 0.4 δ_{BL}.

(b) Gap $= 0.443\delta_{BL}$. Streamlines originate at 0.5 δ_{BL}.

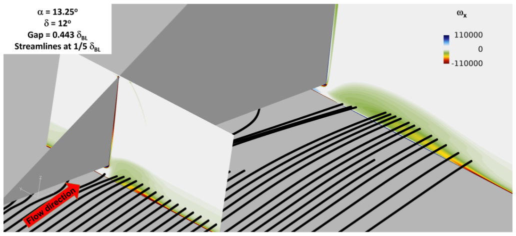

(c) Gap $= 0.443\delta_{BL}$. Streamlines originate at 0.2 δ_{BL}.

Figure 4.20: Contours of streamwise vorticity on the windward side, $\delta = 12\,\text{deg}$.

gap creates flow to egress the windward SBLI region through the gap which weakens the vortex, causing the downward shift. This weakening, coupled with flow through the gap, also causes the attachment point R1 to shift further from the fin. The shift in R1 due to the gap causes the vortex core to move outward, away from the fin. As the gap is increased, the vortex core is seen to move further outward.

Table 4.1: Vortex Core Locations

Gap	x/c	y (mm)	z (mm) relative to fin root	z (mm) relative to plate
0.00	0.60	14.0	3.9	3.9
$0.221\delta_{BL}$	0.60	15.0	1.9	3.1
$0.443\delta_{BL}$	0.60	16.0	0.06	2.5
0.00	0.91	22.0	5.1	5.1
$0.221\delta_{BL}$	0.91	23.0	3.1	4.1
$0.443\delta_{BL}$	0.91	24.0	1.3	3.9

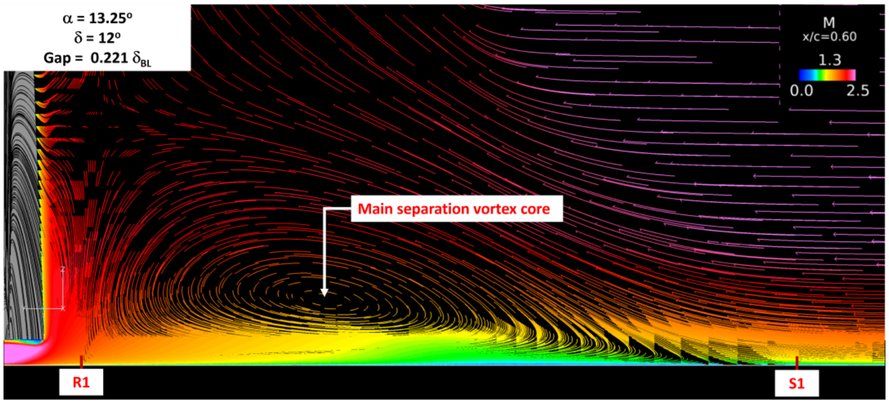

(a) Gap $= 0.221\delta_{BL}$. Vortex core located 15.0 mm outboard of and 1.9 mm above fin leading edge tip.

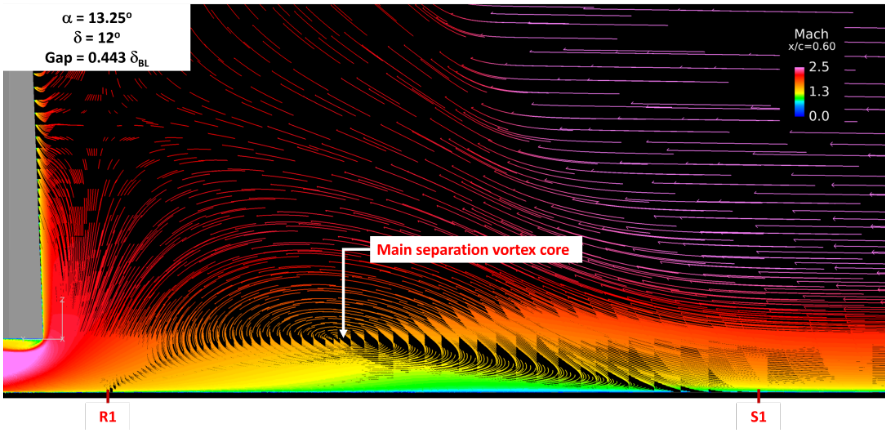

(b) Gap $= 0.443\delta_{BL}$. Vortex core located 16.0 mm outboard of and 0.06 mm above fin leading edge tip.

Figure 4.21: Fin $\delta = 12\,\text{deg}$, $x/c = 0.60$. Velocity vectors normal to fin. Colored by Mach number.

4.3 Surface Pressure Distribution

Just as the increasing sweep angle reduces the peak plateau pressure, so too an increasing gap reduces the peak plateau pressure. This decrease in peak plateau pressure is shown in Fig. 4.23 which plots the plateau pressure ratio for each of the gaps versus normal Mach number. The solid black line plots the results for the 60 deg swept fin without a gap. The green dashed line plots the gap of $0.221\delta_{BL}$, the double-dot-dashed purple line is for $g = 0.443\delta_{BL}$, and the red dot-dashed line is from Eq.

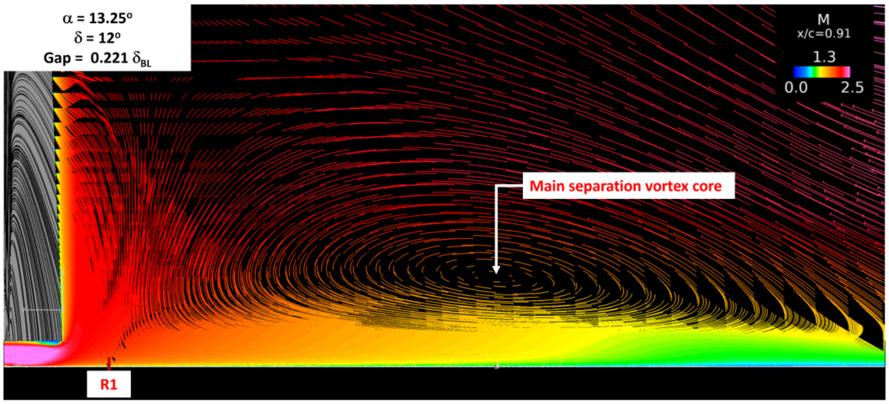

(a) Gap $= 0.221\delta_{BL}$. Vortex core located 23.0 mm outboard of and 3.1 mm above fin leading edge tip.

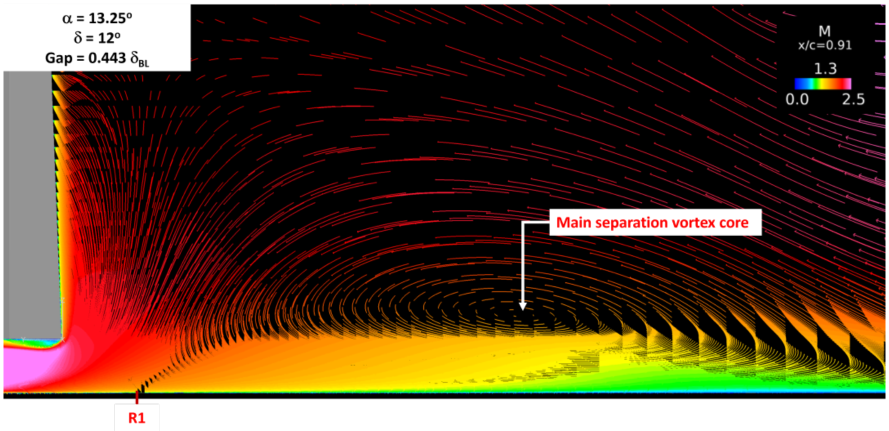

(b) Gap $= 0.443\delta_{BL}$. Vortex core located 24.0 mm outboard of and 1.3 mm above fin leading edge tip.

Figure 4.22: Fin $\delta = 12\,\text{deg}$, $x/c = 0.90$. Velocity vectors normal to fin. Colored by Mach number.

2.4. This decrease in plateau pressure is due to the pressure relieving effect the gap provides.

As seen in Fig. 4.10, the maximum surface pressure also decreases with increasing fin sweep angle. The maximum pressure for an unswept fin can be determined using the relation to M_n given by Scuderi [122]

$$\frac{P_{max}}{P_\infty} = 1.167M_n^{2.2} - 0.167 \tag{4.8}$$

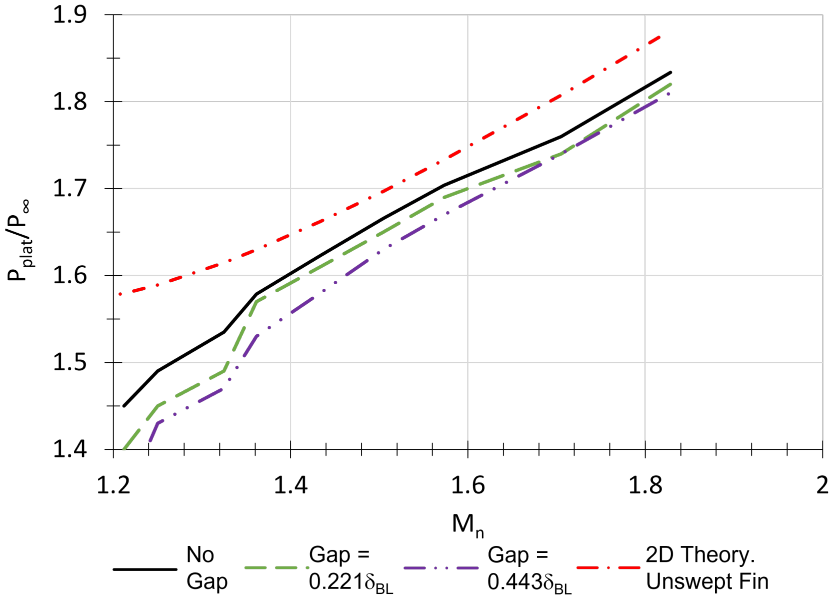

Figure 4.23: Peak plateau pressure vs normal Mach M_n. Solid line: current study, no gap; Dashed line: current study $g = 0.221\delta_{BL}$; Double-dot-dashed line: current study $g = 0.443\delta_{BL}$; Dot-dash line: Eq. 2.4 $k = 5.94$

Comparisons between this equation and the current study for each gap height are given in Fig. 4.24 where the solid black line plots the results for the 60 deg swept fin without a gap, the green dashed line plots the gap of $0.221\delta_{BL}$, the double-dot-dashed purple line is for $g = 0.443\delta_{BL}$, and the red dot-dashed line is from Eq. 4.8.

Example of surface pressure distribution for each gap is in Fig. 4.25

4.4 Leeside Flow

A complex flow is established on the leeside with or without a gap, as shown in Figs. 4.26–4.28. The addition of a gap further produces numerous mean flow structures on the leeward side of the fin, as seen in Figs 4.28. At non-zero deflection angles, a pressure difference occurs between the leeward and windward sides of the fin. Coupled with the pressure difference are large pressure gradients at the leading-edge which causes flow to cross from the leeward to the windward side. Due to

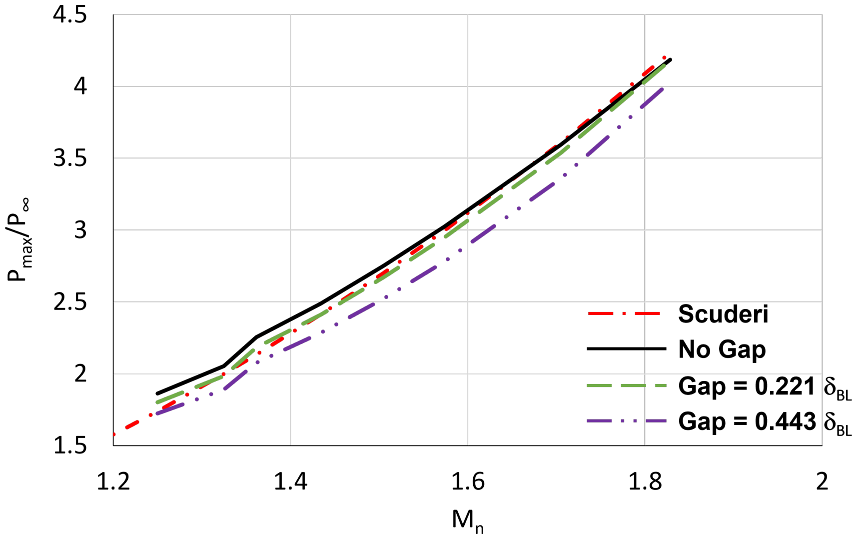

Figure 4.24: Maximum normalized surface pressure vs normal Mach M_n. Solid line: current study, no gap; Dashed line: current study $g = 0.221\delta_{BL}$; Double-dot-dashed line: current study $g = 0.443\delta_{BL}$; Dot-dash line: Eq. 4.8 from [122]

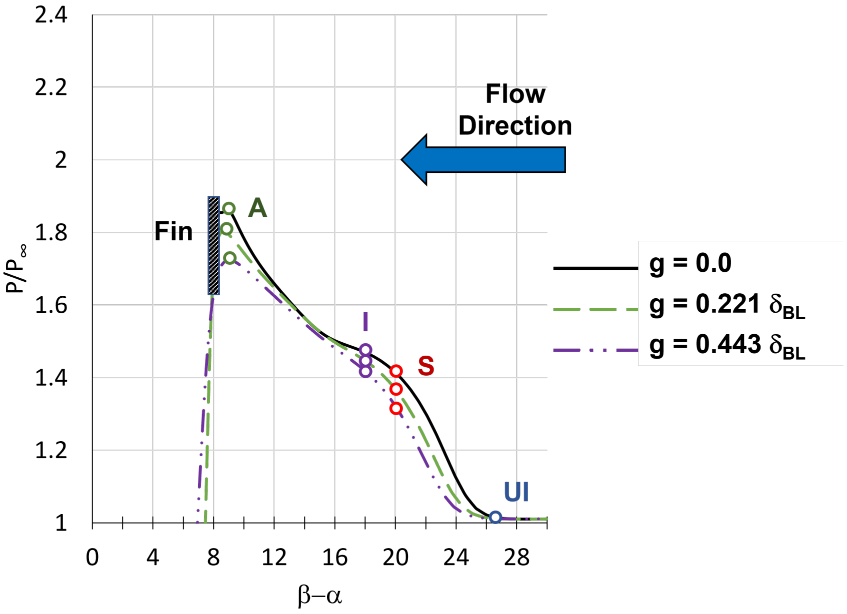

Figure 4.25: Surface pressure distribution. Solid line: current study, no gap; Dashed line: current study $g = 0.221\delta_{BL}$; Double-dot-dashed line: current study $g = 0.443\delta_{BL}$. $M_n = 2.5$ $\delta = 12\,\text{deg}$, $\Lambda = 60\,\text{deg}$.

flow separation and viscous effects vorticity is generated which in turn allows for the creation of vortices. These leading-edge vortices form close to the fin surface rather than further into the freestream normal to the fin surface [29, 30, 31]. To illustrate this vortex, streamlines generated by the fin leading-edge tip are shown in Fig. 4.26. The upper streamlines trace the leading-edge vortices, while the lower streamlines follow a separation line. The separation line can be seen dividing the red and yellow sections of the fin in Fig. 4.27. Regardless of the presence of a gap or not, the lower vortex exists, and is little changed due to the gap.

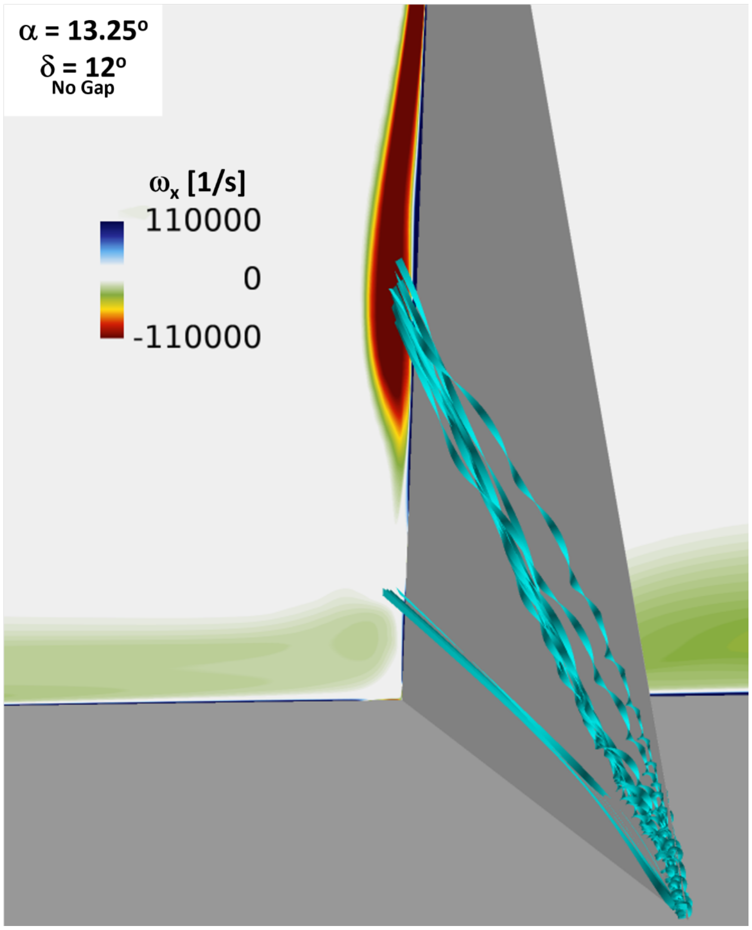

Figure 4.26: Contours of streamwise vorticity on leeward side of fin. Fin leading-edge generates vortex, illustrated by streamlines (colored for appearance). Lower streamline follows lowest separation line. $\delta = 12\,\text{deg}$, no gap.

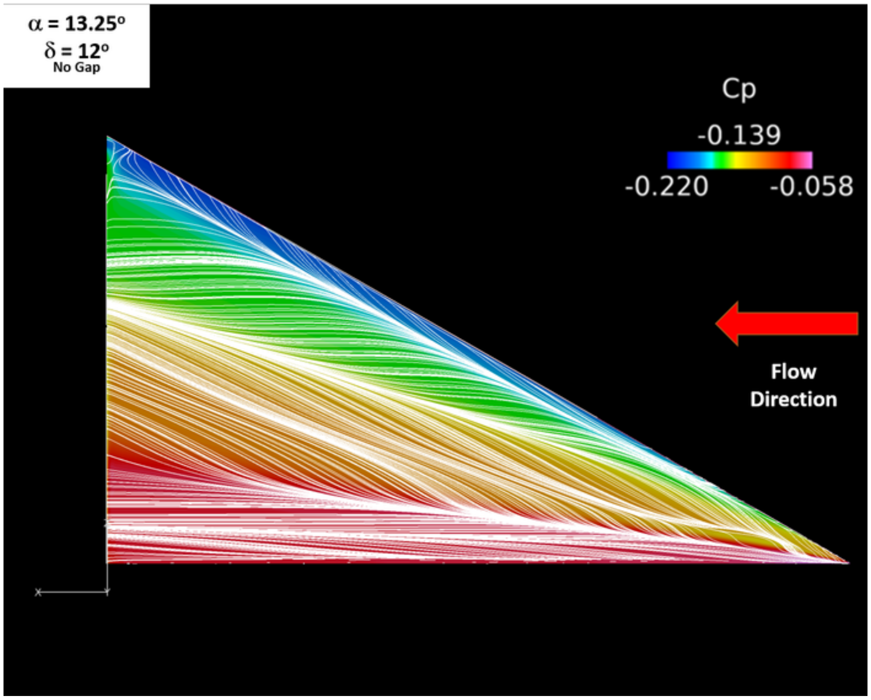

Figure 4.27: Contours of fin leeside pressure coefficient with surface streaklines. $\delta = 12\,\text{deg}$, no gap.

4.4.1 Appearance of Plate Vortex

A unique feature caused by adding a gap is the creation of an additional vortex above the plate. This is somewhat similar to a half-cone-delta-wing as studied by Peake [12]. In the present study, the vortex is set up by separation at the fin tip and moves downstream as shown by the streamlines in Fig. 4.28. Due to the gap, flow coming from between the fin and plate becomes entrained with the vortex as seen in Fig. 4.28a. As the gap is increased, the vortex core gets pushed away from the fin and becomes less circular as shown by the series of ω_x in Fig. 4.29. This is due to a higher mass flow rate of air coming through the gap and breaking down the vortex. The contours of streamwise vorticity are added to further depict the location of the vortices.

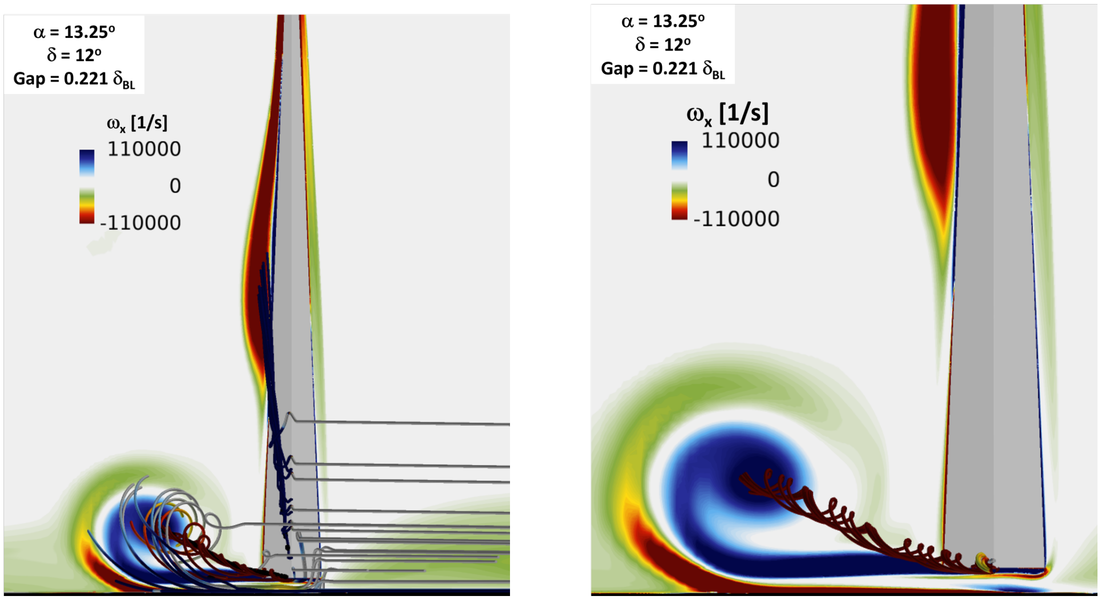

(a) Front view.

(b) Zoomed

Figure 4.28: Contours of streamwise vorticity on leeward side of fin. Fin leading-edge in combination with gap generates two vortexes, illustrated by streamlines (colored for appearance); $\delta = 12\,\mathrm{deg}$, Gap $= 0.221\delta_{BL}$.

The vortex core location for the $0.221\delta_{BL}$ case was determined using eigenmode analysis. During eigenmode analysis, the real components of the eigen-analysis of the velocity gradient tensor are used to determine the axis of swirl[118, 123]. The vortex core center-line is said to have pierced a cell if after subtracting the swirl direction from the nodal velocity, two or more cell faces have zero reduced velocities [118]. This vortex core is shown in Fig. 4.29a along with contours of vorticity magnitude $|\omega| = \sqrt{\omega_x^2 + \omega_y^2 + \omega_z^2}$ and isosurfaces of constant streamwise vorticity. Blue isosurfaces are vortices with positive ω_x, and red isosurfaces have negative streamwise vorticity. The large red isosurface on the fin, away from the flat plate junction, is the same vortex that a delta wing produces. The blue and red isosurfaces around the flat plate junction are unique to the fin with a gap. The positive ω_x vortex is generated at the fin leading-edge tip. This sets up a counter-clockwise vortex at the plate surface. The same process occurs for the larger fin gap as shown in Fig. 4.29b. In this case, the counter-clockwise vortex on the plate surface does not develop until further downstream. It can also be seen from the isosurfaces that the main clockwise vortex is less circular for the larger gap, than for the smaller gap. In both cases, the vortices originate due to flow separation and terminate at the computational domain. Thus they follow Helmholtz's vortex theorems.

The vortex originating from the plate surface due to a fin gap is attributed to flow separation on the leeward side. In order to see the separation line causing the vortex, figure 4.30 depicts a top-down zoomed in view of the leading edge of the fin. Flow is from the bottom left to top right, with the fin shown in blue. In this view, the top half of the image is the leeward side, and the bottom half of the image is windward side. Black surface streaklines are shown on the plate. Converging surface streaklines on the leeward side reveal two separation lines. Isosurfaces of streamwise vorticity are added in Fig. 4.30b, and show the vortex centered on the outer separation line.

Flow separates on the leeward side due to an adverse pressure gradient caused by high speed flow traveling through the gap, as shown in Fig. 4.31 by pressure contours on cut planes located at $x/c = 0.13$ and $x/c = 0.32$ from the fin leading edge. Figure 4.32 provides contour plots of velocity normal to the fin at the same chordwise locations. In both sets of figures, the surface streaklines are shown on the plate, as well as lines of separation. The lines of separation were computed by FieldView following the phase plane analysis method of Kenwright [124, 125]. This method identifies and displays cells where the stream function is zero or singular [118]. Figure 4.32a displays the velocity contours on cut plane 13% downstream of the fin leading edge, where the separation initiates. A cut plane where the vortex is fully

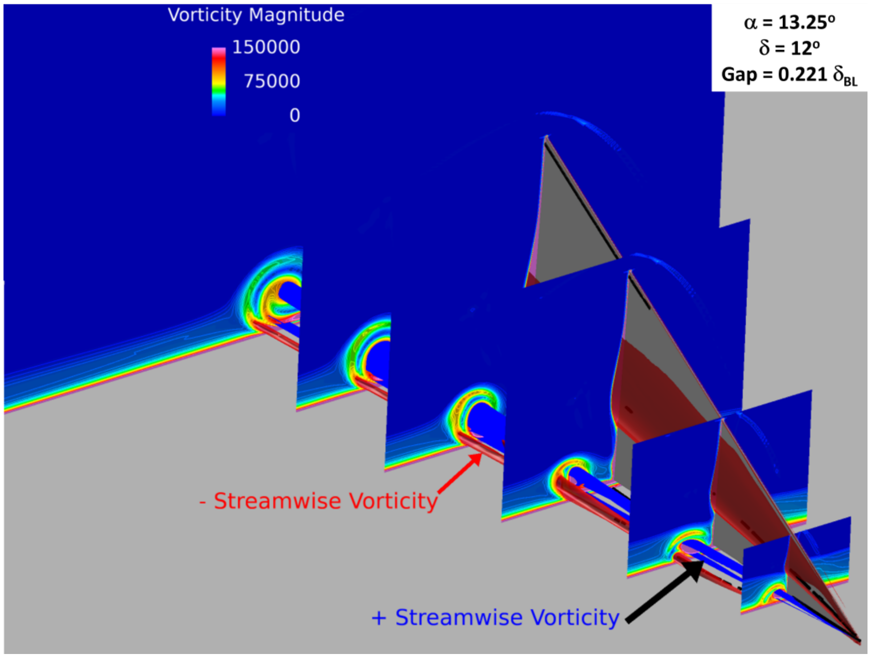

(a) Gap = $0.221\delta_{BL}$.

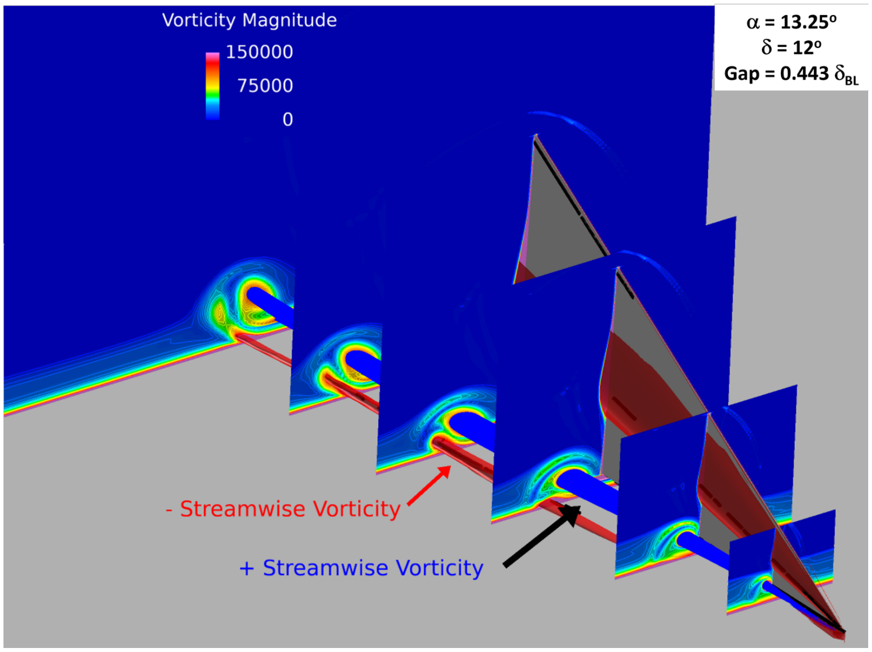

(b) Gap = $0.443\delta_{BL}$.

Figure 4.29: Contours of vorticity magnitude on leeward side of fin. Isosurfaces of streamwise vorticity illustrate clockwise vortices generated by fin leading-edge (blue) and counter-clockwise vortices generated by the gap (red); $\delta = 12\,\mathrm{deg}$

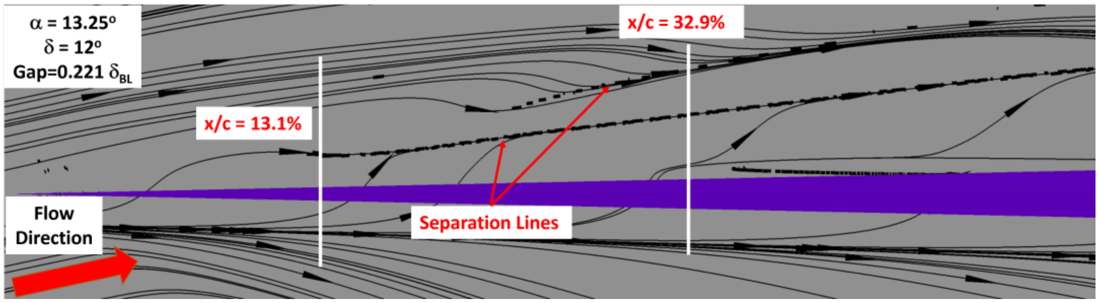

(a) Surface streaklines on plate.

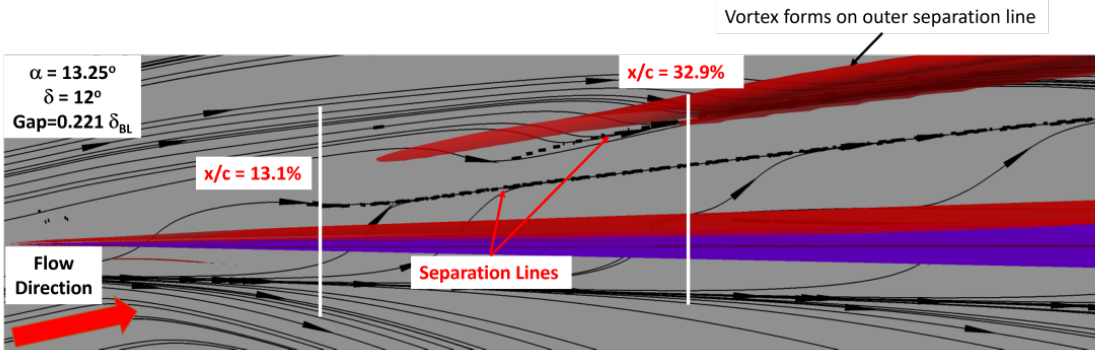

(b) Surface streaklines and isosurfaces of streamwise vorticity.

Figure 4.30: Gap $= 0.221\delta_{BL}$; $\delta = 12\,\mathrm{deg}$

developed, at approximately x/c =33%, is given in Fig. 4.32b. These figures clearly show the high-speed flow which travels through the gap into a region of relatively low speed flow normal to the fin. This high-speed flow, accompanied by a reduction in pressure, creates the adverse pressure gradient causing the flow to separate. As the flow separates, a vortex is generated.

In order to see the development of the vortices, contours of streamwise vorticity on a plane at four different chordwise locations for each gap height are shown in Figs. 4.33 – 4.36. These figures clearly illustrate the complex flow which is established on the leeside due to the presence of a gap. Looking first at Fig. 4.33, the streamwise vorticity at 13% of the chord for each gap is presented. From this figure, it is seen that the gap causes a vortex to form at the fin root due to the airflow coming through the

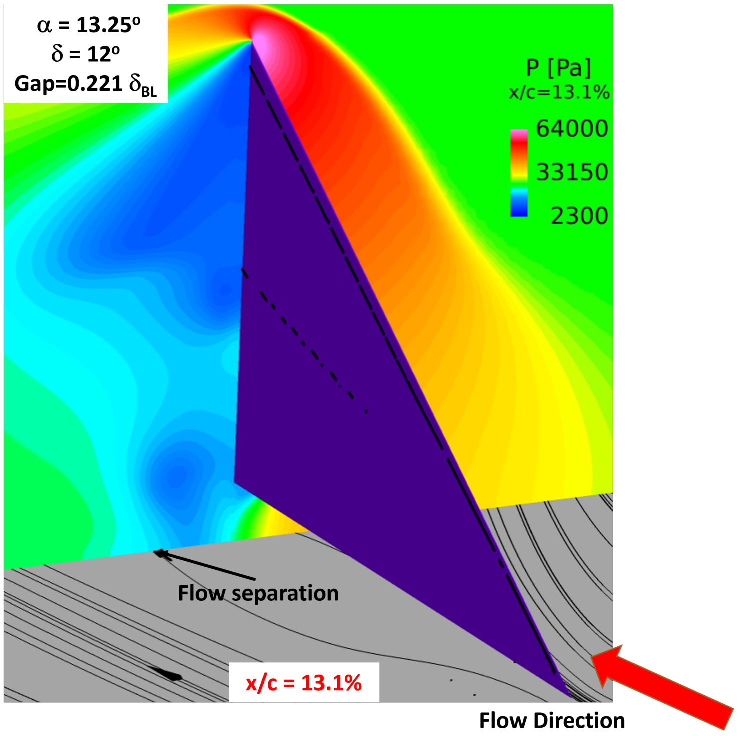

(a) x/c=0.131

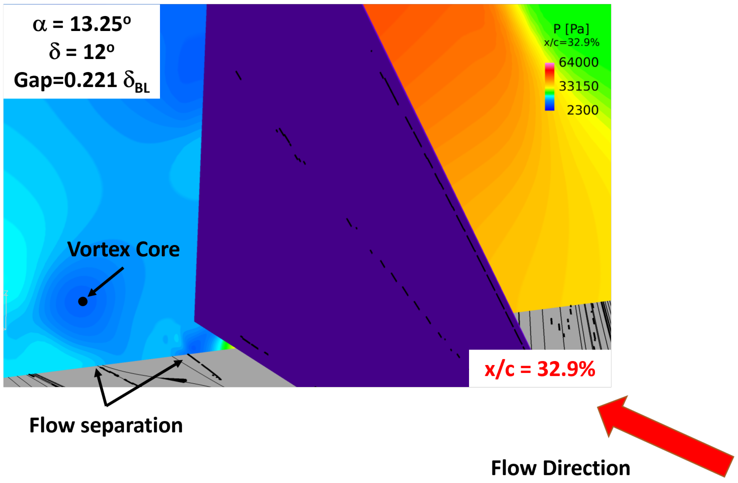

(b) x/c=0.329

Figure 4.31: Pressure contours at two different chordwise locations. Gap $= 0.221\delta_{BL}$; $\delta = 12\,\mathrm{deg}$

gap at the fin leading-edge tip, as described earlier. At $x/c = 0.26$ Fig. 4.34c shows the development of the vortex from the plate for each of the gap cases, as discussed

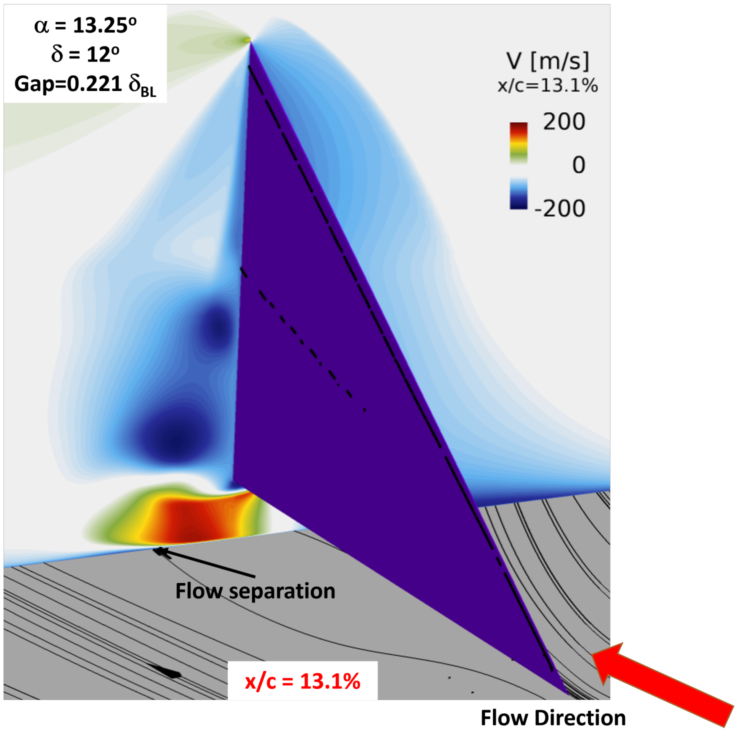

(a) x/c=0.131.

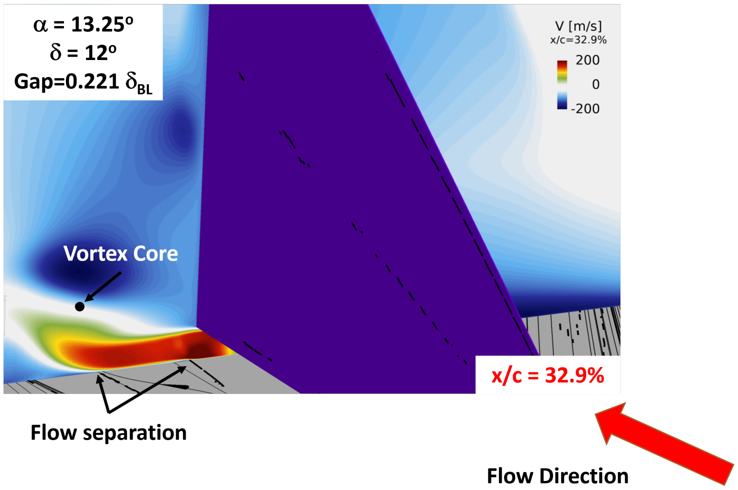

(b) x/c=0.329

Figure 4.32: Velocity contours normal to the fin at two different chordwise locations. Gap $= 0.221\delta_{BL}$; $\delta = 12\,\text{deg}$

in Fig. 4.28 as well. It is observed in Fig. 4.34b that while the plate vortex for the gap height of $0.221\delta_{BL}$ is almost fully formed, Fig. 4.34c shows the vortex for the larger gap height is just starting to form. Further downstream at $x/c = 0.43$, with a gap height of $0.221\delta_{BL}$ Fig. 4.35b shows the plate vortex starting to roll into the fin vortex, while the plate vortex is not yet fully formed for a gap height of $0.443\delta_{BL}$ shown in Fig. 4.35c. Finally, at $x/c = 0.75$, the plate vortex formed from the flow through a gap height of $0.221\delta_{BL}$ is now almost completely rolled into the fin vortex as seen in Fig. 4.36b. However, Fig. 4.36c shows that for the larger gap height, the plate vortex is just now starting to roll into the fin vortex.

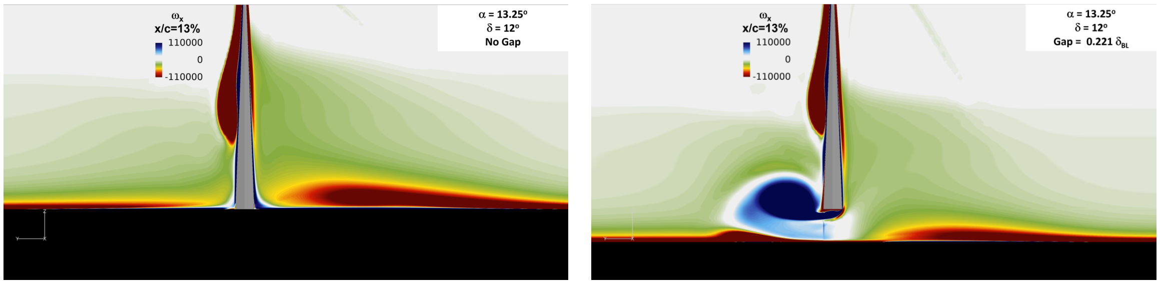

(a) No gap.

(b) Gap = $0.221\delta_{BL}$.

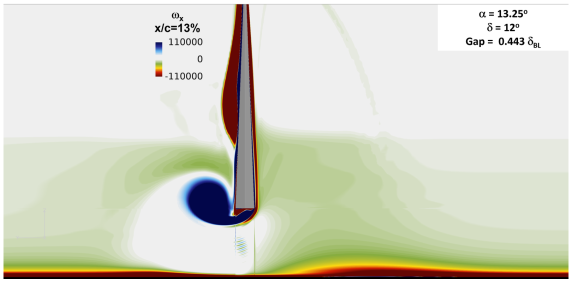

(c) Gap = $0.443\delta_{BL}$.

Figure 4.33: Contours of streamwise vorticity ω_x on YZ plane at $x/c = 0.13$, $\delta = 12\,\text{deg}$.

While the plate surface flow is greatly affected due to the gap, the flow on the leeward side of the fin surface itself is little changed, as shown in Figs. 4.37a through 4.37c. The separation and attachment lines move slightly upward as the gap increases due to the flow leaking through the gap. This was also seen by the small movement of the region of high vorticity in Fig. 4.33.

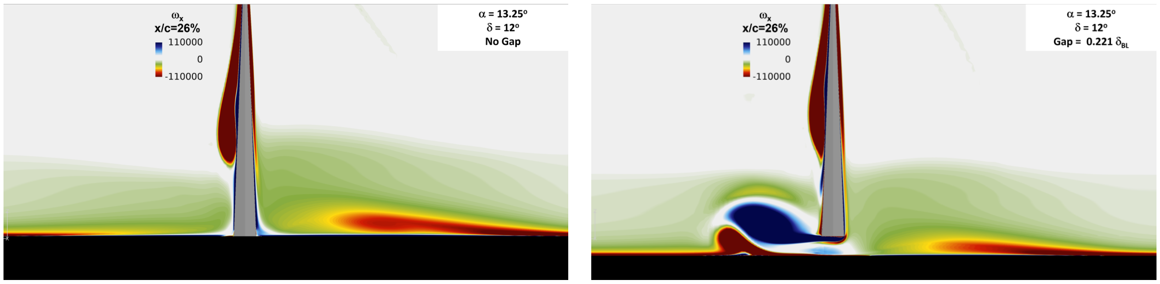

(a) No gap. (b) Gap = $0.221\delta_{BL}$.

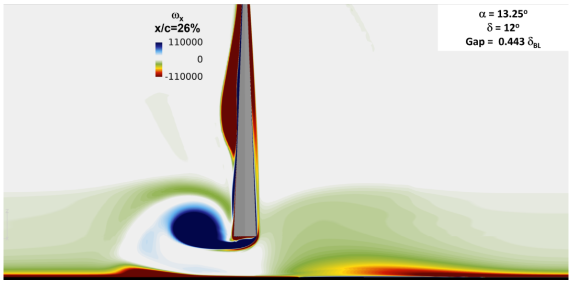

(c) Gap = $0.443\delta_{BL}$.

Figure 4.34: Contours of streamwise vorticity ω_x on YZ plane at $x/c = 0.26$, $\delta = 12\,\text{deg}$.

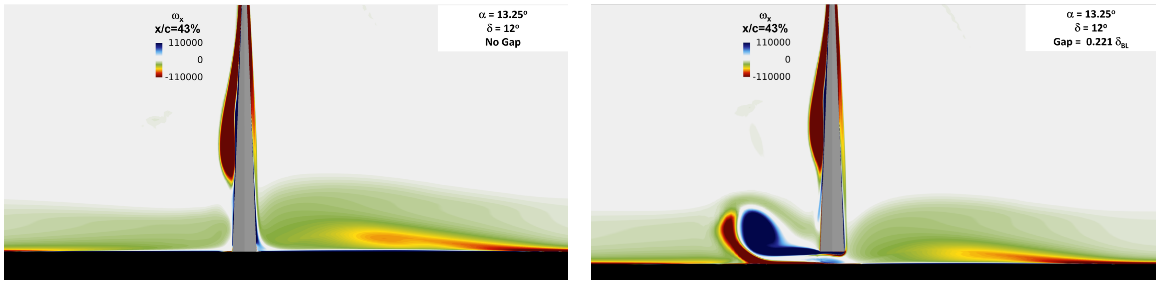

(a) No gap. (b) Gap = $0.221\delta_{BL}$.

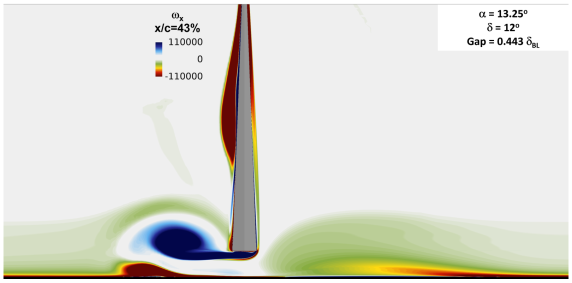

(c) Gap = $0.443\delta_{BL}$.

Figure 4.35: Contours of streamwise vorticity ω_x on YZ plane at $x/c = 0.43$, $\delta = 12\,\text{deg}$.

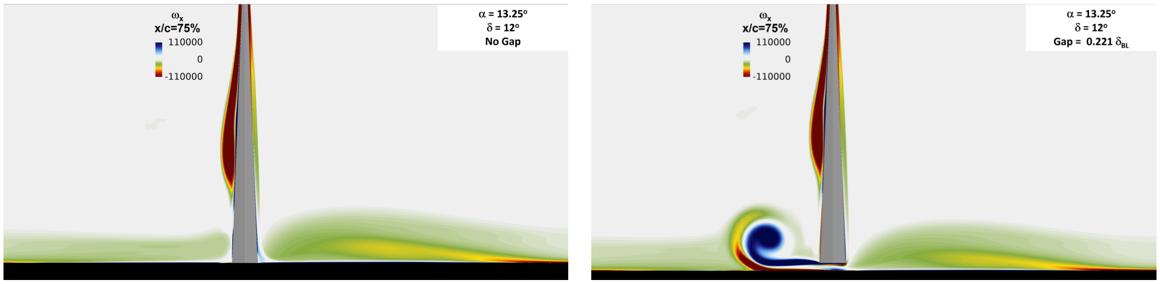

(a) No gap. (b) Gap = $0.221\delta_{BL}$.

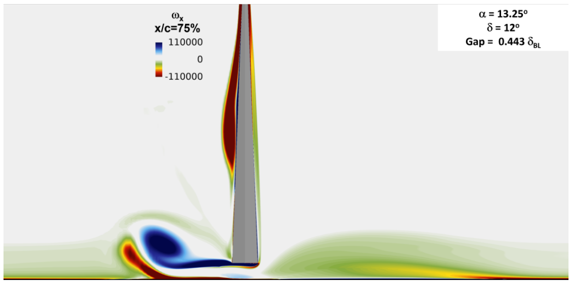

(c) Gap = $0.443\delta_{BL}$.

Figure 4.36: Contours of streamwise vorticity ω_x on YZ plane at $x/c = 0.75$, $\delta = 12\,\text{deg}$.

4.4.2 Flow Characteristics on Leeside Delta Wing

During the analysis of the plate vortex in the previous section, the similarity between the leeside of the fin and a delta wing was noted. This similarity was investigated as a means to determine the extent of the similarities and as a means to qualitatively validate the CFD results on the leeside of the fin.

Delta wings are commonly encountered on supersonic and hypersonic flight vehicles, especially in the early days of high-speed flight. In the absence of high-fidelity computational methods, numerous wind tunnel experiments were carried out to develop empirical relations between the wing geometry and flight conditions. Experiments by Stanbrook and Squire [25, 32] determined six different flow regimes on the leeward side of a delta wing, as shown in Fig. 4.38. The six different regimes are: shock with no separation; shock-induced separation; separation bubble with

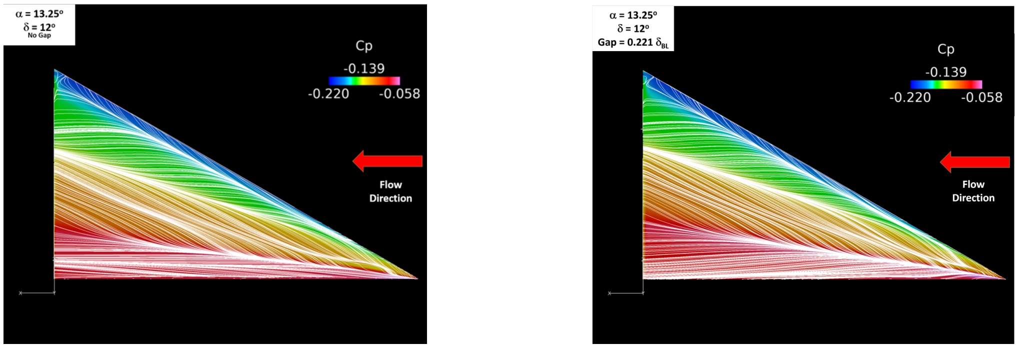

(a) No gap.

(b) Gap $= 0.221\delta_{BL}$.

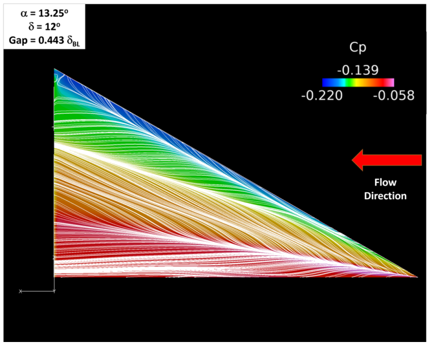

(c) Gap $= 0.443\delta_{BL}$.

Figure 4.37: Leeward side of fin colored by pressure coefficient; $\delta = 12\,\text{deg}$.

shock; separation bubble with no shock; classical vortex; and vortex with shock. The expected regime can be computed from the Mach number

$$M_N = M_\infty \left(1 - \sin^2\Lambda \cos^2\alpha\right)^{\frac{1}{2}} \tag{4.9}$$

and angle of attack normal to the leading edge

$$\alpha_N = \tan^{-1}\left(\frac{\tan\alpha}{\cos\Lambda}\right), \tag{4.10}$$

where Λ is the leading edge sweep and α is the angle of attack.

4.4.3 Experimental Setups

Two sets of experimental results are used for comparison. The first, by Miller [26], are wind tunnel results from the NASA Langley Unitary Plan Wind Tunnel

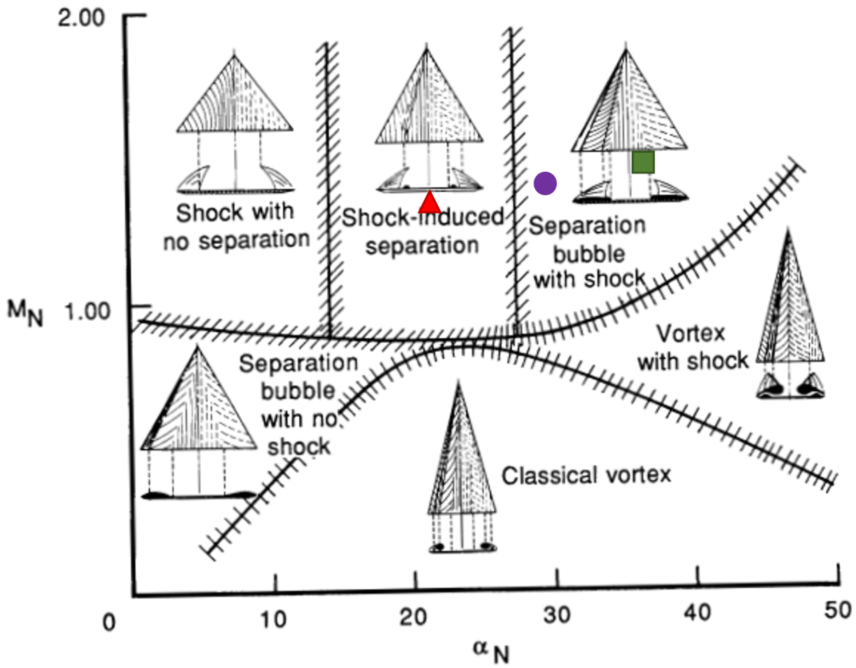

Figure 4.38: Leeward side flow separation classification [24, 25]. Points from current study; $\delta = 12deg$ (red triangle); $\delta = 16deg$ (purple circle); $\delta = 20deg$ (green square)

for a delta wing planform. In this case, Miller looked at four different leading edge sweep angles at five different Mach numbers. Transition strips were placed 0.2 in downstream of the leading edge on the upper surface of each wing to ensure flow transition to turbulent. Pressure orifices were located on the top, in a row an inch upstream of the wing trailing edge. The four different planforms are shown in Fig. 4.39, where the wing with a leading edge sweep of 60 deg was used for comparison as highlighted by the blue box. The delta wings were placed on a dog-leg strut, as shown in Fig. 4.40 and swept from 0 to 20 deg angle of attack.

Vapor screens were used to visualize the flow, and will be utilized for comparison to CFD results. Vapor screens are a flow visualization technique that utilizes water vapor for the visualization of vortices, boundary layers, and shock waves [126].

Condensation causes shock waves to be visible. Unless the flow is seeded, vortices and boundary layers show up dark because they are devoid of scattering particles.

Miller did not run at Mach 2.5, however he did perform wind tunnel runs at Mach 2.4 which is close enough for qualitative comparisons. The Reynolds number at this condition was $6.58 \times 10^6/m$.

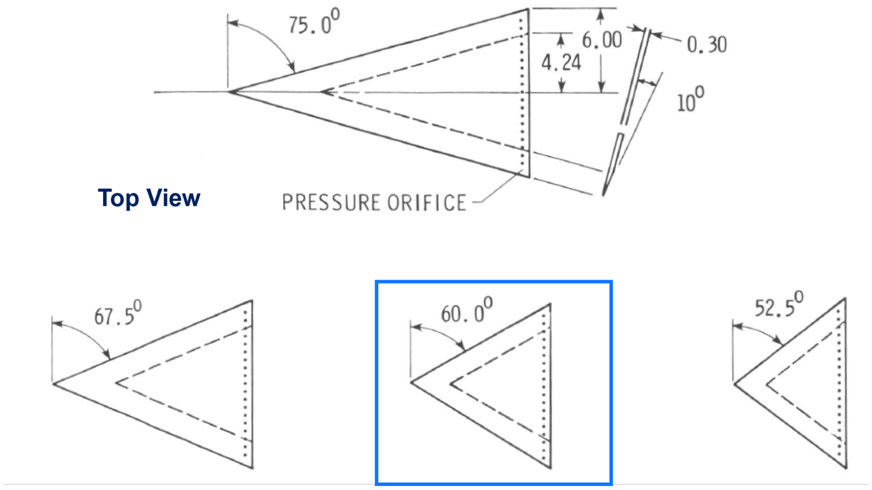

Figure 4.39: Delta wing planform of Miller [26]

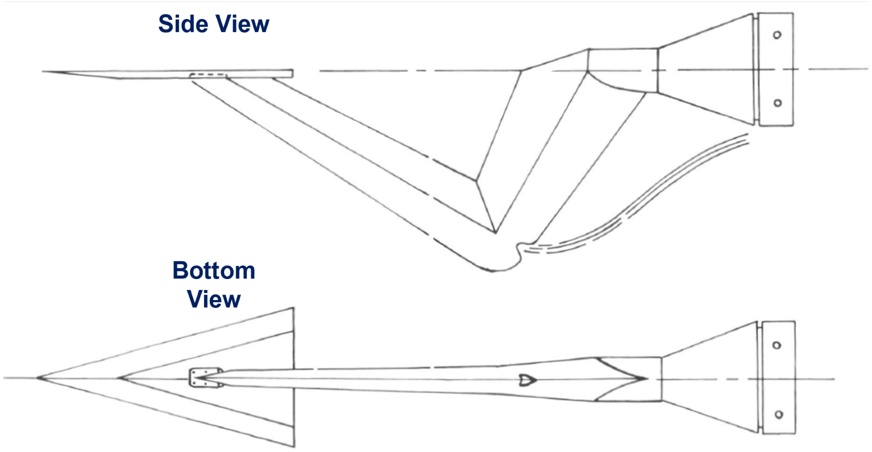

Figure 4.40: Experimental setup of Miller [26]

Since Miller's results are for a delta wing, it was also desire to compare the CFD to wind tunnel results for the leeside of a fin. Michael [34] performed experiments on a fin with a leading edge sweep of 58.75 deg (in addition to five other leading edge sweep angles), as shown in Fig. 4.41. The fin was placed in the 9- by 6-inch Langley gas dynamics laboratory wind tunnel illustrated in Fig. 4.42, which was run at Mach 1.9 and a Reynolds number of $0.43 \times 10^6/m$.

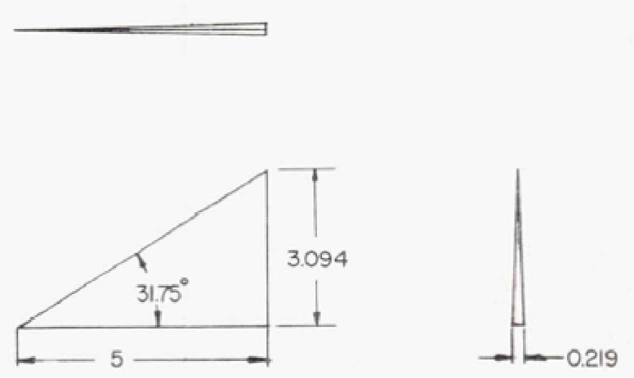

Figure 4.41: Fin planform of Michael [34]

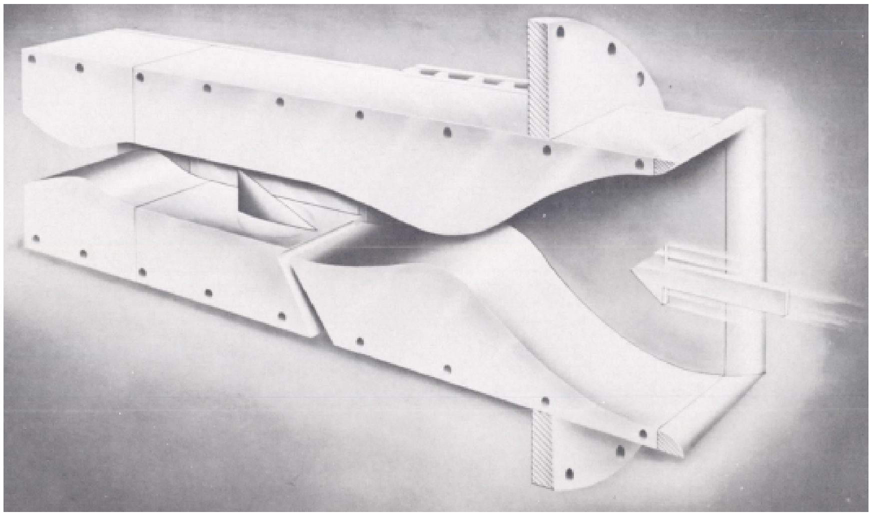

Figure 4.42: Experimental Setup of Michael [34]

Similar to Miller, Michael also placed pressure orifices on the surface, however these were placed at the half chord location instead of the trailing edge. These orifices were also used as a means to insert a surface flow visualization fluid onto the fin surface. The vapor screen flow visual technique was utilized by Michael in this study, and an illustration of the setup is shown in Fig. 4.43. As the camera was placed outside of the tunnel and angled 60 deg from to the tunnel window, the true distance of the vortex cores above the fin surface do not appear in their correct positions in the images [34]. According to Michael however, the actual distance above the fin surface is on the order of twice the observed distance in the photograph [34]. The spanwise position of the vortex does appear in the correctly in the images.

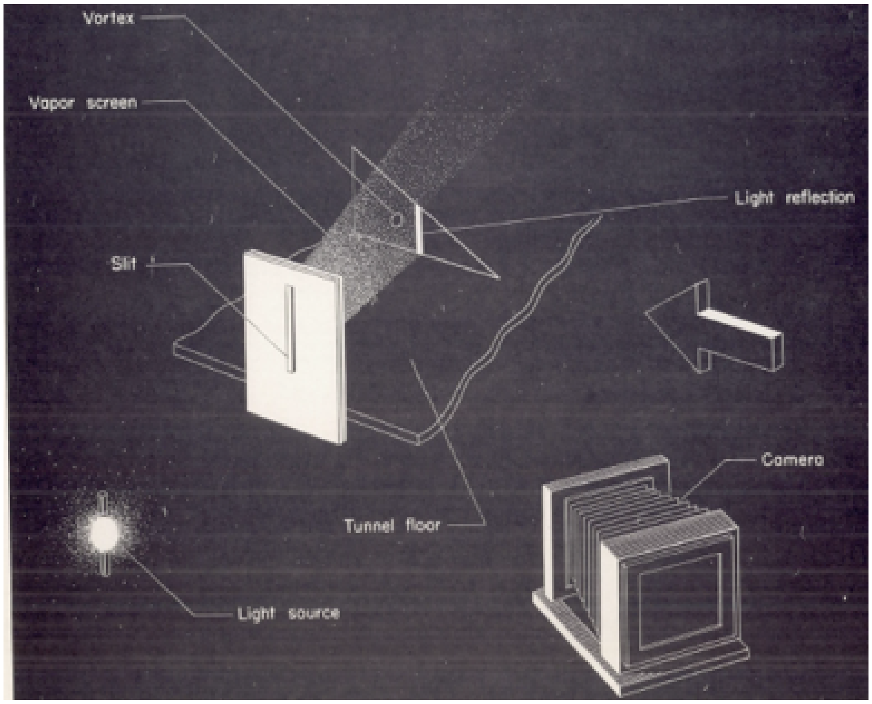

Figure 4.43: Vapor screen setup of Michael [34]

4.4.4 Comparisons between CFD and Experiments

The angles for comparison are plotted in Fig. 4.38, with a deflection of 12 deg shown by the red triangle, 16 deg indicated by the purple circle, and a deflection of 20 deg as indicated by the green square. According to the classification, all deflections will result in separation on the leeward side. A delta wing with a 12 deg deflection will exhibit shock-induced separation, while deflections of 16 and 20 degs will have a separation bubble with a shock. A detailed sketch of surface flow visualizations from [26] for the two flow regimes under consideration is shown in Fig. 4.44. Expected oil flow patterns on the leeward surface, vapor screen images, and pressure coefficient distributions are presented in the figures.

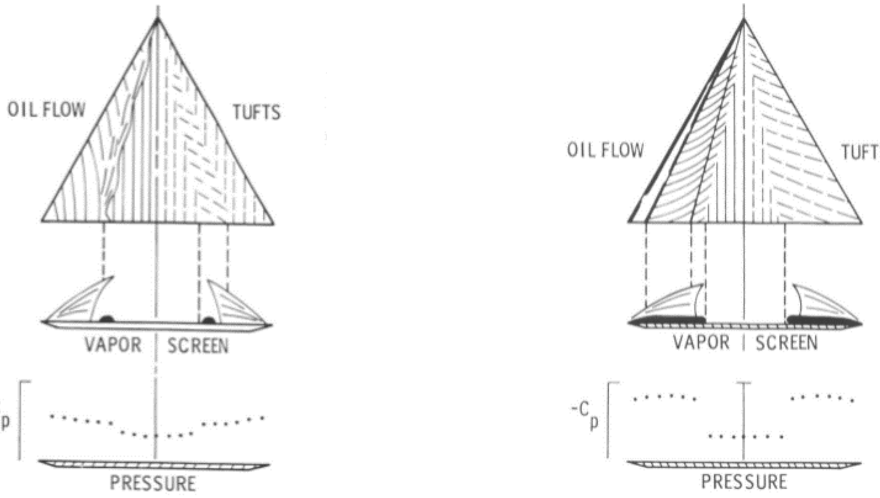

(a) Separation induced by shock (b) Separation bubble with shock

Figure 4.44: Flow feature comparison of two separation types on leeside of delta wing. From [26].

4.4.4.1 Surface Streamline Comparison

Figures 4.45 - 4.47 compare surface streamlines obtained from CFD to surface flow results experimentally obtained at Mach 1.9 by Michael [34] for deflection angles of 12, 16, and 20 deg. Even with the differences in fin geometry and freestream Mach number, similar flow patterns are observed in Fig. 4.45 with the fins deflected 12 deg. Each exhibit a separation line in the outer third of the fin, and display a small separation region at the fin tip. Surface flow patterns continue to match fairly well for a deflection of 16 deg, as seen in Fig. 4.46. As with the 12 deg deflection, there is a separation line present in both results on the upper third of the fin. The separation region at the fin tip is also present, but has increased in size with the increase in deflection. Figure 4.47 shows the comparisons between results at 20 deg. The separation line in the upper third of the fin has disappeared, but the flow separation region at the fin tip has significantly grown for each of the fins.

4.4.4.2 Pressure Coefficient Comparison

In addition to surface flow visualization, Michael also measured the pressure coefficient in the spanwise direction. Results from Michael (red circles with spline fit for visual aid) are plotted against C_p results from the current study in 4.48 and results from Miller [26] (blue square with spline fit for visual aid). The black solid line plots results for a fin with no gap, the dotted purple line shows the fin with a gap of $0.221\delta_{BL}$, and the dashed green line plots C_p for a fin with a gap of $0.443\delta_{BL}$. As with the surface streamlines, the fin used by Michael had a leading edge sweep of 58.25 deg and was tested at $M = 1.9$. The slightly lower Mach number used by Michael accounts for the difference in C_p magnitude between the current results at $M = 2.5$ and results obtained by Miller at 2.5. Similar trends are seen between Michael's

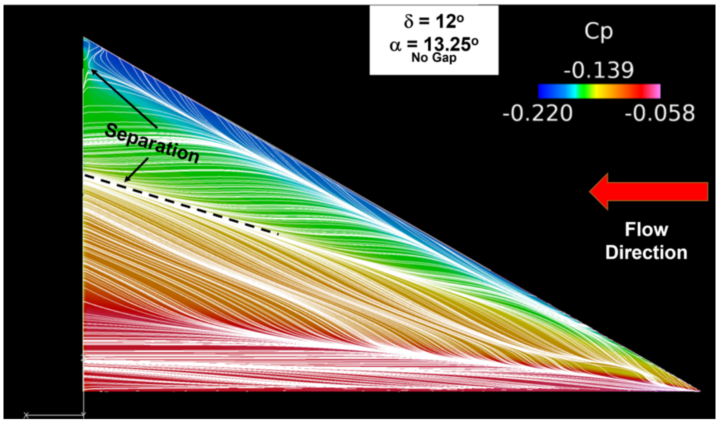

(a) Current Study

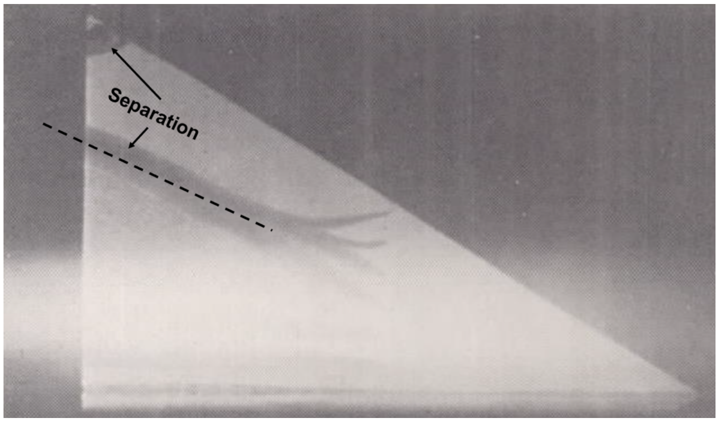

(b) Surface flow visualization results from [34], Mach 1.9, $\Lambda = 58.25$ deg.

Figure 4.45: Surface flow pattern comparisons. $\delta = 12$ deg

and CFD results for each deflection angle. At each deflection angle, the gap shifts the location of the vortex outboard, as seen by the location where the C_p dips around $z/b = 0.2$. As Miller used a full delta wing, and not half a delta wing attached to a flat plat, there is no C_p dip in his results. This suggests that the flat plate affects the flow field resulting in a change in surface pressure on the fin or delta wing. As revealed later, this dip is due to a strong vortical flow.

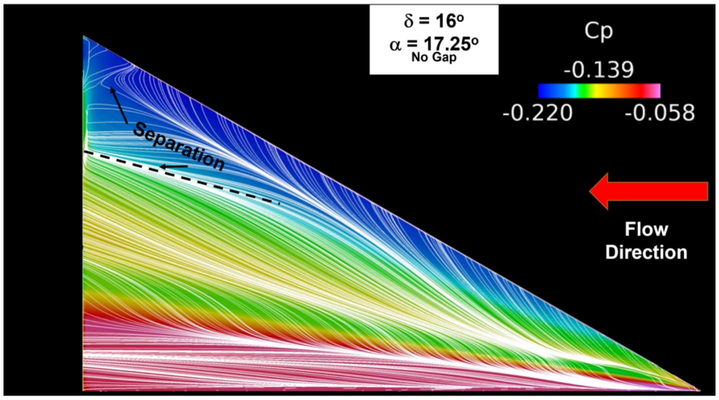

(a) Current Study

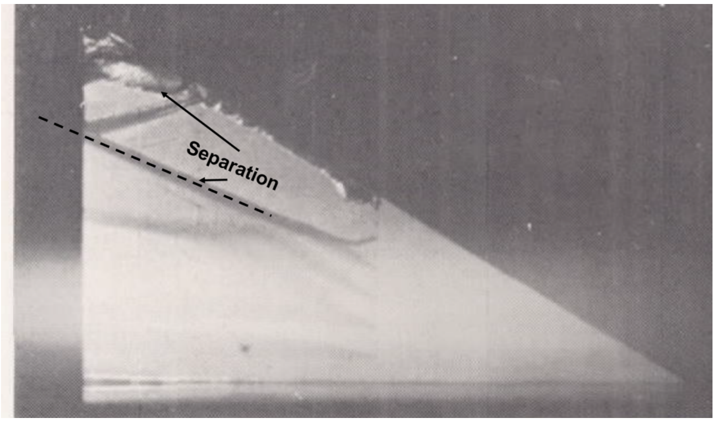

(b) Surface flow visualization results from [34], Mach 1.9, $\Lambda = 58.25$ deg.

Figure 4.46: Surface flow pattern comparisons. $\delta = 16$ deg

4.4.4.3 Vapor Screen Comparison

The quality of available vapor screen images from [34] was insufficient for detailed comparisons. Instead, vapor screen images obtained by Miller [26] are used for comparison. Figure 4.49 compares the delta wing vapor screen image on the left, to density contours from CFD on the right for a fin at 12 deg. In the figure flow is into the page, and a vortex is seen just above the center of the fin with a lambda shock above it. The central foot of the lambda does not extend to the vortex in both the experiment and CFD results. Additionally, the vortex seems to be confined to the

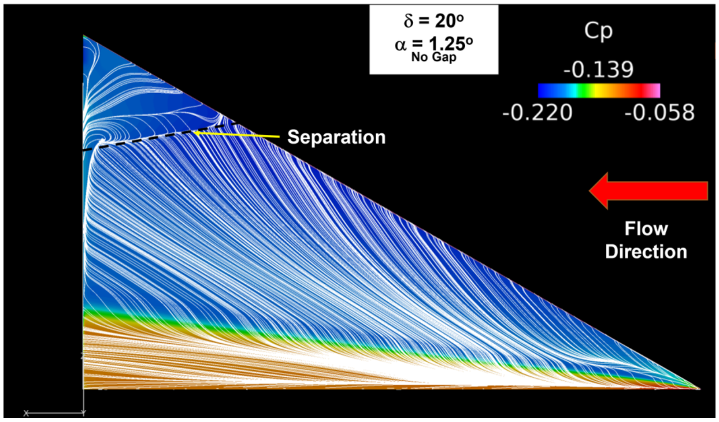

(a) Current Study

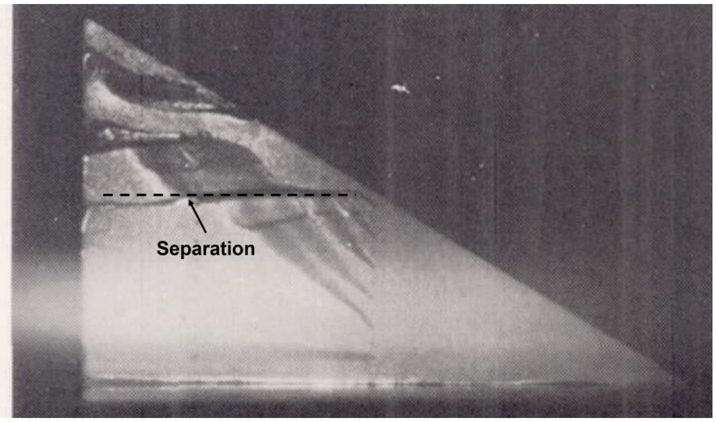

(b) Surface flow visualization results from [34], Mach 1.9, $\Lambda = 58.25$ deg.

Figure 4.47: Surface flow pattern comparisons. $\delta = 20$ deg

middle of the fin, especially in the wind tunnel results on the left. Based on both the regimes defined by Stanbrook and the observed flow features, a shock-induced separation is observed in both cases.

Comparisons for a fin deflection of 16 deg is presented in Fig. 4.50. Similar flow features are observed in both experimental and CFD results, however the vortex is now of sufficient strength to cause crossflow from the center of the fin towards the fin tip along the fin surface causing a separation bubble. The central lambda foot

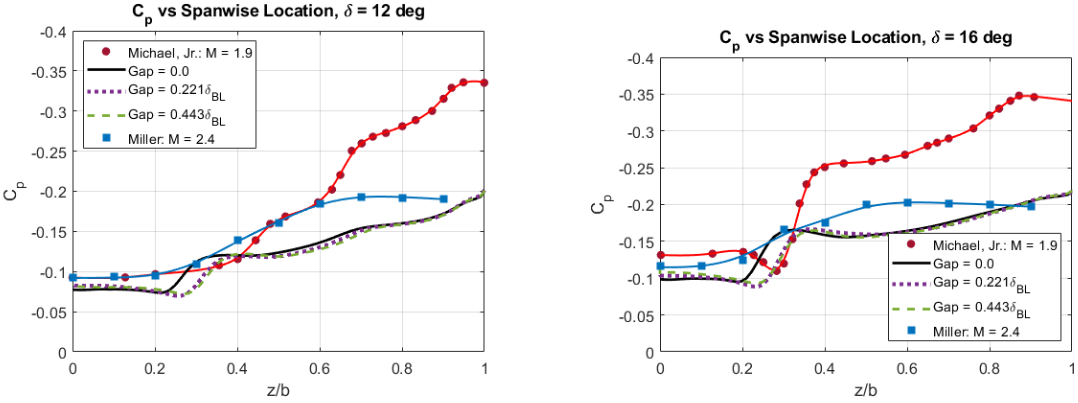

(a) $\delta = 12$ deg

(b) $\delta = 16$ deg

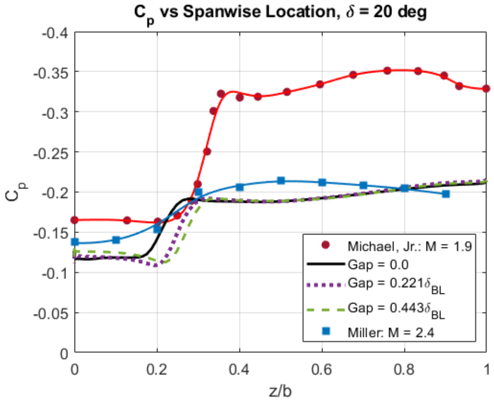

(c) $\delta = 20$ deg

Figure 4.48: Pressure coefficient versus spanwise location on fin leeward side for different gaps. Mach 1.9 from [34] (circles and solid red); No gap (solid black); Gap $= 0.221\delta_{BL}$ (dotted purple); Gap $= 0.443\delta_{BL}$ (dashed green); $M = 2.4$ from [26] (squares and solid blue)

extends closer to the vortex core as well. These results point to bubble separation with a shock.

At a deflection of 20 deg, as shown in Fig. 4.51, both the experimental results and CFD show the vortex strengthen further, increasing the size of the separation bubble. Significant crossflow from the center of the fin towards the fin tip along the fin surface occurs and the central lambda foot extends even closer to the vortex. From Fig. 4.38, the flow is classified as bubble separation with a shock.

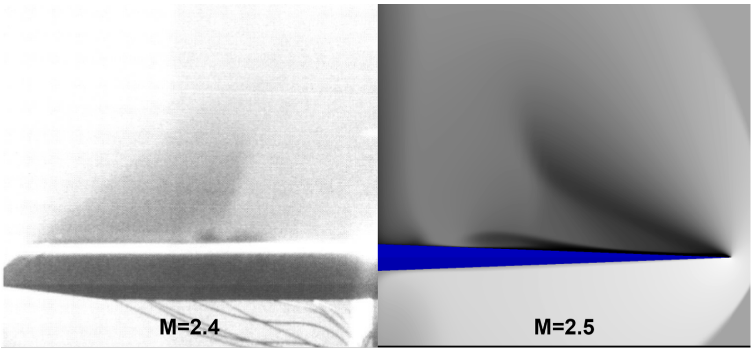

Figure 4.49: Vapor screen results by Miller [26] on left. Density contours from CFD on right. Flow into the page. $\delta = 12$ deg

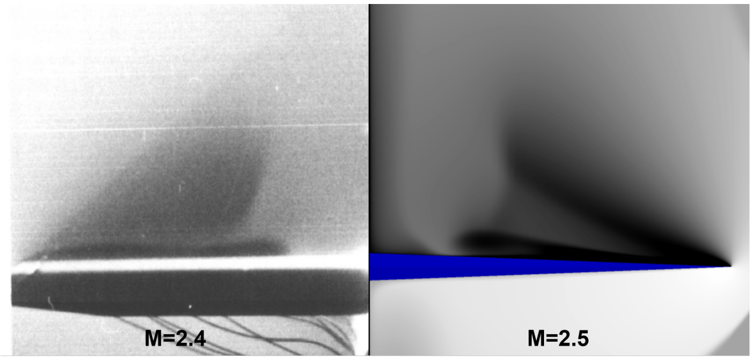

Figure 4.50: Vapor screen results by Miller [26] on left. Density contours from CFD on right. Flow into the page. $\delta = 16$ deg

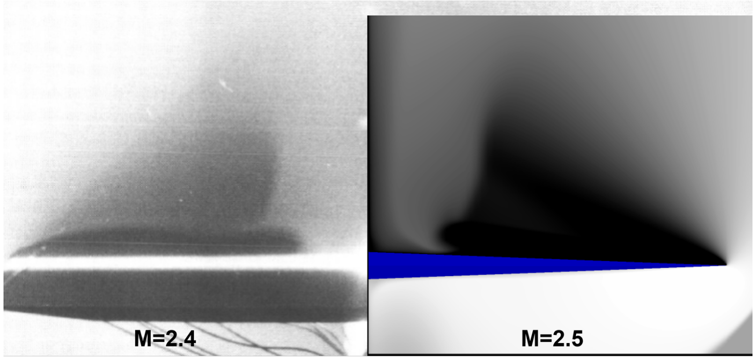

Figure 4.51: Vapor screen results by Miller [26] on left. Density contours from CFD on right. Flow into the page. $\delta = 20$ deg

An interesting feature seen in all the CFD results is the tendency for the central lambda foot to angle out towards the fin tip leaving a concave shape facing the centerline. A similar concave lambda shock was observed in results by Michael for a fin mounted on a flat plate deflected 20 degrees, as seen in 4.52. This is in contrast to the experimental results obtained by Miller, which displayed a convex curve facing the centerline. The concave shape of the lambda shock occurs when a fin is mounted on a flat plate, as opposed to the experiment by Miller which used a full delta wing. As the plate is perpendicular to the fin, flow is confined, causing a local shock-shock interference.

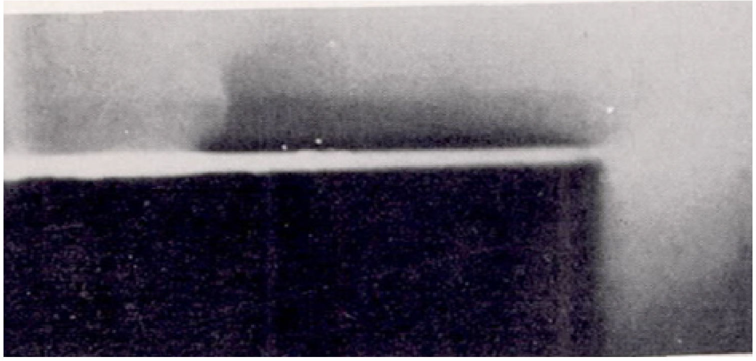

Figure 4.52: Vapor screen results by Michael [34]. Flow into the page. $\delta = 20$ deg, $M = 1.9$, $\Lambda = 58.25$ deg.

The effect on the vortex of adding a gap between the plate and the fin is shown in Fig. 4.53. Both gap heights appear to minimally affect the flow on the surface of the fin. However, flow through the gap adds vortices. An in-depth analysis of vortices due to the gaps was given in the preceding section 4.4.1.

4.5 Fin Effectiveness

So far, comparisons of important SBLI angles were made between the CFD results of the current study and semi-empirical relations. The determination of incipient separation was made for a swept fin and tested against the Korkegi criterion.

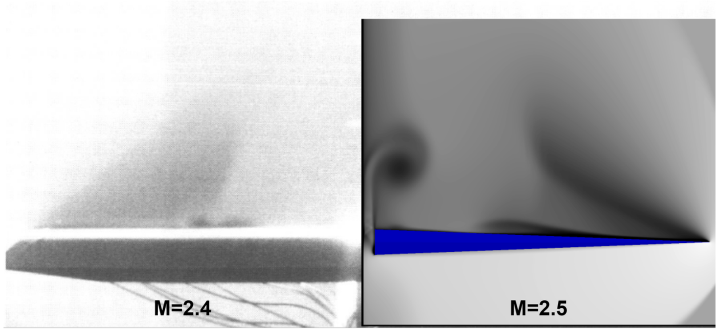

(a) Gap = $0.221\delta_{BL}$.

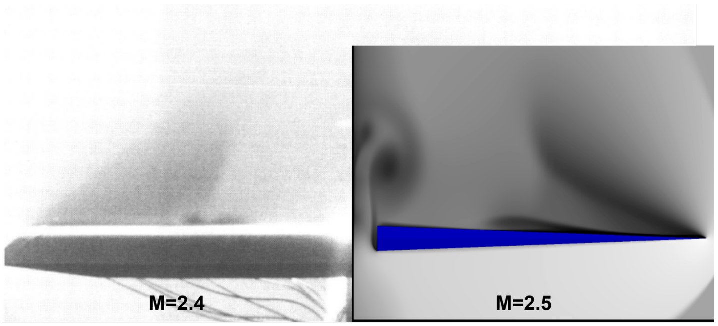

(b) Gap = $0.443\delta_{BL}$.

Figure 4.53: Vapor screen results by Miller [26] on left. Density contours from CFD on right. Flow into the page. $\delta = 12$ deg

Following this, an flow field analysis was performed for the leeside of the fin which uncovered an additional vortex. Just prior to this section, comparisons between CFD and wind tunnel results were made, which showed excellent qualitative agreement. We close the chapter by analyzing the fin effectiveness, or the ability of the fin to generate normal force. Comparisons are made to experimental results of instrumented fins on both flat plates and axisymmetric bodies performed by both Allen [60] and Dahlke and Pettis [61].

4.5.1 Experimental Setup

Allen [60] mounted fins to both an axisymmetric body as well as a flat plate and the fin normal force, hinge moment, and bending moment were measured. He tested several different fin geometries, and the closest geometry to the current study is Fin 8. As shown in Fig. 4.54a, Allen's fin had a sharp leading edge, with a modified double wedge section. The leading and trailing half angles were both 3.1 deg. With a span of 0.0762 m and chord of 0.1524 m, the leading edge sweep was 63.4 deg. A schematic of the fin used by Allen is given in Fig. 4.54a. The fin when mounted above the flat plate had a gap of 1.27 mm.

Dahlke and Pettis [61] examined the effect of a fin gap on the fin's aerodynamic performance when mounted above an axisymmetric body. Due to the nature of the study, only fin normal force was measured by Dahlke and only for a fin on an axisymmetric body. The fin in this study was a delta planform which used a double wedge section. It had a span of 0.0133 m and chord of 0.0355 m resulting in a leading edge sweep of 69.4 deg. Figure 4.54b gives the schematic for the delta fin. The gap heights used by Dahlke are provided in Table 4.2 and range from no gap, up to almost 5.6 mm.

Table 4.2: Gap measurements

Gap Heights (mm)		
Allen [60]	Dahlke [61]	Otten [22]
1.27	0.0 1.676 3.352 5.588	0.0 1.27 2.66

The sign convention for fin normal force, root bending moment, and hinge moment is given in Fig. 4.55. Fin normal force is defined as perpendicular to the fin centerline, and rotates with the fin such that it is always perpendicular to the fin. Positive hinge moment HM is leading edge up, and rotates about the hinge line

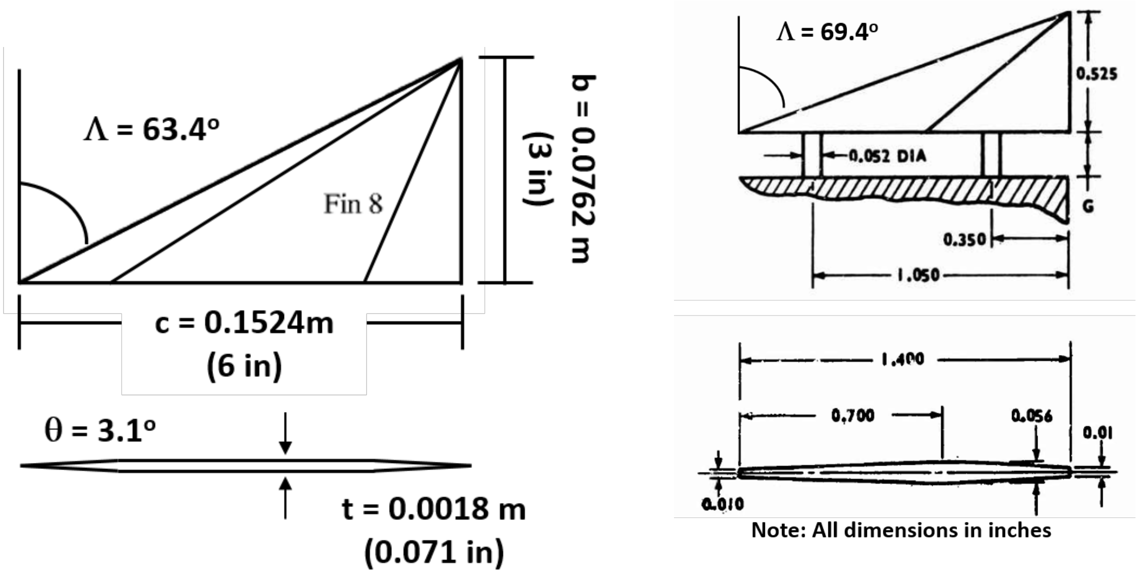

(a) Fin used by Allen [60].

(b) Fin used by Dahlke and Pettis [61]. All units in inches.

Figure 4.54: Schematics for fins used by Allen [60] and Dahlke [61]

located at 60% of the fin root chord. The hinge moment is depicted in Fig. 4.55a. The root bending moment illustrated in Fig. 4.55b is positive if the tip of the fin moves up (towards positive fin normal force) and rotates around the fin root.

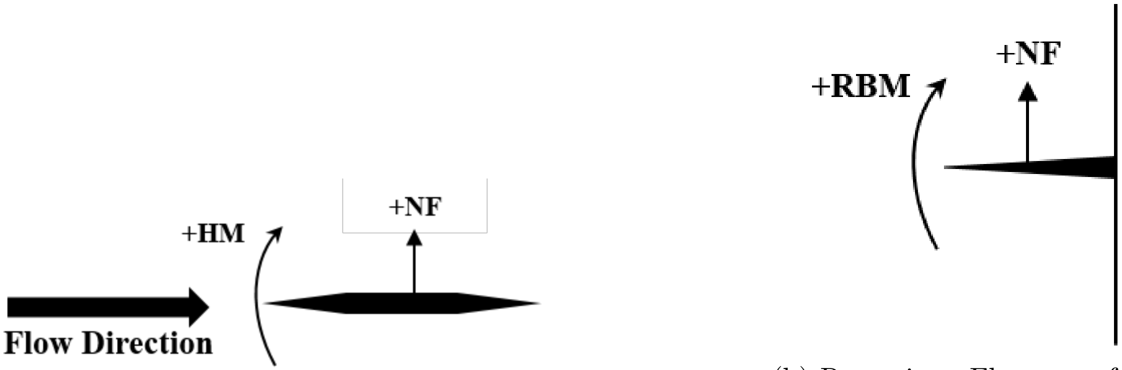

(a) Top view.

(b) Rear view. Flow out of page.

Figure 4.55: Sign convention for normal force, hinge moment, and root bending moment, modified from Allen [60].

4.5.2 Fin Loads vs Deflection Angle

4.5.2.1 Single Gap Height

Fin loads measured by Allen, and Dahlke are compared to results obtained in this study in Fig. 4.56. In all the plots, the diamonds are from the current study, the squares are Allen's data, and the circles on the fin normal force plot are from Dahlke. As previously stated, Dahlke only measured the fin normal force, and not root bending nor hinge moments, so only Fig. 4.56c compares his data to the current study and to Allen's. Additionally, Dahlke only deflected the fin to a maximum of 10 deg. Since the current study places the fin above a flat plate, only the results from Allen for the fin mounted above the flat plate are shown, and not the results for the fin above the axisymmetric body.

It should be noted that the Mach number of the current study and that of Dahlke is 2.5 while that of Allen is Mach 2.3. Given the slight differences in fin geometry and Mach numbers, the general agreement of the data is good. Figure 4.56a shows the comparison of the fin root bending moment coefficient, where the axis of rotation is the fin root. Given the geometry and Mach differences, the two data sets show good agreement through the deflection range, with the disagreement increasing with increasing deflection angle. It can be noted that Allen's data for a deflection of 8 deg appears to be anomalous.

The hinge moment coefficient is compared in Fig. 4.56b, where the moment reference center is 60 percent of the fin root chord. Allen's and the current data agree well. Similar to the root bending moment, the difference between the results increases with increasing deflection angle. Most likely this is due to a combination of differences in the fin geometry and Mach number. As before, the results for a deflection of 8 deg appears to be anomalous.

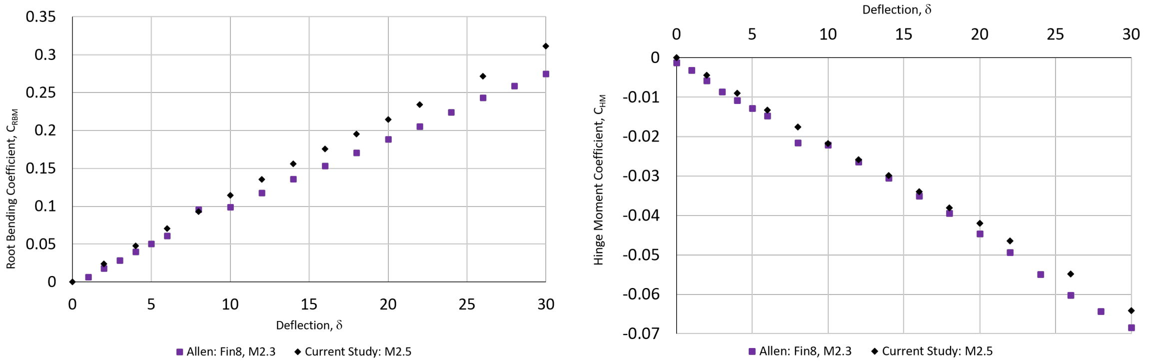

(a) Change in fin bending moment coefficient with deflection.

(b) Change in fin hinge moment coefficient with deflection, $MRC = 0.6c$.

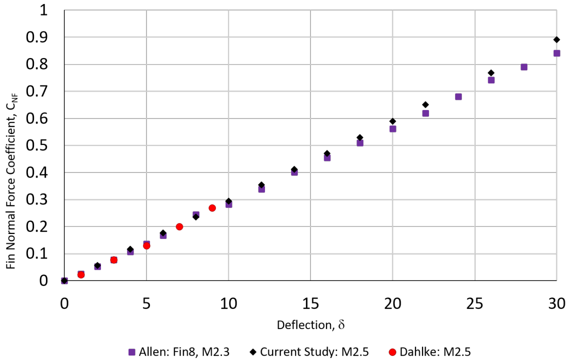

(c) Change in fin normal force coefficient with deflection.

Figure 4.56: Force and moment coefficients. Diamonds: current study, fin on plate, gap = 1.27 mm, Mach 2.5; squares: Fin 8 on a flat plate, Mach 2.3, gap = 1.27 mm by Allen [60]; circles: Dahlke [61], fin on axisymmetric body, Mach 2.5, gap = 1.676 mm.

Finally the fin normal force coefficient is compared in Fig. 4.56c, with the results from Dahlke added. As in the previous results, good agreement is seen with measured data from Allen for deflections under 10 deg. The results are also in line with those obtained by Dahlke for fins on an axisymmetric body with a gap of 1.676 mm.

4.5.2.2 Gap Height Comparison

Following fin load comparisons for fins at the same or similar gap heights, the affect of gap height on the fin loads is desired. For this comparison, the nondimensional gap factor defined as the ratio of the gap height to the fin span

$$f = \frac{g}{g+b} \tag{4.11}$$

is introduced, where g is the gap height and b is the fin span. The gap factors for each of the cases is provided in Table 4.3. Dahlke has the largest values of f due to the significantly smaller span but larger gaps, compared to Allen's and the current study.

Table 4.3: Gap factors for all gap heights analyzed

Allen [60]	Dahlke [61]	Otten [22]
	0.0	0.0
0.016	0.112	0.017
	0.201	0.035
	0.295	

Figure 4.57 shows the effect of the gap below the fin on the normal force and hinge and bending moments. The present results confirmed those of Allen who found that the gap effect for fin loads, when a fin is placed on a flat plate, is negligible [60]. The most noticeable difference occurs in the hinge moment at high deflection angles, Fig. 4.57b, where a reduction in hinge moment occurs as the gap height increases. Otherwise, the gap height has a minimal effect for deflections less than 15 deg.

Further comparisons to Dahlke are made in Fig. 4.58, where the fin normal force slope and axial force for zero deflection are plotted versus gap factor. In Fig. 4.58a, the solid line with diamonds is the current study, the dashed line is results from

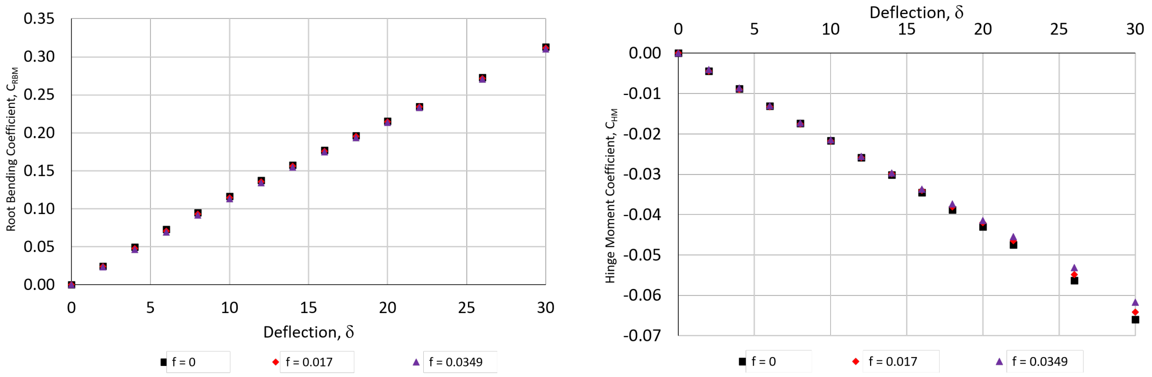

(a) Change in fin bending moment coefficient with deflection.

(b) Change in fin hinge moment coefficient with deflection, $MRC = 0.6c$.

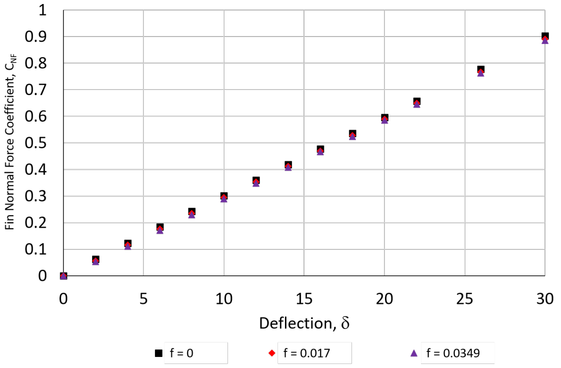

(c) Change in fin normal force coefficient with deflection.

Figure 4.57: Effect of gap on force and moment. Square: no gap; diamond: $f = 0.017$; triangle: $f = 0.0349$.

Dahlke, and the square and triangle are Allen's results for the fin above a flat plate and axisymmetric body respectively. A larger normal force slope indicates greater fin effectiveness. It is seen that as the gap factor increases, a reduction in normal force slope occurs for both the current results and the results measured by Dahlke. However, the reduction in fin normal force slope is greater when the fin is over a plate as compared to when it is over an axisymmetric body. By comparing the results from Allen, it is also observed that the effect of placing the fin on an axisymmetric body is to increase the fin normal force slope for a given gap factor.

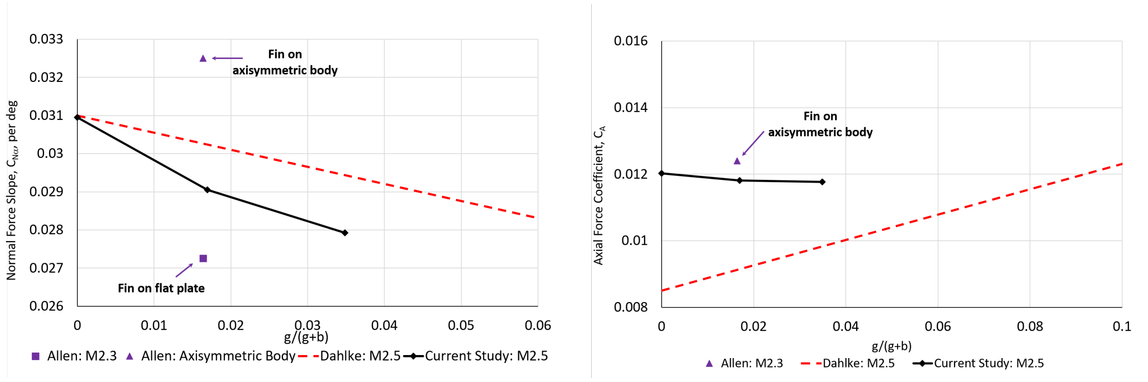

(a) Change fin normal force slope with gap factor.

(b) Change in zero angle of attack axial force with gap factor.

Figure 4.58: Effect of gap on normal force slope and zero angle of attack axial force. Solid line (for visual aid only) with diamond: current study; dashed: Dahlke [61]; square: Allen [60], fin on flat plate; triangle: Allen [60], fin on axisymmetric body.

Zero deflection axial force comparisons are made in Fig. 4.58b. As Allen did not provide fin axial force values, the axial force was determined by taking the difference between the axisymmetric body alone with the results of the axisymmetric body with the fins and dividing by two, as there are two fins on the model. For the current results the zero angle of attack axial force does not have a strong dependance on the gap factor, but the results for a fin above an axisymmetric body shows a strong dependance on gap factor. Additionally the axial force for the fin on the axisymmetric body with no gap is significantly lower than the same gap factor for a fin over the flat plate. Most likely this is due to curvature effects from the flow around the cylinder.

In Fig. 4.59 the fin normal force versus angle of attack for the current results and those obtained by Dahlke are plotted. The lines with 'x' markers are for the current results, and the points are the results by Dahlke. Just as Fig. 4.58a showed that as the gap factor increases, the fins become less effective, so too it is seen by both the current results and those measured by Dahlke that as the gap factor increases

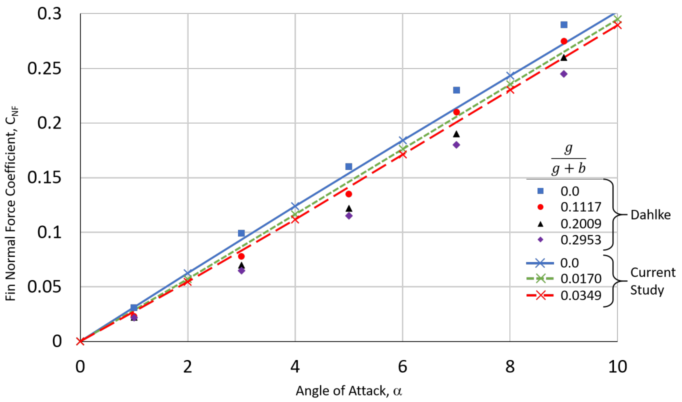

Figure 4.59: Effect of gap on fin normal force. Lines (for visual aid only): current study; solid line: no gap; dot-dashed: $f = 0.017$; dashed: $f = 0.0349$. Points: Results by Dahlke [61]; square: no gap; circle: $f = 0.1117$; triangle: $f = 0.2009$; diamond: $f = 0.2953$.

the normal force over the range of angles decreases. Large gaps affected normal force significantly according to Dahlke [61] factors.

4.6 Comparison to DES

For a moderate separation case of $\delta = 16$ deg, the RANS results were compared to results obtained with detached eddy simulation (DES) using CFD++. The Batten-Goldberg Hybrid RANS-LES model with a Smagorinsky coefficient of 0.05 was used. Wall-bounded compressibility corrections were enabled, just like the RANS runs. As discussed in Sec. 3.2.5, this formulation uses a RANS closure model in the near wall region for the attached turbulent boundary layer, but LES is utilized in cells where the large eddies can be resolved. A time step of 1×10^{-7} s, ensured a fluid element does not travel more than one cell per time step. Contours of normalized surface pressure are shown in Fig. 4.60 for both the RANS and DES results. In both cases, the inviscid shock (purple) line and upstream influence (blue) line were unaffected by the different solution method. However, the primary separation line was slightly different in each case. In Fig. 4.60a, the RANS results are shown with the primary separation line colored red. The DES results are in Fig. 4.60b, and green is used to show the primary separation line. The RANS case has a primary separation line angle of $\beta = 39\,\mathrm{deg}$ ($\beta - \delta = 23\,\mathrm{deg}$), while DES predicts $\beta = 37\,\mathrm{deg}$ ($\beta - \delta = 21\,\mathrm{deg}$).

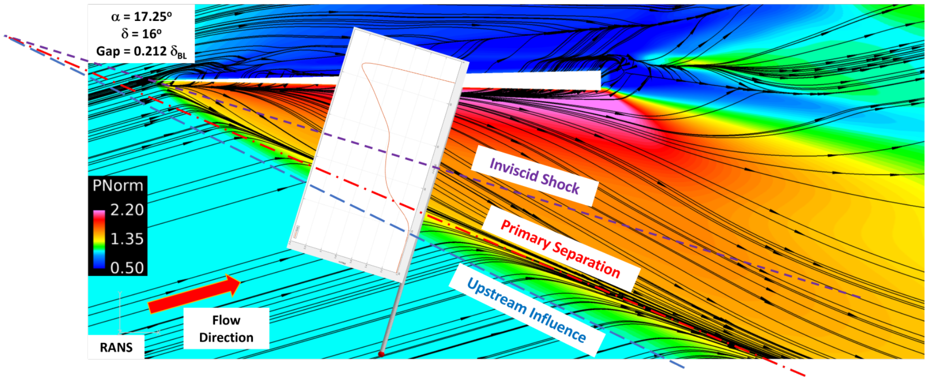

(a) RANS; primary separation (red) $= \beta - \delta = 23\,\mathrm{deg}$

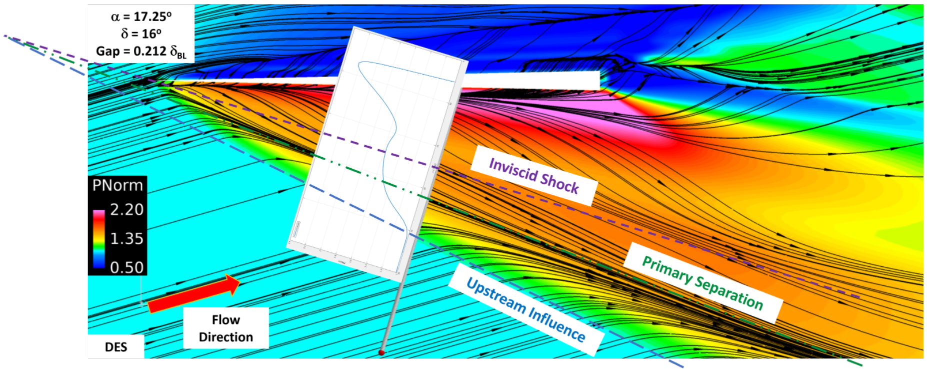

(b) DES; primary separation (green) $= \beta - \delta = 21\,\mathrm{deg}$

Figure 4.60: Surface streaklines on plate, $g/\delta_{BL} = 0.221$, $\alpha = 16\,\mathrm{deg}$, colored by normalized surface pressure; upstream influence (blue) and inviscid shock trace (purple).

Figure 4.61 plots normalized surface pressure vs β for the RANS result as well as DES results at times of 0.002425 and 0.0016 s (solid red and dashed green respectively). At both times steps, the DES results are almost identical to each other. The peak and plateau pressures between DES and RANS are similar, with RANS underpredicting compared to DES. All results show the same location for upstream influence and attachment. The major difference between DES and RANS is the dip in DES data around 15 deg $\beta - \delta$, which is not present in RANS data.

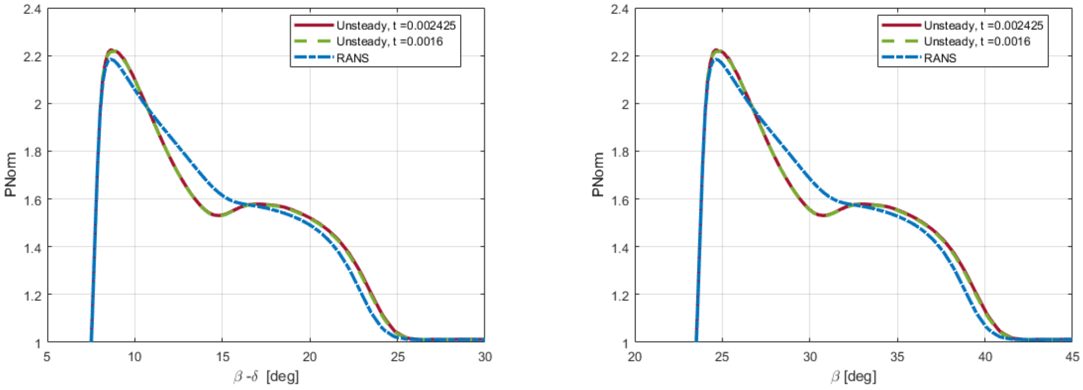

(a) PNorm vs $\beta - \delta$

(b) PNorm vs β

Figure 4.61: Normalized surface pressure plots; $g/\delta_{BL} = 0.221$, $\alpha = 16$ deg; RANS (dot-dashed blue), DES t=0.002425s (solid red), DES t=0.0016s (dashed green)

A close-up of surface pressure is shown in Fig. 4.62. In addition to the inviscid shock, primary separation, and upstream influence lines, a line indicating the leeside separation is also added. On the lee side, it can be seen that the separation line for DES has a larger angle and is further away from the fin compared to the RANS results. Since the peak pressure is higher for the DES runs, it takes longer to encounter a large enough adverse pressure gradient to cause separation on the leeside compared to RANS.

The normalized plateau pressure versus time, starting at $t = 0.0016$ s is shown in Fig. 4.63a. The black dashed line is the mean normalized plateau pressure from $t = 0.0016$ s onwards and the blue dot-dashed line is the RANS result. The computed error about the mean is shown with error bars on the unsteady results around the red solid line. As previously seen in Fig. 4.61, RANS slightly under predicts the

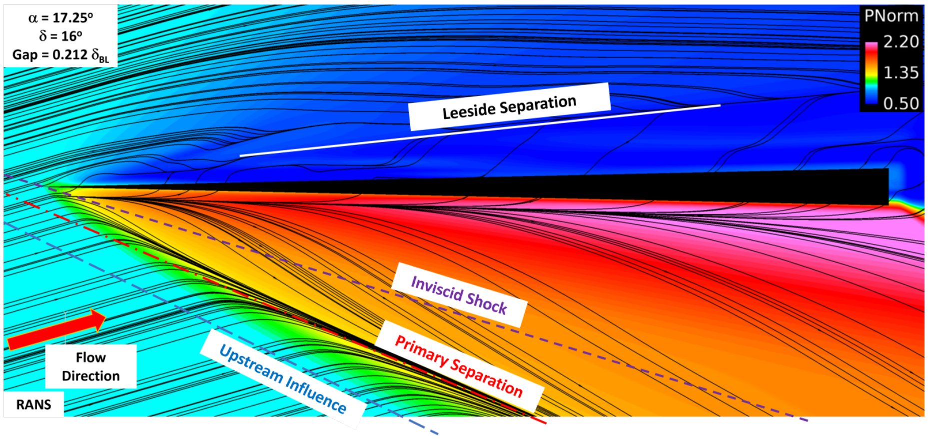

(a) RANS; primary separation (red) $= \beta - \delta = 23\,\text{deg}$

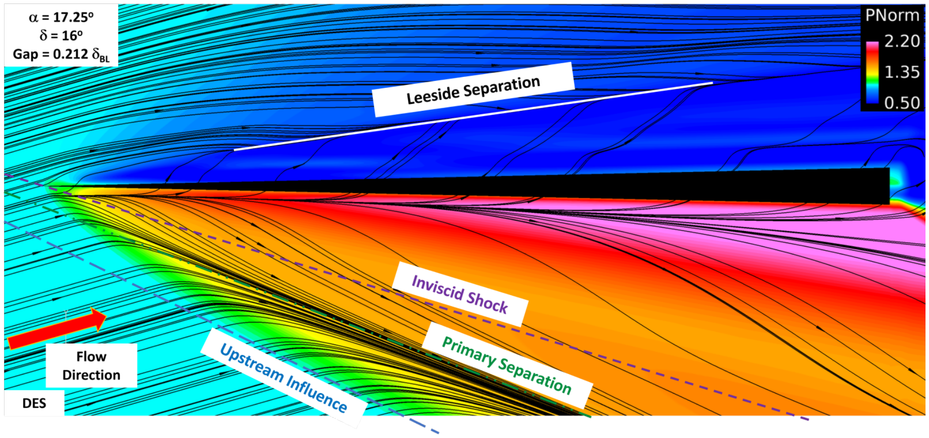

(b) DES; primary separation (green) $= \beta - \delta = 21\,\text{deg}$

Figure 4.62: Zoom in of surface streaklines on plate, $g/\delta_{BL} = 0.221$, $\alpha = 16\,\text{deg}$, colored by normalized surface pressure; upstream influence (long dashed blue), inviscid shock trace (short dashed purple), leeside separation (solid white).

plateau pressure compared to DES. While the DES results are time-dependent, they have reached a fairly steady result for the plateau pressure.

The normalized pressure from RANS data was subtracted from the normalized pressure obtained with DES. This is shown in Fig. 4.64 where red indicates larger RANS pressure and blue is larger DES pressure. Moving upstream to downstream, downstream of the upstream influence line the pressure is lower for the RANS solution compared to DES. This lower pressure allows for the flow to separate sooner

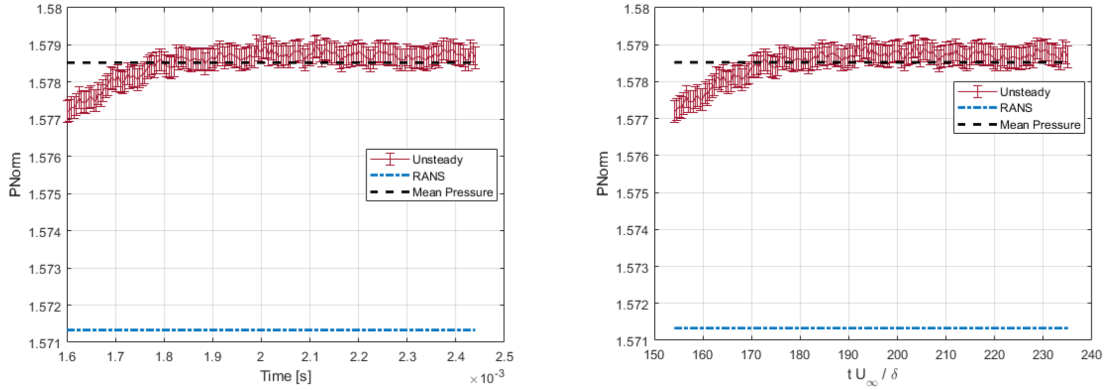

(a) Normalized plateau pressure vs time [s] (b) Normalized plateau pressure vs tU_∞/δ

Figure 4.63: Normalized plateau pressure vs time; Unsteady results (solid red), mean unsteady (black dashed), RANS (blue dot-dashed)

in the RANS solution compared to DES, resulting in a larger separation angle. As seen in Fig. 4.61, the RANS data does not capture the pressure dip following the inviscid shock. This can also be seen by the large area of higher RANS pressure in Fig. 4.64. Surface streaklines are added for both the RANS data (black) and DES data (magenta) in Fig. 4.64b streaklines are DES, black RANS. It is seen that the streamlines are identical until the upstream influence line is encountered. Also, the streamlines between the fin surface and inviscid shock are also almost identical, with both showing the same attachment line.

Velocity vectors on a plane normal to the fin are shown for the RANS and DES results in Fig. 4.65. Vectors are colored by Mach number. The separation (S1) and attachment (R1) locations are marked for each figure, showing the different separation locations, but same attachment point. Even though the separation locations are different in each case, the cores of the main separation vortex are separated by only 1 mm. However, the RANS vortex almost looks 'tilted' compared to the DES one. Shown in Fig. 4.65.

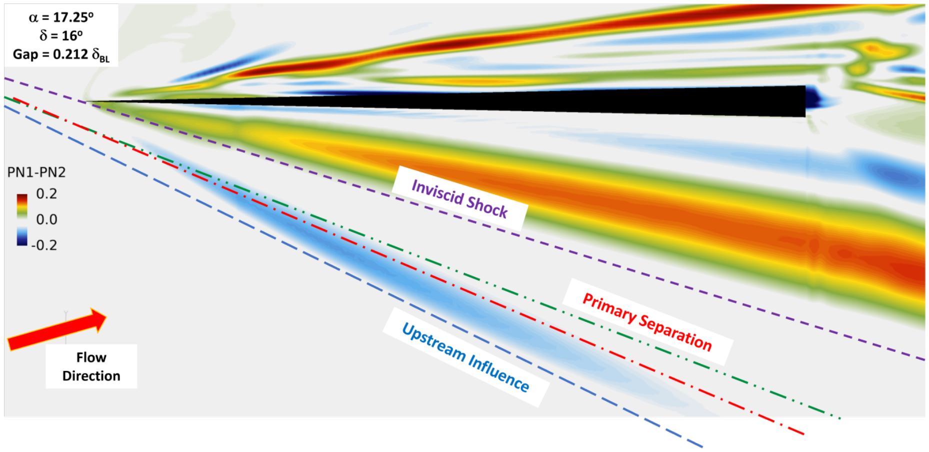

(a) Normalized pressure only

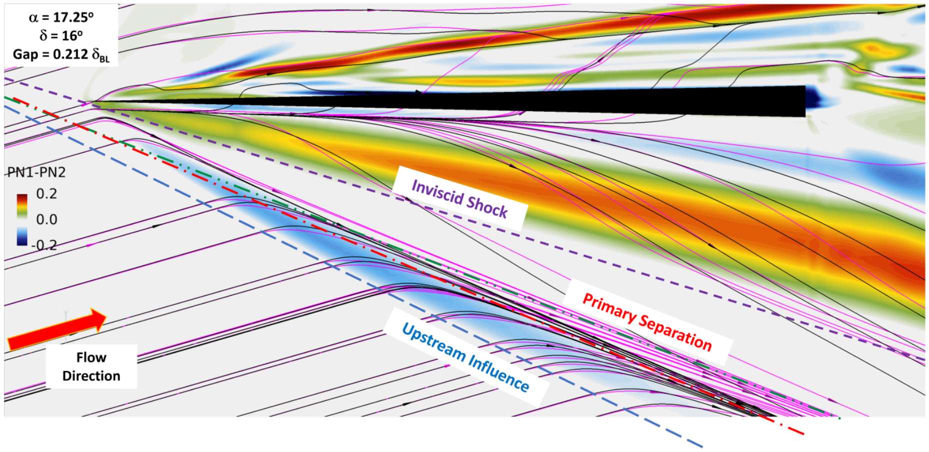

(b) RANS (black) and DES (magenta) surface streakline added

Figure 4.64: Δ Normalized surface pressure ($P_{RANS} - P_{DES}$); $g/\delta_{BL} = 0.221$, $\alpha = 16\,\text{deg}$; upstream influence (blue), primary separation (RANS: red, DES: green), and inviscid shock trace (purple).

To further aid in visualizing the vortices, streamwise vorticity is shown on a plane normal to the fin in Fig. 4.66. The plate is colored by normalized surface pressure, and surface streaklines are added as well. Both the RANS and DES results show similar vortical structures on both the leeward and windward sides of the fin. In the case of the RANS results, the core of the main separation vortex is elongated and connected to the boundary layer at the separation point. In the DES results of Fig. 4.66b a distinct main core exists, separated from the boundary layer.

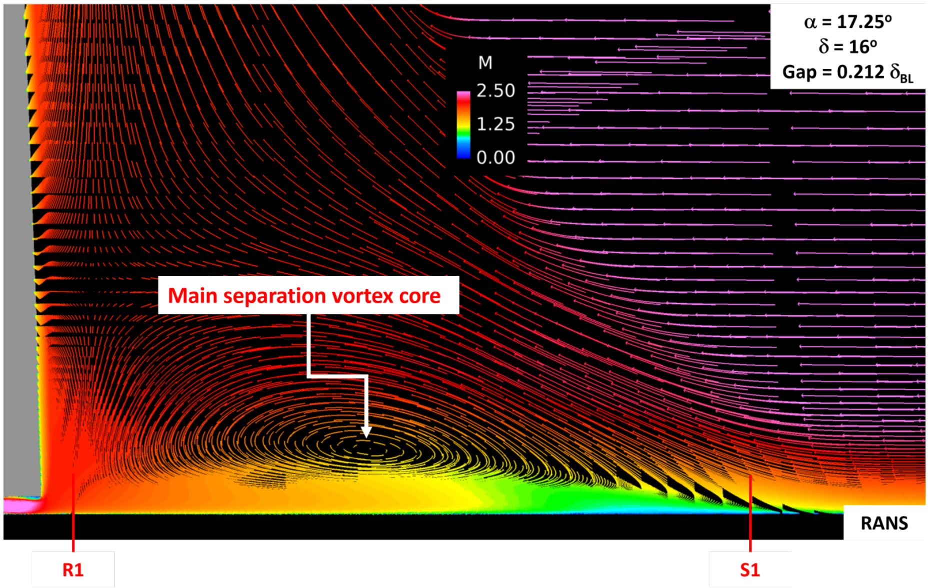

(a) RANS. Vortex core 26.60 mm outboard of and 3.43 mm above fin leading edge.

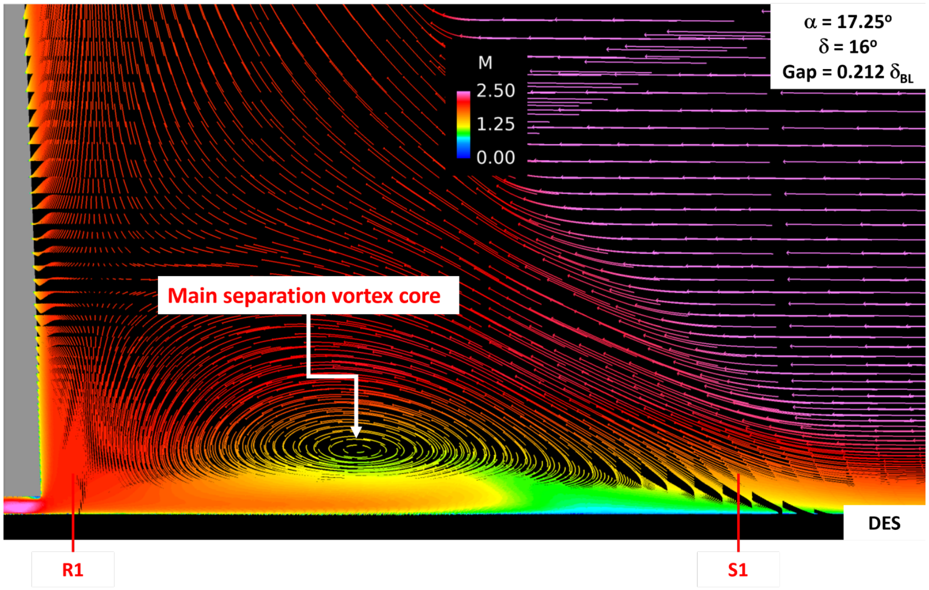

(b) DES. Vortex core 25.63 mm outboard of and 3.49 mm above fin leading edge.

Figure 4.65: Velocity vectors normal to fin. Colored by Mach number: $g/\delta_{BL} = 0.221$, $\alpha = 16\,\mathrm{deg}$

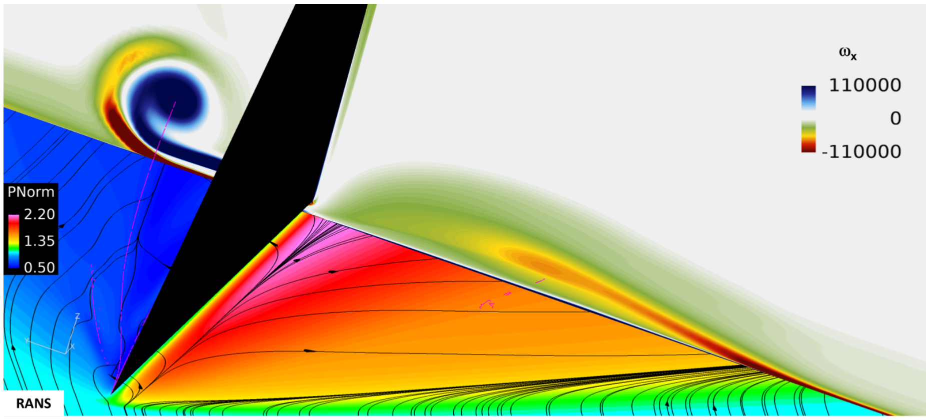

(a) RANS

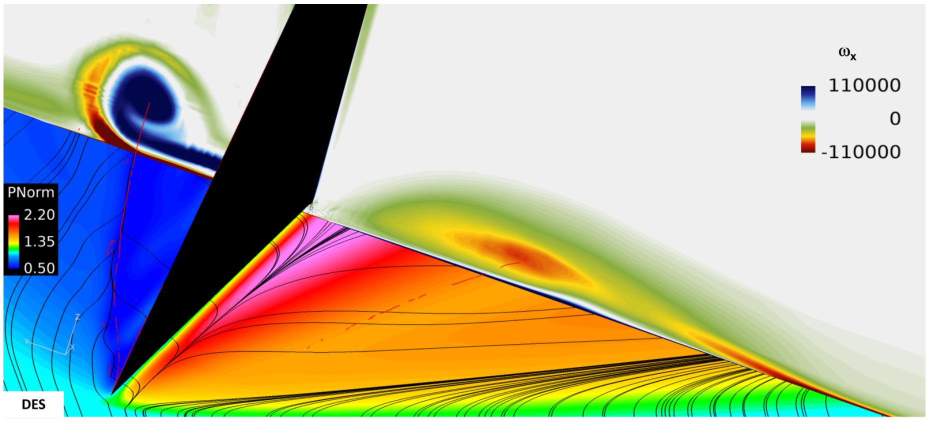

(b) DES

Figure 4.66: Streamwise vorticity ω_x, surface streaklines, and vortex core lines: $g/\delta_{BL} = 0.221$, $\alpha = 16\,\text{deg}$

The location of the dip in normalized pressure present in the DES results downstream of the inviscid shock corresponds to the location of the main separation vortex. This is because, in order to balance centrifugal acceleration, pressure is local minimum at the center of vortex [8], and increases as a function of distance from the vortex core squared. Assuming a Rankine vortex, which is a uniform distribution of vorticity inside a radius, the equation for the pressure distribution is

$$p - p_\infty = \frac{1}{2}\rho\Omega^2\left(r^2 - 2R_c^2\right) \tag{4.12}$$

where Ω is the angular velocity, r is the radius from the vortex center, and R_c is the radius of the vortex. The pressure at the center of the vortex reduces Eq. 4.12 to

$$p(0) - p_\infty = \rho (\Omega R_c)^2 . \tag{4.13}$$

Substituting vorticity $\omega = 2\Omega$ in for angular velocity results in

$$p(0) - p_\infty = \rho \left(\frac{\omega R_c}{2} \right)^2 . \tag{4.14}$$

Since pressure is a local minimum at the center of a vortex, it follows that $p(0)$ is less than the ambient pressure. Also, since the vortex is behind a shock, the ambient pressure is greater than the freestream pressure, as seen in Fig. 4.67. So, as $p(0)$ decreases, $p(0) - p_\infty$ increases. In that case, assuming density is constant, the vorticity ω must increase. Or as vorticity increases, the vortex pressure decreases. The circulation Γ will also increase with increasing vorticity and decreasing vortex core pressure from the relation $\Gamma = \omega A$, where A is the area of the vorticity tube. The lower pressure from the DES results, points to a higher vorticity and circulation, and therefore a stronger vortex. The lower pressure is observed in Figs. 4.64a, 4.61, and 4.67b. The increased vorticity is shown in Fig. 4.65b. All of which point to the DES results predicting a stronger vortex than the RANS results. As DES will be able to resolve the large eddies these results are not surprising. Moreover, the mean flow properties and separation characteristics are consistent between the two computational methods.

4.7 Ogive-Cylinder

Finally, we turn our attention to the fin on a body of revolution (BoR). In this section, the results for the body of revolution are compared to the flat plate results. Starting with Fig. 4.68 shows surface streaklines on a body of revolution

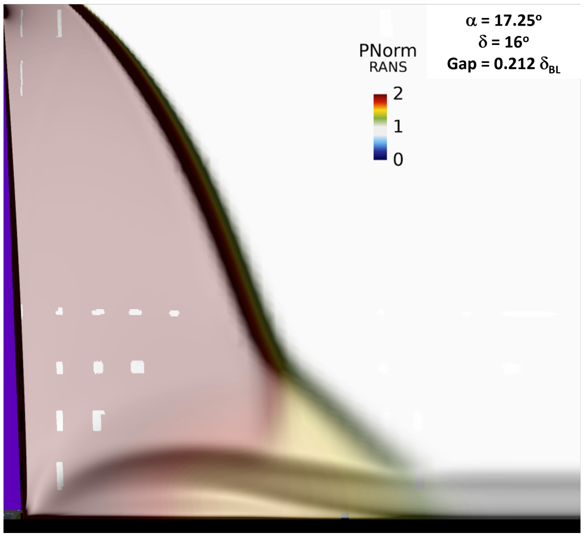

(a) RANS

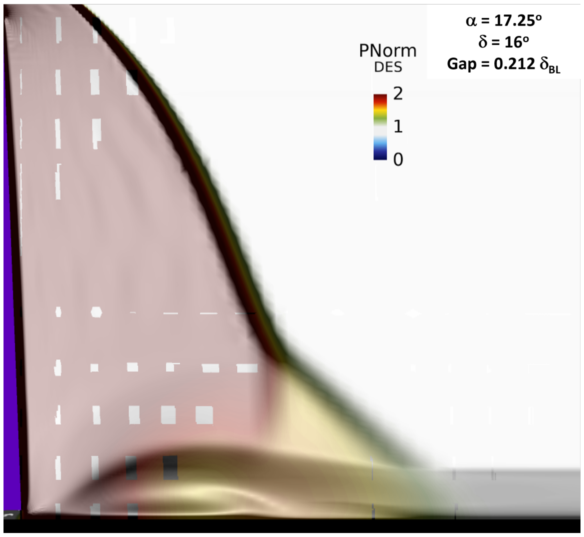

(b) DES

Figure 4.67: Schlieren with normalized pressure; $g/\delta_{BL} = 0.221$, $\alpha = 16\,\text{deg}$. White rectangles are post-processing artifacts from overlaying pressure on top of numerical Schlieren.

due to the fin deflected 12 deg. The surface has been unrolled from the cylindrical coordinate system. The streaklines are colored by normalized surface pressure, and lines indicating the inviscid shock, primary separation, and upstream influence are added in purple, red, and blue respectively. Solid lines in Fig. 4.68 indicate results for the fin above the body of revolution and dashed lines are flat plate results. It can be seen that for a majority of the SBLI region when a fin is placed on the body of revolution the lines of inviscid shock, upstream influence, inviscid shock, and primary separation are within a degree of the flat plate results. However, curvature of each of these lines occurs in both the inception and farfield regions. As the inviscid shock, primary separation, and upstream influence angles change with axial location, the quasi-conical behavior no longer exists for SBLI generated by a swept fin mounted above a flat plate. Pickles et al. [57] also observed this departure in quasi-conical behavior.

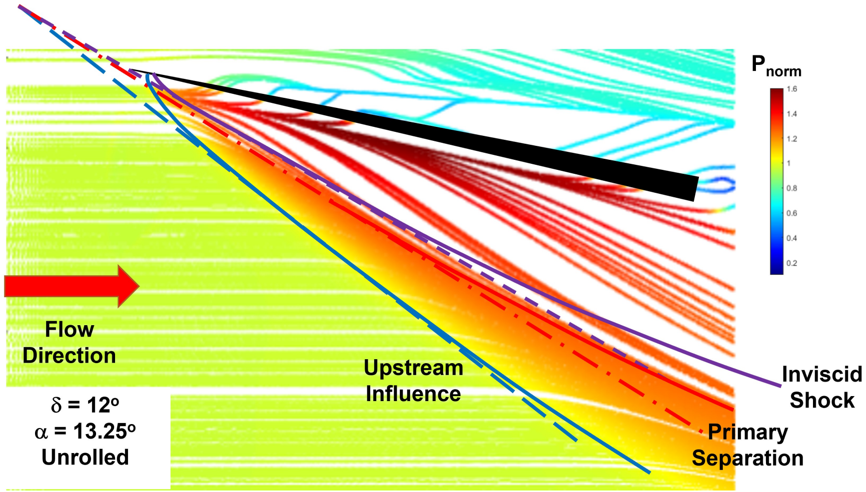

Figure 4.68: Surface streaklines on unrolled body of revolution showing incipient separation for $\delta = 12$ deg. Streaklines colored by normalized surface pressure; upstream influence (blue), primary separation (red), and inviscid shock trace (purple). Solid lines for body of revolution, dashed lines from flat plate results

The streaklines in cylindrical coordinates are shown in Fig. 4.69. The solid line is the inviscid shock line, the dot-dashed line is the primary separation line, and the dashed line is the upstream influence line. Due to the curvature of the body, they curvature of the lines of interest is more apparent in the Fig. 4.69 than in the unrolled image of Fig. 4.68.

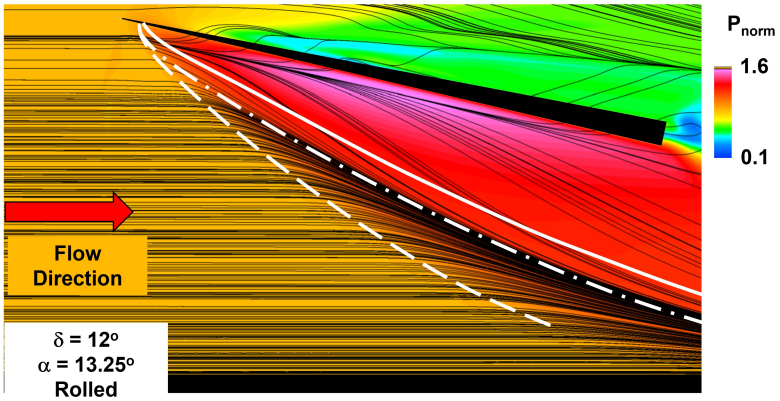

Figure 4.69: Surface streaklines on body of revolution showing incipient separation for $\delta = 12$ deg. Surface colored by normalized surface pressure; upstream influence (dashed), primary separation (dot-dashed), and inviscid shock trace (solid)

The effect of curvature on the SBLI structure is seen in Fig. 4.70 where contours of numerical Schlieren on a yz-plane normal to the inviscid shock wave are shown. The left figure, Fig. 4.70a, is for the fin on a flat plate, and Fig. 4.70b is the fin on the BoR. In both figures, the numerical Schlieren picks up the shock waves, as well as the boundary layer. The lambda shock on the leeward side of the fin is also present in both cases. On the windward side of the fin, the size of the interaction region (distance from fin to the triple point of lambda shock) is less for the case with the fin on a body of revolution. In addition the boundary layer height within the interaction region is greater for the case of the fin on the BoR. Due to curvature, the outer lambda foot is longer for the fin above the BoR compared to the case with the fin above a flat plate.

Figure 4.71 shows numerical Schlieren at two different locations along the fin. The leftmost plane is in the inception region where separation is just starting and the

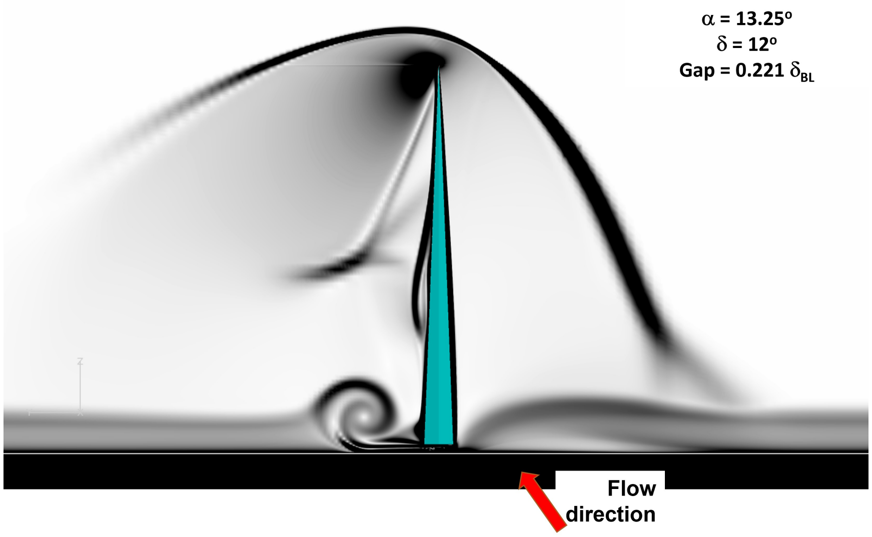

(a) Fin placed above flat plate, $g/\delta_{BL} = 0.221$

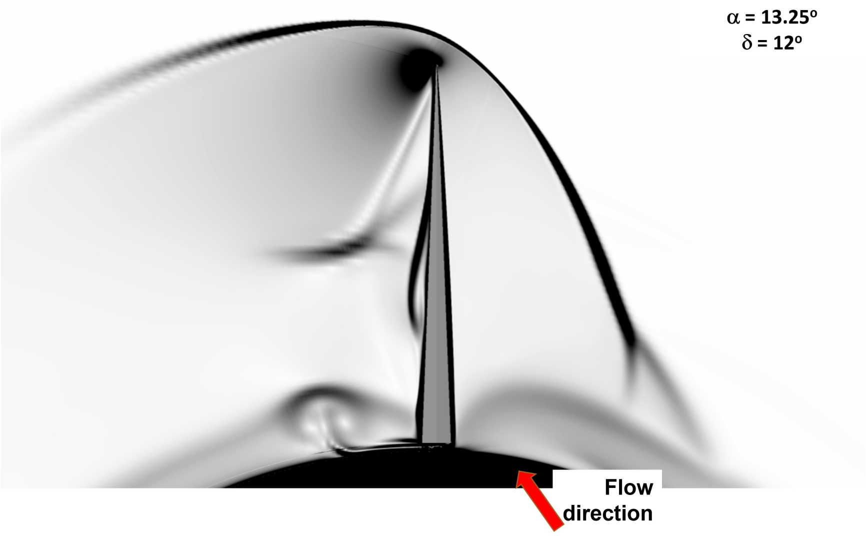

(b) Fin placed above BoR

Figure 4.70: Numerical Schlieren, yz-plane, x/c=0.75, $\delta = 12\,\text{deg}$

lambda shock is submerged in the boundary layer. Downstream the lambda shock is fully present. The converging surface streaklines on the body show the separation location below the outer lambda foot.

The normalized surface pressure is plotted in Fig. 4.72 versus β along a line normal to the inviscid shock. The solid line is for the fin on the flat plate with a gap

Figure 4.71: Numerical Schlieren, yz-plane, $\delta = 12$

of $0.221\delta_{BL}$ and the dot-dashed line is for the fin on the BoR at x/c = 0.69. The upstream influence (UI), primary separation (S), inviscid shock (I), and attachment (A) angles are indicated by points of blue, red, purple, and green respectively. The fin is indicted by the boxes. The normalized surface pressure plotted in Fig. 4.72 confirms the observation in Fig. 4.68 that the upstream influence, primary separation, inviscid shock, and attachment lines for each case are within a degree of each other. However, the maximum pressure is 17% less for the fin on the BoR. The reduction in pressure is expected due to the side relief from the geometry. The reduction in pressure was also observed by Pickles et al. [57].

4.7.1 Leeside Flow

The leeside of the fin above the body of revolution was also investigated. Compared to the flat plate results, similar features were observed. A vortex was produced along the leeside of the fin itself, as is common with delta wings at angle of attack. In a similar way to the flat plate, two additional vortex appear on the surface of the body from the fin leading edge tip, as seen in Fig. 4.73. As before, this occurs due to the gap between the fin and surface.

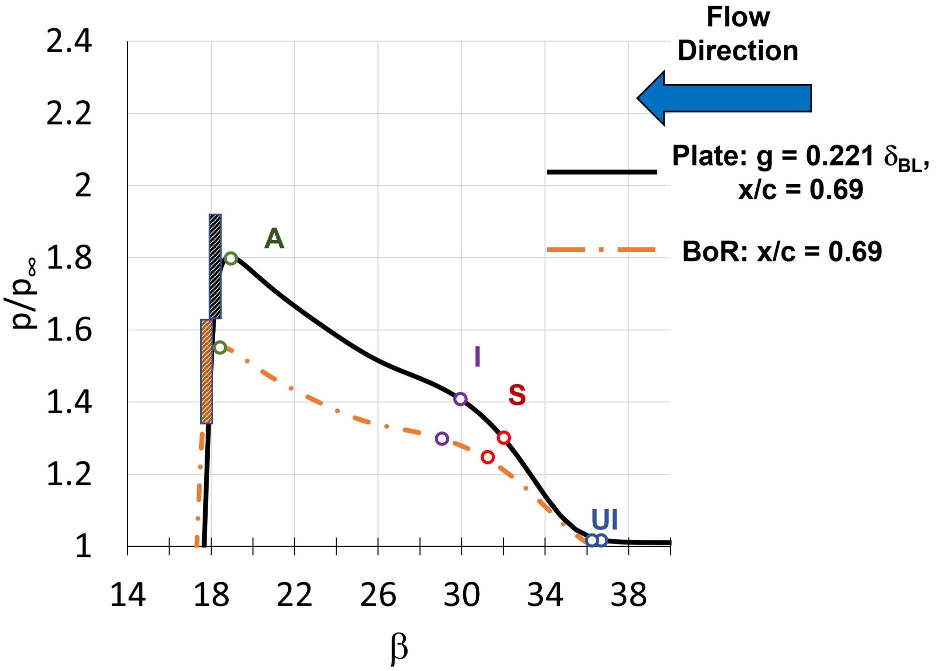

Figure 4.72: Normalized surface pressure with points for attachment (green), inviscid shock (purple), separation (black), and upstream influence (red). Fin on flat plate $g = 0.221\delta_{BL}$ (solid), fin on BoR (dot-dashed). x/c=0.69, Mach 2.5, $\delta = 12$

The additional vortex is visualized using isosurfaces of streamwise vorticity in Fig. 4.74, for both the flat plate (Fig. 4.74a) and body of revolution (Fig. 4.74b). The isosurfaces are colored to show the sign of the vorticity. Planes of vorticity magnitude are added for further visualization, and are at the same chordwise position for each case. In both images, the positive (blue) vortex generated by the fin leading edge extends from the fin tip to the end of the computational domain. A counter-rotating vortex due to flow separation is also present, running alongside the positive vortex. This vortex develops much further downstream for the case where the fin is above the body of revolution. As a result of the relieving effect from bodies of revolution, a high enough adverse pressure gradient to cause separation is not encountered until further downstream. This is seen in Fig. 4.75, where planes of pressure are shown

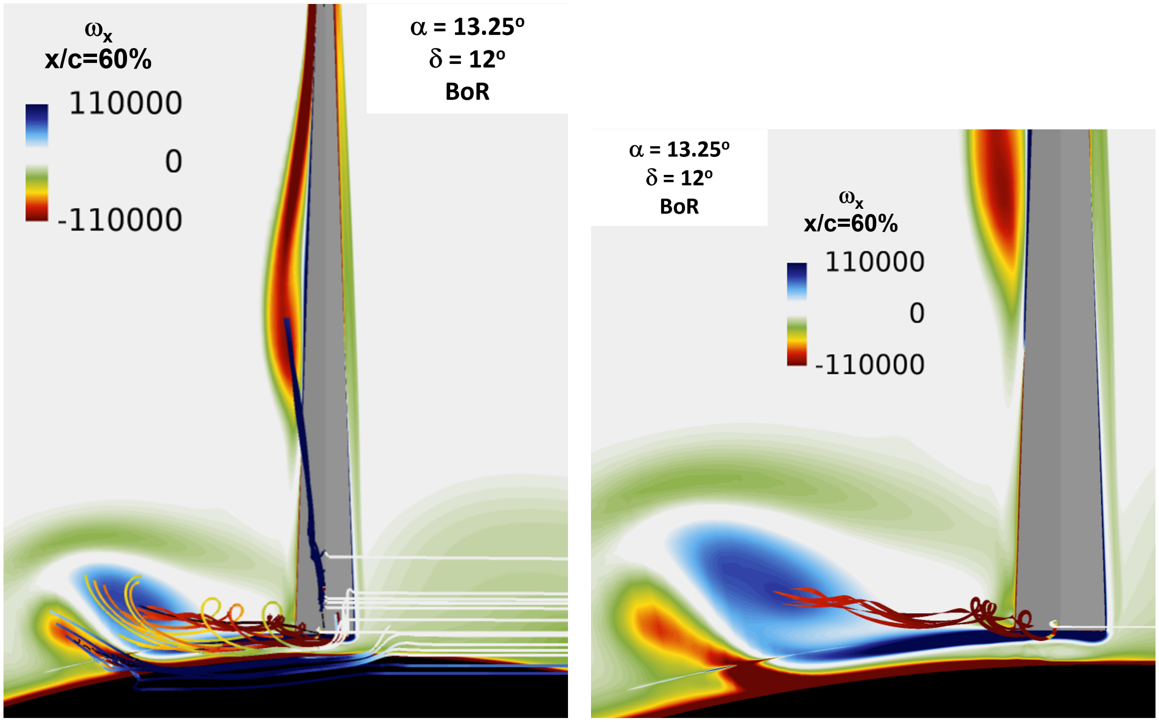

(a) Front view.

(b) Zoomed

Figure 4.73: Contours of streamwise vorticity on leeward side of fin. Fin leading-edge in combination with gap generates two vortexes, illustrated by streamlines (colored for appearance); $\delta = 12\,\text{deg}$, body of revolution.

at two different chordwise locations. Unlike the adverse pressure gradient seen at $x/c = 0.131$ in Fig. 4.31a for the fin above the plate, Fig. 4.75a does not show an adverse pressure gradient, and so separation has not yet occurred. However, further downstream at $x/c = 0.329$ an adverse pressure gradient is present, and so separation does occur at this location. Velocity contours normal to the fin in Fig. 4.76 further illustrate the lack of separation at $x/c = 0.131$, and the appearance of separation at $x/c = 0.329$.

Comparing the surface streamlines between the flat plate and body of revolution results around the fin leading edge in Fig. 4.77, the delay in surface separation is even more apparent. Figure 4.77a shows the streaklines on the flat plate for $g = 0.221\delta_{BL}$,

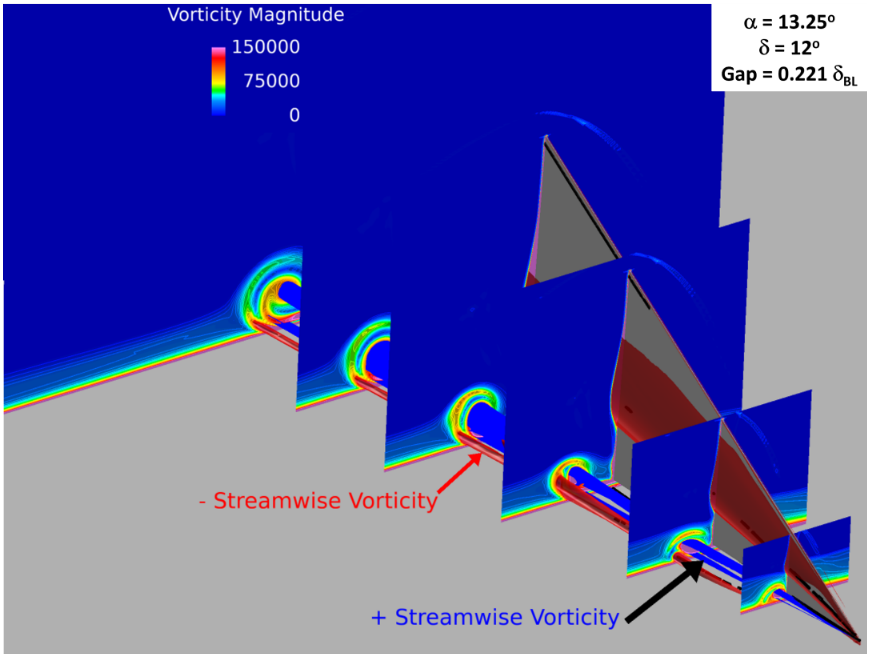

(a) Gap $= 0.221\delta_{BL}$.

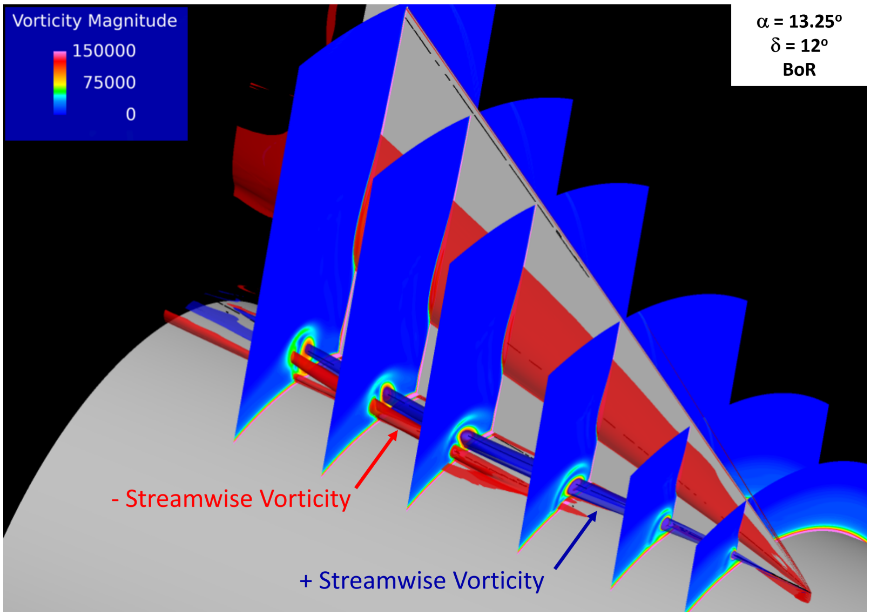

(b) Body of revolution.

Figure 4.74: Contours of vorticity magnitude on leeward side of fin. Isosurfaces of streamwise vorticity illustrate clockwise vortices generated by fin leading-edge (blue) and counter-clockwise vortices generated by the gap (red); $\delta = 12\,\text{deg}$

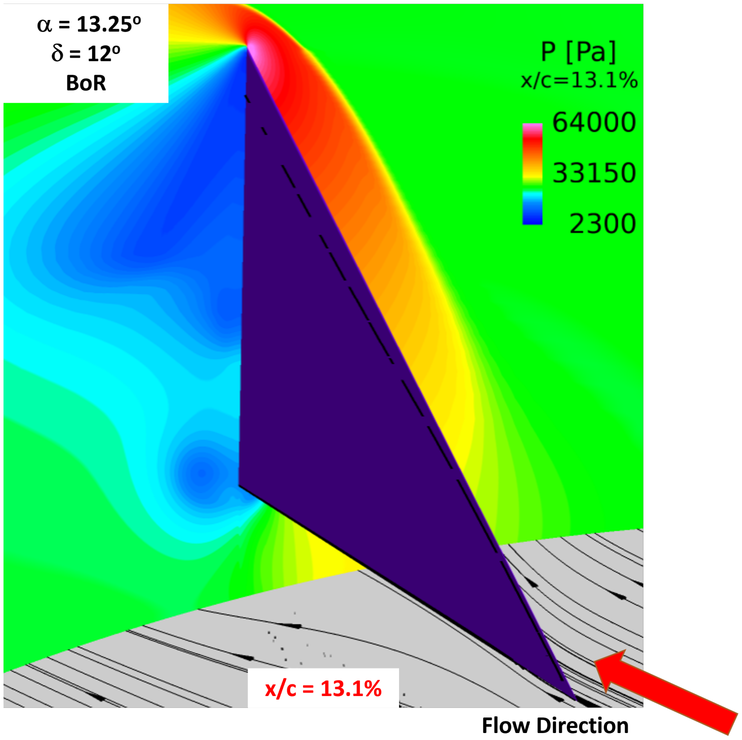

(a) x/c=0.131

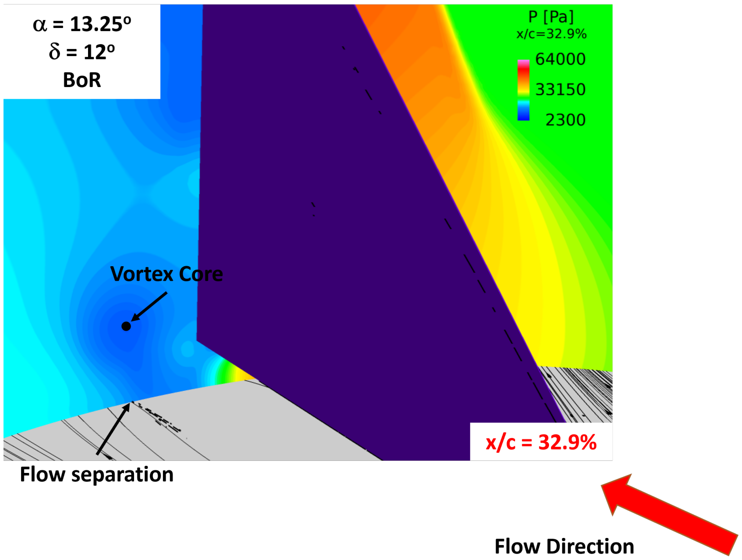

(b) x/c=0.329

Figure 4.75: Pressure contours at two different chordwise locations. Body of revolution; $\delta = 12\,\text{deg}$

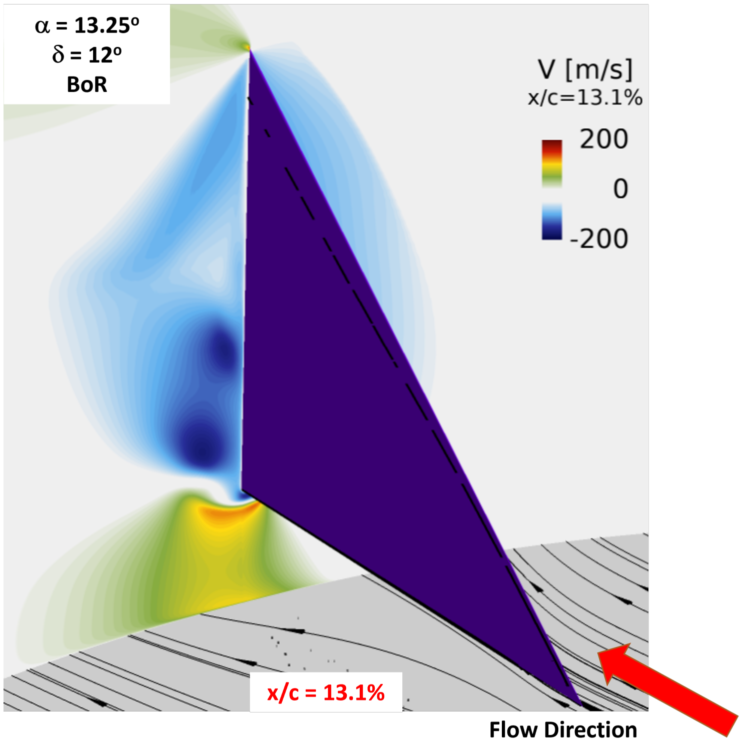

(a) x/c=0.131.

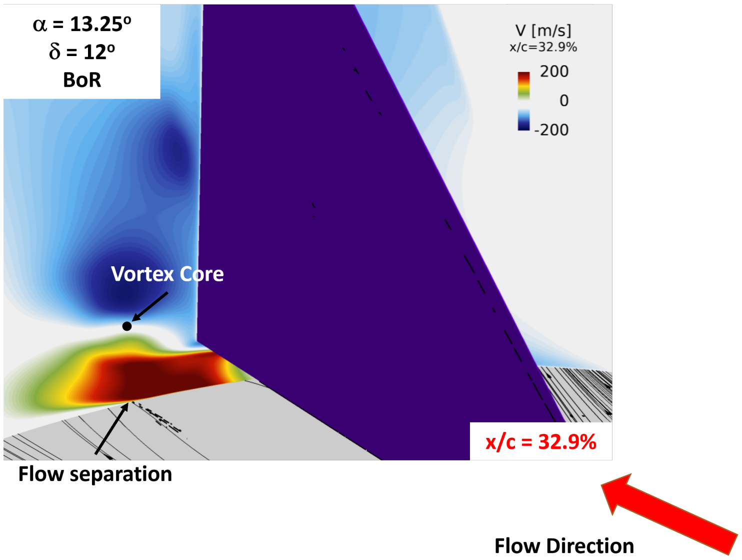

(b) x/c=0.329

Figure 4.76: Velocity contours normal to the fin at two different chordwise locations. Body of revolution; $\delta = 12\,\text{deg}$

Fig. 4.77b $g = 0.443\delta_{BL}$, and Fig. 4.77c shows streaklines on the body of revolution. In each figure, the location of $x/c = 0.131$ and $x/c = 0.329$ are marked. On the flat plate for a gap of $0.221\delta_{BL}$, separation starts around $x/c = 0.131$, but for the gap of $g = 0.443\delta_{BL}$ and the body of revolution it is not until approximately $x/c = 0.3$. Additionally, the secondary separation line does not develop on the body of revolution until approximately $x/c = 0.4$ compared to $x/c = 0.2$ for $g = 0.221\delta_B L$.

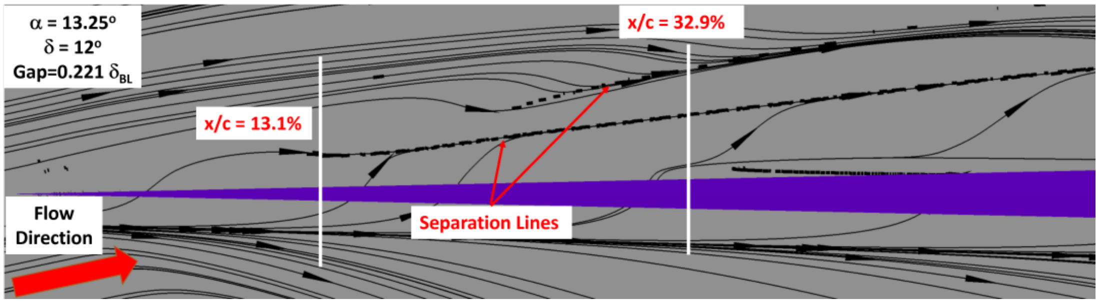

(a) Surface streaklines on plate. $g = 0.221\delta_{BL}$

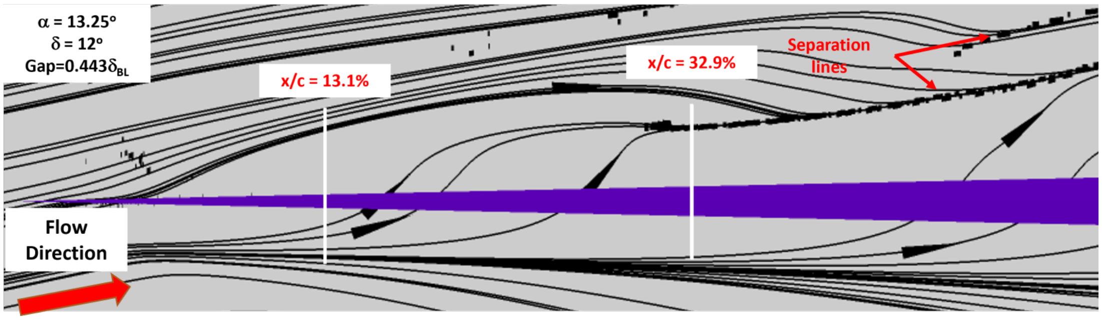

(b) Surface streaklines on plate. $g = 0.443\delta_{BL}$

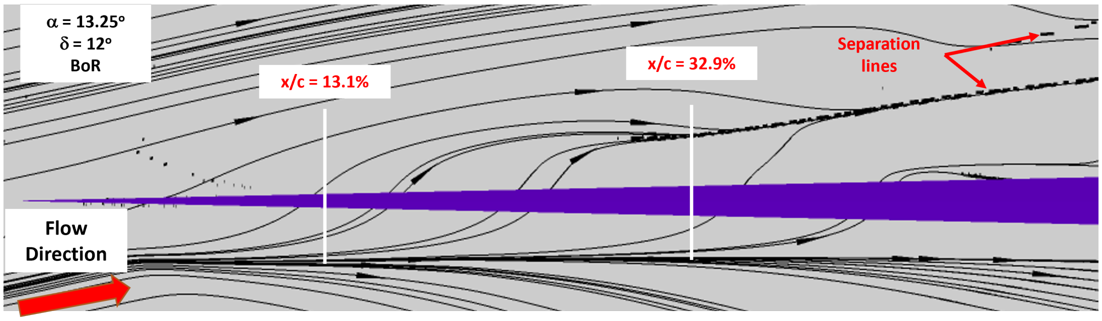

(c) Surface streaklines on body of revolution.

Figure 4.77: Gap = $0.221\delta_{BL}$; $\delta = 12\,\text{deg}$

Contours of streamwise vorticity are shown at several chordwise locations in Fig. 4.78 through Fig. 4.81 for both gap heights above a flat plate and the body of revolution. The general shape of the leading edge blue vortex is more similar between the body of revolution and gap of $0.443\delta_{BL}$ than the gap of $0.221\delta_{BL}$. Since the gap leading edge gap sets up that vortex, and the distance between the fin leading edge and body of revolution is greater than $0.221\delta_{BL}$, it makes sense that the body of revolution would more closely resemble the larger flat plate gap.

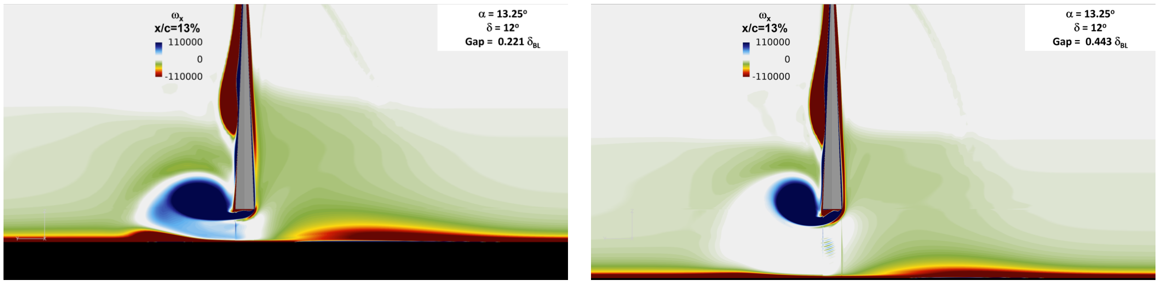

(a) Gap = $0.221\delta_{BL}$. (b) Gap = $0.443\delta_{BL}$.

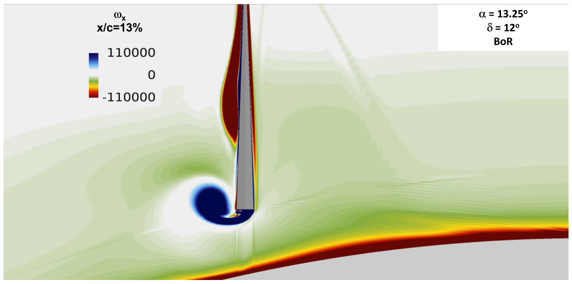

(c) Body of revolution

Figure 4.78: Contours of streamwise vorticity ω_x on YZ plane at $x/c = 0.13$, $\delta = 12\,\text{deg}$.

Going from a flat plate to the body of revolution has minimal affect on the surface flow on the leeside of the fin itself. This is seen in Fig. 4.82, where the surface streaklines on the fin surface for both flat plate gaps and the body of revolution are shown. Each have a separation line along the lower third of the fin, another separation

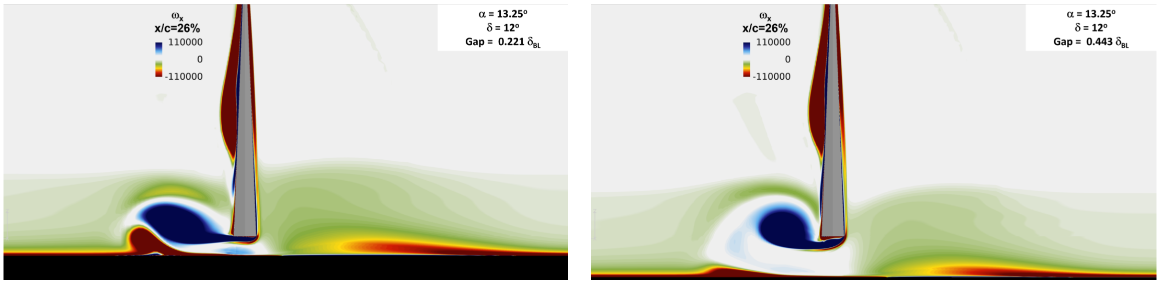

(a) Gap $= 0.221\delta_{BL}$.

(b) Gap $= 0.443\delta_{BL}$.

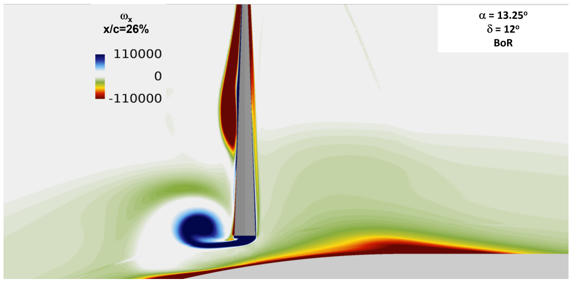

(c) Body of revolution

Figure 4.79: Contours of streamwise vorticity ω_x on YZ plane at $x/c = 0.26$, $\delta = 12\,\text{deg}$.

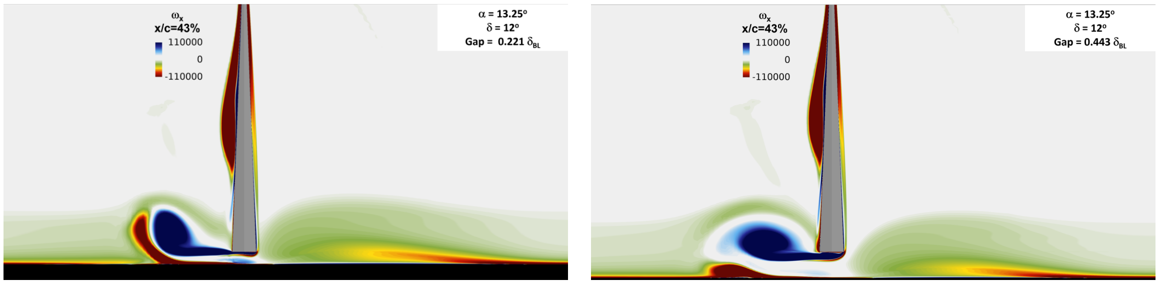

(a) Gap $= 0.221\delta_{BL}$.

(b) Gap $= 0.443\delta_{BL}$.

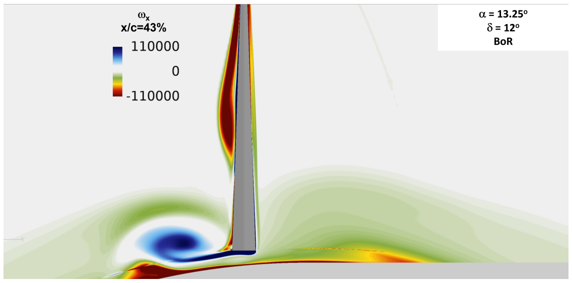

(c) Body of revolution

Figure 4.80: Contours of streamwise vorticity ω_x on YZ plane at $x/c = 0.43$, $\delta = 12\,\text{deg}$.

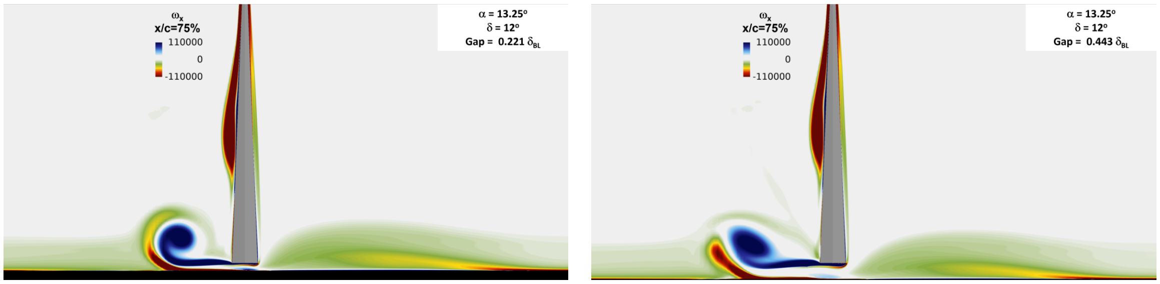

(a) Gap $= 0.221\delta_{BL}$. (b) Gap $= 0.443\delta_{BL}$.

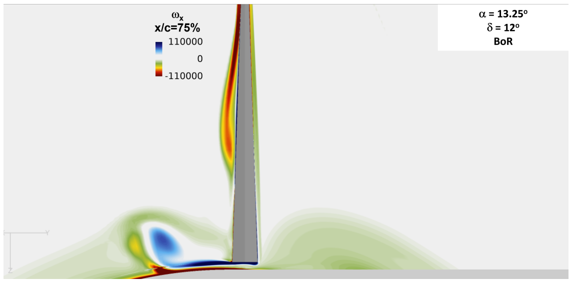

(c) Body of revolution

Figure 4.81: Contours of streamwise vorticity ω_x on YZ plane at $x/c = 0.75$, $\delta = 12\,\text{deg}$.

line along the upper third, and leading edge separation line. The pressure coefficient distribution is also similar in each case.

4.7.2 Fin Forces

Loads were computed for the fin placed above the body of revolution. A comparison is given to the fin over a flat plate, as well as results from Allen [60] in Tab. 4.4. The results by Allen are for a fin deflected 12 deg above a flat plate, and the undeflected fin on a body of revolution at an angle of attack of 12 deg. Results from the current study include all of the fin gaps with the fin placed above a flat plate and the fin deflected 12 deg. For the case with the fin above a body of revolution, both zero angle of attack with a 12 degree deflection, and 12 deg angle of attack with no deflection are reported. The results for fin normal force, hinge moment, and root bending moment all have the same order of magnitude.

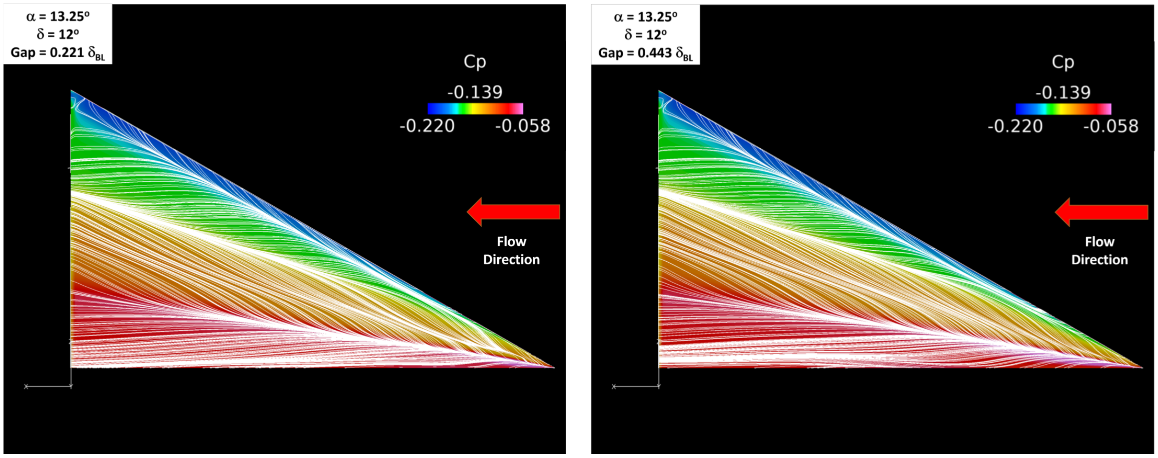

(a) Gap $= 0.221\delta_{BL}$.

(b) Gap $= 0.443\delta_{BL}$.

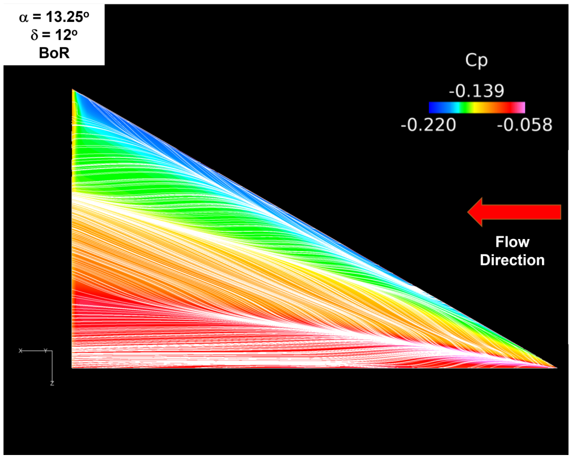

(c) Body of revolution

Figure 4.82: Leeward side of fin colored by pressure coefficient; $\delta = 12$ deg.

From the current study, it is seen that both the fin normal force and root bending moment both decrease with increasing gap (as seen in Sec. 4.5). Additionally, placing the fin above the body of revolution further decreases the fin loads. In both cases where the fin is on the body of revolution, its incidence relative to freestream is 12 deg. As seen in the current results, due to unporting (as described in detail by Nielsen [62] and August [127] for instance) a deflected fin exhibits less effectiveness than an undeflected one at the same incidence.

Table 4.4: Fin Forces and Moments

Data Source	Geometry	C_{NF}	C_{HM}	C_{RBM}
Allen [60]	Flat Plate: $\delta = 12\,\mathrm{deg}$	0.3334	-0.0264	0.1177
	BoR: $\alpha = 12\,\mathrm{deg}$; $\delta = 0\,\mathrm{deg}$	0.3481	-0.0239	0.1248
Current Study	Flat Plate: No Gap; $\delta = 12\,\mathrm{deg}$	0.3608	-0.0259	0.1372
	Flat Plate: $g = 0.221\delta_{BL}$	0.3537	-0.0258	0.1355
	Flat Plate: $g = 0.443\delta_{BL}$	0.3488	-0.0256	0.1342
	BoR: $\alpha = 12\,\mathrm{deg}$; $\delta = 0\,\mathrm{deg}$	0.3466	-0.0322	0.1267
	BoR: $\alpha = 0\,\mathrm{deg}$; $\delta = 12\,\mathrm{deg}$	0.3181	-0.0248	0.1299

CHAPTER 5

CONCLUSIONS

5.1 Summary of the Numerical Studies Performed

Computational fluid dynamic simulations utilizing the SST κ–ω RANS turbulence closure model was used to study swept sharp fin generated shock wave/turbulent boundary layer interaction. The fin was placed above a flat plate such that three gaps existed between the fin and plate: no gap, $g = 0.221\delta_{BL}$, and $g = 0.443\delta_{BL}$. The fin was deflected until incipient separation was determined. Results showed that a swept fin weakens the shock wave compared to an unswept fin such that incipient separation is delayed to a larger deflection angle. This leads to replacing Mach number in the Korkegi criterion with the Mach number normal to the inviscid shock in determining if separation occurs. As the gap was increased, the effect was to weaken the interaction. However, the gap was not increased such that the interaction was no longer present. Overall good agreement was seen between computational results and previously established empirical relationships for the normal Mach number which indicates incipient separation.

Using semi-empirical relations, the numerical results were validated for gap and no gap cases. New equations were proposed for swept fins relating the reduced influence angle to deflection angle, and relating the reduced inviscid shock angle to deflection angle. The influence of gap height on upstream influence, primary separation, and attachment angles was analyzed. It was found that while the gap height affected these angles, its effects on the angles were minimal.

The leeward side of the fin was also investigated. While the flow on the leeward fin surface was little change, the flow around the fin and on the plate was altered. Vortex cores were identified using Eigenmode analysis. It was found that without a gap, only a vortex generated at the leading edge was produced due to pressure differences across the leeside and windward side of the fin. For fins with gaps, two additional vortices were generated. One at the fin leading edge, and a weaker one at the plate surface. Increasing the gap changes the location and shape of the additional vortices.

Flow on the leeward side of the fin was studied and compared to experimental results for delta wings. It was found that the flow on the leeward side of a fin mounted on a flat plate was similar to that of flow on the leeward side of a delta wing. The plate introduced some crossflow from the plate towards the fin tip, which altered the shape of the lambda shock. No appreciable difference in the flow on the fin surface was observed when introducing a gap between the fin and plate.

CFD results were analyzed to determine the how the gap affects the fin normal force, hinge moment, and root bending moment. These results followed trends of measured results for varying gap heights, where increasing the gap resulted in a loss of fin effectiveness.

For the fin mounted above a body of revolution and compared to results for a fin mounted above a flat plate. Consistent with results by Pickles et al. [57], lines of upstream influence, separation, and inviscid shock were found to curve in the farfield region, rather than remain linear. At the chordwise position studied, the angles of these lines for the body of revolution and flat plate were within a degree of each other, but further downstream of this position a larger difference between the angles occurs. The size of the interaction region for the BoR was smaller compared to flat plate results, with the inviscid shock staying closer to the fin. Also, the body of revolution caused the surface pressures within the separation region to decrease significantly when compared to the separation region generated by the same fin above a flat plate. This same behavior was observed by Pickles et al. [57]. Additionally, the lines of upstream influence, separation, and inviscid shock were found to curve in the farfield region, rather than remain linear.

RANS results were compared to DES results for $\delta = 16\,\text{deg}$. At this condition, a difference of two degrees was observed in the predicted separation line angle between DES and RANS, but the inviscid shock and upstream influence lines were identical. A stronger main separation vortex was predicted using DES, however the mean flow and separation characteristics were consistent between the two methods.

5.2 Recommendations for Future Work

Future research areas include placing the fin on bodies of revolution with multiple diameters and gap heights to generalize the results. It would also be beneficial to investigate the formation of the leeside vortex and unsteadiness of swept fin induced SBLI with DES or LES. The examination of different fin leading edge sweep angles and bluntness and their influence on incipient separation is another recommended area of study. It would be of immense value to generate experimental data and compare to the results obtained in this study.

REFERENCES

[1] D. S. Dolling, “Fifty years of shock-wave/boundary-layer interaction research: What next?” *AIAA Journal*, vol. 39, no. 8, pp. 1517–1531, 2001. [Online]. Available: https://doi.org/10.2514/2.1476

[2] D. D. Knight and A. A. Zheltovodov, “Ideal-gas shock wave-turbulent boundary-layer interactions (STBLI) in supersonic flows and their modeling: Two-dimensional interactions,” in *Shock Wave-Boundary-Layer Interactions*, H. Babinsky and J. K. Harvey, Eds. Cambridge, 2011, ch. 4, pp. 137–201.

[3] A. A. Zheltovodov and D. D. Knight, “Ideal-gas shock wave-turbulent boundary-layer interactions in supersonic flows and their modeling: Three-dimensional interactions,” in *Shock Wave-Boundary-Layer Interactions*, H. Babinsky and J. K. Harvey, Eds. Cambridge, 2011, ch. 5, pp. 202–258.

[4] J. D. Anderson Jr, *Fundamentals of Aerodynamics*, 4th ed. McGraw Hill, 2007, ch. 4.

[5] A. Leder, *Abgelöste Strömungen. Physikalische Grundlagen.* Vieweg Verlag, 1992.

[6] J. Deléry, “Physical introduction,” in *Shock Wave-Boundary-Layer Interactions*, H. Babinsky and J. K. Harvey, Eds. Cambridge, 2011, ch. 2, pp. 5–86.

[7] M. S. Holden, “Experimental studies of shock wave-boundary-layer interactions in hypersonic flows,” in *Shock Wave-Boundary-Layer Interactions*, H. Babinsky and J. K. Harvey, Eds. Cambridge, 2011, ch. 6, pp. 259–313.

[8] P. A. Durbin and G. Medic, “High Reynolds number flow and boundary layers,” in *Fluid Dynamics with a Computational Perspective.* Cambridge, 2013, ch. 5, pp. 167–209.

[9] J. A. Schetz and R. D. W. Bowersox, *Boundary Layer Analysis*, 2nd ed. AIAA, 2011.

[10] A. J. Smits and J.-P. Dussauge, *Turbulent Shear Layers in Supersonic Flow*, 2nd ed. Springer, 2006, ch. 10.

[11] W. R. Sears, “The boundary layer of yawed cylinders,” *Journal of the Aeronautical Sciences*, vol. 15, no. 1, pp. 49–52, 1948. [Online]. Available: https://doi.org/10.2514/8.11499

[12] D. J. Peake, “Controlled and uncontrolled flow separation in three dimensions,” NRC, NAE LR–591, 1976.

[13] E. Maskell, “Flow separation in three-dimensions,” Royal Aeronautical Establishment, Aero. Report 2565, Nov. 1955.

[14] M. J. Lighthill, “Attachment and separation in three dimensional flow,” in *Laminar Boundary Layers*, L. Rosenhead, Ed. Oxford University Press, 1963, ch. 2, pp. 72–82, section 2.6.

[15] R. Legendre, “Lignes de courant d’un écoulement permanent: Décollement et séparation,” *La Recherche Aérospatiale*, vol. 1977-6, pp. 327–335, 1977.

[16] M. Tobak and D. J. Peake, “Topology of three-dimensional separated flows,” *Annual Review of Fluid Mechanics*, vol. 14, no. 1, pp. 61–85, 1982.

[17] F. K. Lu, “Quasiconical free interaction between a swept shock and turbulent boundary layer,” *AIAA Journal*, vol. 31, no. 4, pp. 686–692, 1993.

[18] F. K. Lu and G. S. Settles, “Conical similarity of shock/boundary-layer interactions generated by swept and unswept fins,” *AIAA Journal*, vol. 23, no. 7, pp. 1021–1027, 1985.

[19] F. K. Lu, G. S. Settles, and C. C. Horstman, "Mach number effects on conical surface features of swept shock-wave/boundary-layer interactions," *AIAA Journal*, vol. 28, no. 1, pp. 91–97, 1990.

[20] F. K. Lu and G. S. Settles, "Upstream-influence scaling of sharp fin interactions," *AIAA Journal*, vol. 29, no. 7, pp. 1180–1181, 1991.

[21] ——, "Inception length to a fully developed, fin-generated, shock-wave, boundary-layer interaction," *AIAA Journal*, vol. 29, pp. 758–762, 1991.

[22] D. L. Otten and F. K. Lu, "Preliminary study of shock/boundary-layer interactions generated by a sharp fin mounted above a flat plate," AIAA Paper 2021–4118, 2021.

[23] I. C. Richards, "Supersonic flow over low aspect-ratio wings," Ph.D. dissertation, Cranfield Insitute of Technology, November 1976.

[24] R. M. Wood, "Supersonic aerodynamics of delta wings," NASA TP 2771, 1988.

[25] A. Stanbrook and L. C. Squire, "Possible types of flow at swept leading edges," *Aeronautical Quarterly*, vol. 15, no. 1, pp. 72–82, 1964.

[26] D. S. Miller and R. M. Wood, "Lee-side flow over delta wings at supersonic speeds," NASA TP 2430, 1985.

[27] K. Narayan and S. Seshadri, "Shock-induced separated flows on the lee surface of delta wings," *Aeronautical Journal*, vol. 91, no. 903, pp. 128–141, 1987.

[28] G. S. Bluford Jr, "Numerical solution of the supersonic and hypersonic viscous flow around thin delta wings," *AIAA Journal*, vol. 17, no. 9, pp. 942–949, 1979.

[29] J. G. Szodruch, "Lee side flow for slender delta wings of finite thickness," NASA-TM-75753, 1980.

[30] J. G. Szodruch and D. J. Peake, "Leeward flow over delta wings at supersonic speeds," NASA-TM-81187, 1980.

[31] K. Narayan and S. Seshadri, “Types of flow on the lee side of delta wings,” *Progress in Aerospace Sciences*, vol. 33, no. 3, pp. 167–257, 1997.

[32] L. C. Squire, “Flow regimes over delta wings at supersonic and hypersonic speeds,” *Aeronautical Quarterly*, vol. 27, no. 1, pp. 1–14, 1976.

[33] D. M. Rao and A. H. Whitehead Jr, “Lee-side vortices on delta wings at hypersonic speeds,” *AIAA Journal*, vol. 10, no. 11, pp. 1458–1465, 1972.

[34] W. H. Michael, Jr., “Flow studies on flat-plate delta wings at supersonic speeds,” NACA TN 3472, 1955.

[35] D. L. Otten and F. K. Lu, “Flow features of swept shock/turbulent boundary-layer interaction due to a gap beneath a sharp fin,” *Aerospace Science and Technology*, vol. 130, 2022. [Online]. Available: https://www.sciencedirect.com/science/article/pii/S1270963822006083

[36] ——, “Flow on leeward side of a sharp fin undergoing swept shock/turbulent boundary-layer interaction,” AIAA Paper 2023–1434, 2023.

[37] A. G. Panaras, *Aerodynamic Principles of Flight Vehicles*, 1st ed., N. Allen, Ed. AIAA, 2012.

[38] J.-Z. Wu, H.-Y. Ma, and M.-D. Zhou, *Vorticity and Vortex Dynamics*, 1st ed. Springer, 2006.

[39] M. S. Holden, “Experimental studies of quasi-two-dimensional and three-dimensional viscous interaction regions induced by skewed-shock and swept-shock boundary layer interaction,” AIAA Paper 2004–2879, 1984.

[40] J. Délery and J. G. Marvin, “Turbulent shock-wave/boundary-layer interactions,” 1986, AGARD-AG-280.

[41] H. Babinsky and J. K. Harvey, *Shock Wave-Boundary-Layer Interactions*. Cambridge, 2011.

[42] G. S. Settles and L. J. Dodson, "Supersonic and hypersonic shock/boundary-layer interaction database," *AIAA Journal*, vol. 32, no. 7, pp. 1377–1383, 1994.

[43] D. S. Dolling and W. B. McClure, "Flowfield scaling in sharp fin-induced shock wave/turbulent boundary-layer interaction," *AIAA Journal*, vol. 23, no. 2, pp. 201–206, 2 1985.

[44] E. G. Pace and F. K. Lu, "On the scale of surface features in hypersonic swept shock boundary-layer interactions," AIAA Paper 91–1769, 1991.

[45] D. Knight, C. C. Hortsman, B. Shapey, and S. Bogdonoff, "Structure of supersonic turbulent flows past a sharp fin," *AIAA Journal*, vol. 25, no. 10, pp. 1331–1337, 1987.

[46] F. S. Alvi and G. S. Settles, "Physical model of the swept shock wave/boundary-layer interaction flowfield," *AIAA Journal*, vol. 30, no. 9, pp. 2252–2258, 9 1992.

[47] C. H. Law, "Three-dimensional shock wave-turbulent boundary layer interactions at Mach 6," AD-A014 738, 1975, Aerodynamics Research Laboratory (ARL) Interim Report.

[48] F. K. Lu, "Fin generated shock-wave boundary-layer interactions," Ph.D. dissertation, Pennsylvania State University, May 1988.

[49] S. Garg and G. S. Settles, "Unsteady pressure loads generated by swept-shock-wave/boundary-layer interactions," *AIAA Journal*, vol. 34, no. 6, pp. 1174–1181, 6 1996.

[50] G. He, J. Zhou, and Y. Zhao, "Application of free interaction theory in swept shock wave/turbulent boundary layer interactions," *Journal of Visualization*, vol. 21, no. 2, pp. 203–214, April 2018.

[51] R. D. Neumann and J. R. Hayes, "Aerodynamic heating in the fin interaction region of generalized missile shapes at Mach 6 (Modular Missile Test Program),"

AFFDL-TR-79-3066, 1979, Air Force Flight Dynamics Laboratory, Wright-Patterson Air Force Base, Ohio.

[52] M. I. Kussoy and C. C. Horstman, “Documentation of two- and three-dimensional hypersonic shock wave/turbulent boundary layer interaction flows,” NASA-TM-101075, 1989.

[53] D. Fano, J. Poggie, and G. A. Blaisdell, “Aerodynamic heating in missile-fin interaction region,” AIAA Paper 2020–0583, 2020.

[54] R. Alviani, D. Fano, J. Poggie, and G. Blaisdell, “Aerodynamic heating in the gap between a missile body and a control fin,” *Journal of Spacecraft and Rockets*, vol. 59, no. 4, pp. 1111–1124, 2022.

[55] J. Pickles, P. Subbareddy, and V. Narayanaswamy, “Sharp-fin induced shock wave/turbulent boundary layer interactions in an axisymmetric configuration,” AIAA Paper 2016–3340, 2016.

[56] J. Pickles, M. Balachandra, P. Subbareddy, and V. Narayanaswamy, “Sharp-fin induced shock wave/turbulent boundary layer interactions in an axisymmetric configuration,” AIAA Paper 2017–4314, 2017.

[57] J. Pickles and V. Narayanaswamy, “Investigation of surface curvature effects on unseparated fin shock-wave/boundary-layer interactions,” *AIAA Journal*, vol. 58, no. 2, pp. 770–778, 2020.

[58] R. R. Martis, A. Misra, and A. Singh, “Effect of microramps on separated swept shock wave/boundary-layer interactions,” *AIAA Journal*, vol. 52, no. 3, pp. 591–603, 2014.

[59] J. Pickles and V. Narayanaswamy, “Control of fin shock induced flow separation using vortex generators,” *AIAA Journal*, vol. 58, no. 11, pp. 4794–4806, 2020.

[60] J. M. Allen, “Parametric fin-body and fin-plate database for a series of 12 missile fins,” NASA TM-2001-210652, 2001.

[61] C. Dahlke and W. Pettis, “Normal force effectiveness of several fin planforms with streamwise gaps at Mach numbers of 0.8 to 5.0,” RD-TR-70-8 (Revision), 1970, U.S. Army Missile Command, Redstone Arsenal, Alabama.

[62] J. N. Nielsen, *Missile Aerodynamics*, 1st ed. McGraw-Hill, 1960.

[63] F. Zhang, S. Yi, X. Xu, H. Niu, and X. Lu, “A swept fin-induced flow field with different mounting gaps,” *Chinese Journal of Aeronautics*, vol. 34, no. 1, pp. 148–162, 2021.

[64] H. Mirels, “Gap effect on slender wing-body interference,” *Journal Aeronautical Sciences*, vol. 20, no. 8, 1953.

[65] A. Mikhail, “Fin gaps and body slots: Effects and modeling for guided projectiles,” AIAA Paper 87–0447, 1987.

[66] ——, “Lift losses for large fin-body gaps in transonic and supersonic speeds: Data correlation and modeling,” AIAA Paper 89–0332, 1989.

[67] D. W. Dugan and K. Hikido, “Theoretical investigation of the effects upon lift of a gap between wing and body of a slendor wing-body combination,” NACA TN 3224, 1954.

[68] D. W. Dugan, “Experimental investigation of some aerodynamic effects of a gap between wing and body of a moderately slender wing-body combination at a Mach number of 1.4,” NACA RM A55D08, 1955.

[69] G. R. Gromillion, “A compilation of static stability and fin loads data for slender body missile models with and without tail fins and wings. Volume 1,” AEDC-TR-75-125, 1976.

[70] D. L. Otten and F. K. Lu, “Gap effects on shock/boundary-layer interactions generated by a sharp fin mounted above a flat plate,” AIAA Paper 2022–1064, 2022.

[71] R. H. Korkegi, "A simple correlation for incipient turbulent boundary-layer separation due to a skewed shock wave," *AIAA Journal*, vol. 11, no. 11, pp. 1578–1579, 1973.

[72] ——, "A lower bound for three-dimensional turbulent separation in supersonic flow," *AIAA Journal*, vol. 23, no. 3, pp. 475–476, 1985.

[73] F. K. Lu and G. S. Settles, "Color surface-flow visualization of fin-generated shock wave boundary-layer interactions," *Experiments in Fluids*, vol. 8, no. 6, pp. 352–354, 1990.

[74] A. A. Zheltovodov, "Shock waves/turbulent boundary-layer interactions – fundamental studies and applications," AIAA Paper 1996–1977, 1996.

[75] D. J. Peake and M. Tobak, "Three-dimensional separation and reattachment," NASA TM 84221, 1982.

[76] A. A. Zheltovodov, A. Maksimov, and E. Schülein, "Development of turbulent separated flows in the vicinity of swept shock waves," in *The Interactions of Complex 3-D Flows*, A. Kharitonov, Ed., 1987, pp. 67–91, in Russian.

[77] A. A. Zheltovodov, "Regimes and properties of three-dimensional separation flows initiated by skewed compression shocks," *Journal of Applied Mechanics and Technical Physics*, vol. 23, no. 3, pp. 413–418, 1982.

[78] D. J. Friedlander, "Understanding the flow physics of shock boundary-layer interactions using CFD and numerical analyses," NASA/TM–2013-218081, 2013.

[79] D. Knight, H. Yan, A. G. Panaras, and A. Zheltovodov, "Advances in CFD prediction of shock wave turbulent boundary layer interactions," *Progress in Aerospace Sciences*, vol. 39, no. 2, pp. 121–184, 2 2003.

[80] G. S. Settles and Y. Lee, "Swept shock/boundary layer interaction experiments in support of CFD code validation," NASA-CR-190583, 1992.

[81] C. C. Horstman, "Prediction of secondary separation in shock wave boundary-layer interactions," *Computers and Fluids*, vol. 17, no. 4, pp. 611–614, 1989.

[82] C. Horstman and C. Huang, "Computation of three-dimensional turbulent flows at supersonic speeds," in *AIAA 17th Aerospace Sciences Meeting*, 1979.

[83] D. D. Knight, "Numerical simulation of a three-dimensional shock wave-turbulent boundary-layer interaction generated by a sharp fin at Mach 4," *Computing Systems in Engineering*, vol. 1, no. 2-4, pp. 391–399, 1990.

[84] A. G. Panaras, "Numerical investigation of the high-speed conical flow past a sharp fin," *Journal of Fluid Mechanics*, vol. 236, pp. 607–633, 1992.

[85] A. G. Panaras and E. Stanewsky, "Numerical study of secondary separation in glancing shock/turbulent boundary layer interactions," in *28th Joint Propulsion Conference and Exhibit*. Nashville, U.S.A.: AIAA Paper 92-3666, 1992.

[86] J. R. DeBonis, W. L. Oberkampf, R. T. Wolf, P. D. Orkwis, M. G. Turner, and H. Babinsky, "Assessment of computational fluid dynamics (CFD) models for shock boundary-layer interaction," NASA/TM-2011-216832, 2011.

[87] R. F. Vieira and J. L. F. Azevedo, "RANS simulation of flows with shock wave-boundary layer interaction," AIAA Paper 2013–0985, 2013.

[88] J. J. Sebastian and F. K. Lu, "Upstream-influence scaling of fin-induced laminar shockwave/boundary-layer interactions," *AIAA Journal*, vol. 59, no. 5, pp. 1861–1864, 2021.

[89] ——, "Free interaction in three-dimensional, laminar shockwave/boundary-layer interaction," AIAA Paper 2021–0490, 2021.

[90] A. Salin, Y. F. Yao, and A. A. Zheltovodov, "Numerical prediction of 3-D supersonic turbulent separation initiated by a single-fin," in *29th International Symposium on Shock Waves 2*, R. Bonazza and D. Ranjan, Eds. Springer International Publishing, 2015, pp. 1265–1270.

[91] F. K. Lu, “New results on the incipient separation of shock/boundary-layer interactions,” *Procedia Engineering*, no. 126, pp. 12–15, 2015.

[92] J. Fang, L. Lu, Y. Yao, and A. A. Zheltovodov, “Large-eddy simulation of a three-dimensional hypersonic shock wave/turbulent boundary layer interaction of a single-fin,” AIAA Paper 2015–1062, 2015.

[93] A. Panaras, “Algebraic turbulence modeling for swept shock-wave/turbulent boundary-layer interactions,” *AIAA Journal*, vol. 35, no. 3, pp. 456–463, 1997.

[94] ——, “The effect of the structure of swept-shock-wave/turbulent-boundary-layer interactions on turbulence modeling,” *Journal of Fluid Mechanics*, vol. 338, pp. 203–230, 1997.

[95] ——, “Calculation of flows characterized by extensive cross-flow separation,” *AIAA Journal*, vol. 42, no. 12, pp. 2474–2481, 2004.

[96] D. V. Gaitonde, “Progress in shock wave/boundary layer interactions,” *Progress in Aerospace Sciences*, vol. 72, pp. 80–99, 2015. [Online]. Available: https://www.sciencedirect.com/science/article/pii/S0376042114000815

[97] S. Palaniswamy, S. R. Chakravarthy, and D. K. Ota, “Finite rate chemistry for USA-series codes: Formulation and applications,” AIAA Paper 89–0200, 1989.

[98] “ICFD++ theory guide,” Metacomp Technologies, Tech. Rep., 2022.

[99] J. C. Tannehill, D. A. Anderson, and R. H. Pletcher, *Computational Fluid Dynamics and Heat Transfer*, 2nd ed. Taylor and Francis, 1997.

[100] W. Sutherland, “LII. the viscosity of gases and molecular force,” *The London, Edinburgh, and Dublin Philosophical Magazine and Journal of Science*, vol. 36, no. 223, pp. 507–531, 1893.

[101] S. B. Pope, *Turbulent Flows*, 1st ed. Cambridge, 2000.

[102] T. Cebeci, *Analysis of Turbulent Flows with Computer Programs*, 3rd ed. Butterworth-Heinemann, 2013.

[103] F. R. Menter, “Two-equation eddy-viscosity turbulence models for engineering applications,” *AIAA Journal*, vol. 32, no. 8, pp. 1598–1605, 1994.

[104] J. D. Anderson Jr, *Computational Fluid Dynamics: The Basics with Applications*, 1st ed. McGraw Hill, 1995.

[105] R. M. Cummings, W. H. Mason, S. A. Morton, and D. R. McDaniel, *Applied Computational Aerodynamics*, 1st ed. Cambridge University Press, 2015.

[106] S. V. Patankar, *Numerical Heat Transfer and Fluid Flow*, 1st ed. Taylor and Francis, 1980.

[107] P. Batten, N. Clarke, C. Lambert, and D. M. Causon, “On the choice of wavespeeds for the HLLC Riemann solver,” *SIAM Journal on Scientific Computing*, vol. 18, no. 6, pp. 1553–1570, 1997.

[108] P. Batten, M. Leschziner, and U. Goldberg, “Average state jacobians and implicit methods for compressible viscous and turbulent flows,” *Journal of Computational Physics*, vol. 137, no. 1, pp. 38–78, 1997.

[109] E. F. Toro, M. Spruce, and W. Speares, “Restoration of the contact surface in the HLL-Riemann solver,” *Shock Waves*, vol. 4, no. 1, pp. 25–34, 1994.

[110] M. S. Guerrero, “Parallel multigrid algorithms for computational fluid dynamics and heat transfer,” Ph.D. dissertation, Universitat Politècnica de Catalunya, 2000.

[111] N. J. Georgiadis, C. L. Rumsey, and G. P. Huang, “Revisiting turbulence model validation for high-Mach number axisymmetric compression corner flows,” AIAA Paper 2015–0316, 2015.

[112] E. Van Driest, “The problem of aerodynamic heating,” *Aeronautical Engineering Review*, vol. 15, no. 10, pp. 26–41, 1956.

[113] P. G. Huang and G. N. Coleman, “Van Driest transformation and compressible wall-bounded flows,” *AIAA Journal*, vol. 32, no. 10, pp. 2110–2113, 1994.

[114] H. Reichardt, “Complete representation of the turbulent velocity distribution in smooth pipes,” *Journal of Applied Mathematics and Mechanics*, vol. 31, no. 7, pp. 208–219, 1951.

[115] P. S. Granville, “A modified law of the wake for turbulent shear layers,” *Journal of Fluids Engineering*, pp. 578–580, 1976.

[116] T. B. Gatski and J.-P. Bonnet, *Compressibility, Turbulence and High Speed Flow*, 2nd ed. Elsevier, 2013.

[117] J. L. Stollery and L. Bates, “Turbulent hypersonic viscous interaction,” *Journal of Fluid Mechanics*, vol. 63, no. 1, pp. 145–156, 1974.

[118] “Working with FieldView. software release version 20,” https://fieldviewcfd.azureedge.net/docs/Working_with_FieldView.pdf, 2020, accessed: 2022-09-30.

[119] G. S. Settles and R. L. Kimmel, “Similarity of quasiconical shock wave/turbulent boundary-layer interactions,” *AIAA Journal*, vol. 24, no. 1, pp. 47–53, 1986.

[120] A. A. Zheltovodov, “Physical singularities and certain properties of two- and three-dimensional separation flows at supersonic velocities,” *Izv. Akad. Nauk SSSR, Mekh. Zhidk. Gaza*, no. 3, 1979.

[121] A. Stanbrook, “An experimental study of the glancing interaction between a shock wave and a boundary layer,” British ARC C.P. No. 555, 1961.

[122] L. F. Scuderi, “Expressions for predicting 3D shock wave-turbulent boundary layer interaction pressures and heating rates,” AIAA Paper 79–2, 1978.

[123] R. Haimes and D. Kenwright, “On the velocity gradient tensor and fluid feature extraction,” AIAA Paper 1999–3288, 1999.

[124] D. N. Kenwright, C. Hense, and C. Levit, “Feature extraction of separation and attachment lines,” *IEEE Transactions on Visualization and Computer Graphics*, vol. 5, no. 2, pp. 135–144, 1999.

[125] D. N. Kenwright, “Automatic detection of open and closed separation and attachment lines,” Proc. IEEE Visualization ’98, pp. 151–158, 1998.

[126] R. L. Maltby, “Flow visualization in wind tunnels using indicators,” AGARDograph, Tech. Rep. 70, 1962.

[127] H. August, “Improved control surface effectiveness for missiles,” in *AIAA 20th Aerospace Sciences Meeting*, 1979.

BIOGRAPHICAL STATEMENT

Dustin L. Otten was born in May 1986 to David and Danele Otten. He graduated from Westmoore High School in 2004 and was admitted to the University of Nebraska - Lincoln. He attended UNL for one year, before transferring to the University of Oklahoma in 2005, where he received his B.S. and M.S. degrees from the University of Oklahoma in 2008 and 2009, respectively, both in Aerospace Engineering. For his M.S., Dustin researched computational methods designed to reduce the statistical error within the direct simulation Monte Carlo (DSMC) method. The title of his master's thesis is "Weighting Methods for Nonequilibrium Systems and Complex Flows." Prior to graduating with his M.S, Dustin worked as a NASA Langley Aerospace Reseach Summer Scholar intern.

In 2010, Dustin joined Lockheed Martin Missiles and Fire Control (LMMFC) in Grand Prairie, Texas as a modeling and simulation engineer. After a few years he transferred into the Aerodynamics Technology Center (AeroTC) as an aeronautical engineer. During this time he performed CFD, planned and performed wind tunnel tests, and served as aerodynamics lead on several missile programs. He has worked on projects including cruise missiles, gun launched projectiles, hypersonics, air-launched missiles and tactical surface-to-surface missiles. In 2017, while working at LMMFC, he began work on this doctoral degree from The University of Texas at Arlington. Still employed at LMMFC, he holds the title of aeronautical engineer staff.

His current research interests are shock wave/boundary layer interaction, numerical methods to combine disparate data fidelity levels, hypersonic design and propulsion. He is a senior member of AIAA, a former chair of the AIAA Missile

Systems Technical Committee, and currently a deputy directory of the AIAA Space and Missiles Group (SMG) within the AIAA Technology Activities Division (TAD).

He is married to Nicci Otten with three children, Stuart, Maxwell, and Genevieve.